How molecular doping affects the charge separation process in polymer-fullerene blends

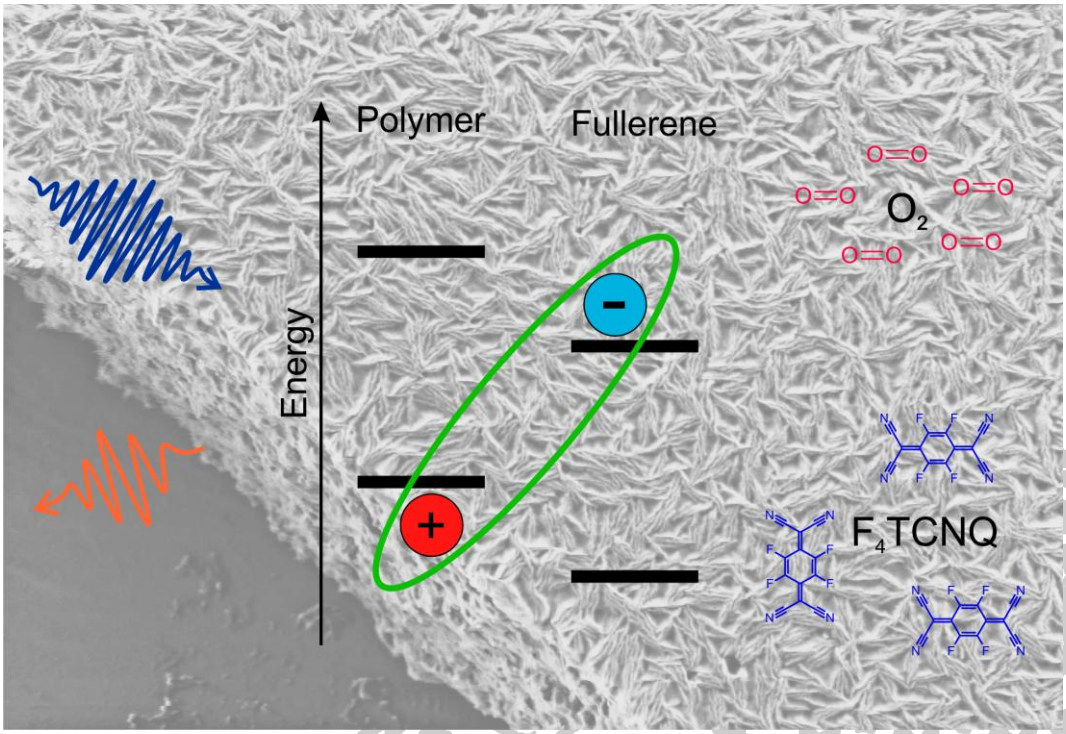

München 2012

How molecular doping affects the charge separation process in polymer-fullerene blends

Dissertation

submitted to the Physics Department

of the Ludwig-Maximilians-Universität München

by

Felix Alexander Deschler

of

Bayreuth, Germany

München, 14th December 2012

Cover picture:

SEM image of a dropcasted PCPDTBT film. The sketch displays a schematic representation of a charge transfer exciton in a polymer-fullerene blend. The dopant molecules F_4TCNQ and oxygen are shown.

First reviewer:	Prof. Dr. Jochen Feldmann
Second reviewer:	Prof. Dr. Müller-Buschbaum
Additional members of the examination:	Prof. Dr. Lode Pollet
	PD Dr. Stefan Ludwig
Date of the oral examination:	01.02.2013

Learn from yesterday, live for today, hope for tomorrow.

The important thing is to not stop questioning.

Albert Einstein

Publications presented in this thesis

Deschler F., Da Como E., Limmer T., Tautz R., Godde T., Bayer M., von Hauff E., Yilmaz S., Allard S., Scherf U., Feldmann J.
Reduced Charge Transfer Exciton Recombination in Organic Semiconductor Heterojunctions by Molecular Doping
Physical Review Letters 107, 127402. (2011)

Deschler F., De Sio A., von Hauff E., Kutka P., Sauermann T., Egelhaaf H.-J., Hauch J., Da Como E.
The Effect of Ageing on Exciton Dynamics, Charge Separation, and Recombination in P3HT/PCBM Photovoltaic Blends.
Advanced Functional Materials 22, 1461–1469. (2012)

Deschler F., Riedel D., Deák A., Da Como E.
Imaging morphology changes and phase segregation in doped polymeric semiconductors with low-voltage SEM
submitted (2012)

Further publications

Deschler F., Riedel D., Ecker B., Da Como E., von Hauff E., MacKenzie R.
Increasing organic solar cell efficiency with polymer interlayers
Phys. Chem. Chem. Phys., DOI: 10.1039/c2cp43876c, (2012)

Tunc A.V., De Sio A., Riedel D., Deschler F., Da Como E., Parisi J., von Hauff E.
Molecular doping of low-bandgap-polymer:fullerene solar cells: Effects on transport and solar cells.
Organic Electronics 13, 290–296. (2012)

De Sio A., Madena T., Huber R., Parisi J., Neyshtadt S., Deschler F., Da Como E., Esposito S., von Hauff E.
Solvent additives for tuning the photovoltaic properties of polymer–fullerene solar cells.
Solar Energy Materials and Solar Cells 95, 3536–3542. (2011)

Hallermann M., Deschler F., Berger J, von Hauff E., Da Como E.
Dynamics of Charge Transfer Excitons Recombination in Polymer/Fullerene Solar Cells
Material Research Society Proceedings 1286 (2011)

Contributions to conferences and workshops

Oral presentations

Deschler F., Da Como E, Feldmann J.
Enhanced exciton dissociation in doped organic semiconductors,
Light Harvesting Processes 2011, Kloster Banz, Germany

Deschler F., Da Como E, Feldmann J.
Enhanced charge separation in polymer/fullerene heterojunctions by molecular doping
SPIE Photonics West 2011, San Diego, CA, US

Deschler F., Riedel D., Da Como E, Feldmann J.
Doping as a new approach for charge generation in polymer-fullerene solarcells
Material Research Society Spring Meeting 2012, San Francisco, CA, US

Poster presentations

Deschler F., Tautz R., Hallermann M., von Hauff E., Da Como E., and Feldmann J.
Charge transfer excitons in conjugated polymer/fullerene blends
DFG Schwerpunktprogramm 1355 Winter School 2010, Bad Schandau, Germany

Deschler F., Da Como E., De Sio A., von Hauff E., Egelhaaf H.-J.
Identification and quantification of loss processes in aged P3HT/PCBM blends
Material Research Society Spring Meeting 2012, San Francisco, CA, US

Deschler F., Da Como E., De Sio A., von Hauff E., Egelhaaf H.-J.

The Effect of Ageing on Exciton Dynamics, Charge Separation, and Recombination in P3HT/PCBM Photovoltaic Blends

Gordon Research Conference Electronic Processes in Organic Materials 2012, Lucca, Italy

Kurzfassung

Diese Arbeit untersucht den Effekt niedermolekularen Dopings auf den Ladungstrennungsprozess in organischen Halbleiter-Heteroübergängen. Zur Klärung der grundlegenden Mechanismen werden verschiedene Dopanten und ihr förderlicher sowie nachteiliger Einfluss untersucht. Die gefundenen Erkenntnisse bieten aussichtsreiche Ansätze zur Verbesserung der Leistung organischer Solarzellen.
Der erste Teil dieser Arbeit zeigt Niederspannungs-Rasterelektronenmikroskopie (REM) als neue Methode zur hochauflösenden Detektion von p-Typ Dopanten-Verteilungen in konjugierten Polymer-Filmen. Diese Studie hat das Ziel den Effekt von Doping auf die Morphologie von organischen Halbleitern zu untersuchen. Dopantreiche Regionen werden in REM Bildern als helle Bereiche detektiert. Photolumineszenz(PL)-Kartierung bestätigt die Zuordnung dopantreicher Regionen, da ein Vergleich der dopantinduzierten PL-Quenching-Strukturen mit den, in REM beobachteten, Dopantverteilungen Domänen mit vergleichbarer Form und Größe zeigt. Selektives Aufladen dopantreicher Bereiche durch den Elektronstrahl wird als grundlegender Mechanismus des erhöhten REM Kontrasts identifiziert. Das neue Detektionsprinzip wird verwendet, um den Effekt von Doping auf die Morphologie zweier, für Solarzellen verwendeter, Polymere zu untersuchen (PCPDTBT, P3HT). PCPDTBT weist, verglichen mit P3HT, eine homogenere Filmmophologie und höhere Grenzwerte für Dopantclustering auf. Dies wird auf die Donor-Akzeptor Struktur von PCPDTBT zurückgeführt, die elektrostatische Dopant-Polymer Interaktionen abschirmt.
Der zweite Teil untersucht den Effekt molekularen Dopings auf die Rekombination von Charge transfer (CT) Exzitonen an der Grenzfläche von Polymer-Fulleren (PCPDTBT:PCBM) Blends. Elektrontransfer von Polymer-HOMO zu Dopant-LUMO (F_4CTNQ) führt zu p-Dotierung des Polymers im Grundzustand. Niedrige Dopingkonzentrationen (<4% Gewicht) reduzieren die CT Exziton Rekombination an der Grenzfläche and resultieren in einer bevorzugten Ladunsgträgerbildung. Dies wird durch das ultra-schnelle Quenching der CT Exziton Emission in zeitaufgelöster PL und die Zunahme der Polarondichte in zeitaufgelöster photoinduzierten Absorption (PIA) beobachtet. Ein Fit der zeitaufgelösten PL und PIA mit einem Ratengleichungsmodel signalisiert ferner eine, im Vergleich zur Polaronbildung, reduzierte CT Exziton Bildungsrate, was zur beobachteten höheren Polarondichte führt. Die Resultate werden durch dopinginduziertes Phasenraumfüllen und Blocken der niederenergetischen, unbeweglichen Randzustände des Polymer-HOMOs erklärt. Solarzellen aus dotierten Blends erzeugen, in Übereinstimmung mit den spektroskopischen Studien, einen erhöhten Photostrom. Diese Erkenntnisse tragen zum grundlegenden Verständnis des Ladungstrennungsprozesses und der Rolle von CT Exzitonen als Zwischenstufe bei. Zudem wird Elektronakzeptordoping als vielversprechende neue Methode zur Verbesserung der Solarzellenleistung vorgestellt.
Das letzte Kapitel erforscht den nachteiligen Effekt von Sauerstoffdoping auf die Ladungstrennung in P3HT:PCBM Blends mit spektroskopischen Methoden. Sauerstoffdoping unter Beleuchtung bewirkt Photooxidation und p-Dotierung des Polymers, auch Degradation genannt. Die Auswirkung auf die Exzitonpopulation wird durch Blend-Emissionsspektren für verschiedene Degradationsstufen untersucht. Die Ergebnisse weisen auf eine, mit Degradation, linear zunehmende Dichte von Quenchingstellen hin. Zur Untersuchung des Effekts von Sauerstoffdoping auf die Dynamik der Ladungsträgerbildung werden Exziton- und Polaronpopulation mit zeitaufgelöster PIA untersucht. Beide Populationen zeigen in degradierten Proben ein ultra-schnelles anfängliches Quenching und, auf längeren Zeitskalen, eine schnellere Rekombination. Der Effekt ist jedoch stärker für Polaronen ausgeprägt. Dies weist auf einen größeren Einfluss von Sauerstoffdoping an der Grenzfläche zwischen Polymer und Fulleren hin, an der Ladungstrennung erfolgt. Ein Ratengleichungsmodel wird verwendet um die zeitaufgelöste PIA zu fitten. Ultra-schnelles Einfangen von Exzitonen und Polaronen an Degradationsstellen wird als zentraler Verlustmechanismus identifiziert. Diese Ergebnisse tragen zum grundlegenden Verständnis der Degradation von organischen Solarzellen bei und helfen neue Wege zu finden die Lebenszeit von Photovoltaikmodulen zu verlängern.

Abstract

This thesis investigates the effect of small molecule doping on the charge separation process in organic semiconductor heterojunctions. To understand the underlying mechanisms, different dopants and their beneficial and adverse impact on charge separation were investigated. The insights from these results offer promising directions to improve organic solar cell performance.
In the first part, low-voltage scanning electron microscopy (SEM) is presented as a new approach to map p-type dopant distributions in conjugated polymer films with high resolution. This study is conducted to understand the effect of doping on the morphological properties of the organic semiconductors. Dopant-rich regions are detected as bright areas in SEM images. The assignment of dopant-rich regions is confirmed by photoluminescence (PL) mapping. Comparison of dopant induced PL quenching patterns with the distributions observed in SEM reveals domains with similar shape and size in both experiments. Additionally, site-selective charging by the electron beam is identified as the underlying mechanism for the increased SEM contrast. This novel mapping approach is employed to investigate the effect of doping on the morphology of two polymers (PCPDTBT, P3HT), which are widely used in organic solar cells. A more homogenous film morphology and a higher dopant clustering threshold is observed for PCPDTBT, compared to P3HT. These findings are attributed to the special donor-acceptor structure of PCPDTBT, screening the dopant-polymer electrostatic interaction.
The second part investigates the effect of molecular doping on the recombination of charge transfer (CT) excitons localized at polymer–fullerene (PCPDTBT:PCBM) interfaces. Electron transfer from the polymer HOMO (highest occupied molecular orbital) to the dopant (F_4TCNQ) LUMO (lowest unoccupied molecular orbital) leads to ground-state p-doping. A low dopant concentration (<4% weight) reduces the interfacial recombination via CT excitons and results in a favoured formation of separated carriers. This is observed by ultrafast quenching of CT exciton emission in transient PL and an increase in polaron density in transient photoinduced absorption (PIA). Furthermore, a rate equation model, used to fit the transient PL and PIA, reveals a reduced rate of CT exciton compared to polaron formation, giving rise to the observed increase in polaron yield. The results are interpreted on the basis of doping induced phase-space filling and blocking of low-energy, immobile tail states in the polymer HOMO. Prototype solar cells, fabricated from the doped blends, show an increase in photocurrent, in accordance with the spectroscopic studies. These findings are important for the fundamental understanding of the charge separation process and the role of CT excitons as intermediate steps. Further, electron acceptor doping is presented as a promising method to improve organic solar cell performance.
The last chapter studies the adverse effect of oxygen doping on charge generation in P3HT:PCBM blends with spectroscopic methods. Oxygen doping under illumination is known to cause photo-oxidation and p-type doping of the polymer, termed degradation. The effects on the exciton population are investigated from blend PL spectra for different degradation extents. The results indicate a linearly increasing density of quenching sites with increasing degradation. To address the effect of oxygen doping on the dynamics of charge formation, transient PIA is employed to study exciton and polaron populations. With increasing degradation, both populations exhibit an ultrafast initial quenching and a faster decay on longer time scales. However, the effect is more severe for polarons. This indicates a more pronounced influence of oxygen doping at the interface between polymer and fullerene, where charge separation occurs. A rate equation model is used to fit the transient PIA. From this, ultra-fast trapping of excitons and polarons at degradation sites is identified as the main loss mechanism. These results contribute to the fundamental understanding of degradation processes in organic solar cells and will help to find new ways to extend the lifetimes of organic photovoltaic modules.

Table of contents

List of abbreviations

AFM	Atomic force microscopy
CCD	Charge coupled device
CT exciton	Charge transfer exciton
DOS	Density of states
DP	Delocalized polaron
F4-TCNQ	2,3,5,6-Tetrafluoro-7,7,8,8-tetracyanoquinodimethane
FF	Fillfactor
GSB	Ground state bleach
HOMO	Highest occupied molecular orbital
I_{SC}	Short circuit current
LP	Locliazed polaron
LUMO	Lowest unoccupied molecular orbital
MIR	Mid-infrared
NIR	Near-infrared
NOPA	Non-linear optical parametric amplifier
OLED	Organic light emitting diode
OPA	Optical parametric amplifier
P3HT	Poly(3-hexylthiophen-2,5-diyl)
PCBM	Phenyl-C61-butyric acid methyl ester
PCPDTBT	Poly[2,1,3-benzothiadiazole-4,7-diyl[4,4-bis(2-ethylhexyl)-4H-cyclopenta[2,1-b:3,4-b']dithiophene-2,6-diyl]]
PIA	Photo-induced absorption
PL	Photoluminescence
RPM	Rounds per minute

SE	Stimulated emission
SEM	Scanning electron microscope
SHG	Second harmonic generation
TA	Transient absorption
TCNQ	Tetracyanoquinodimethane
TEM	Transmission electron microscope
TrA	Triplet exciton absorption ($T_1 \rightarrow T_n$)
UV	Ultraviolet
V_{OC}	Open circuit voltage
WL	White light
YAG	Yttrium aluminium garnet

1 The road to clean energy production from renewable sources

On June 21, 1979 the 39th President of the United States, Jimmy Carter, had 32 solar panels installed on the roof of the White House. On the same day he gave a speech in which he stated:

> *"A generation from now, this solar heater can either be a curiosity, a museum piece, an example of a road not taken or it can be just a small part of one of the greatest and most exciting adventures ever undertaken by the American people."*

More than 30 years later, one has to conclude, that the road to regenerative energies, mentioned by President Carter, has only been travelled partially. We are still underway on this "*exciting adventure*" to clean energy production. The increasing need for clean energy due to a rising world population and global warming remains an unsolved problem. In 2011, only 4% of the global power consumption was provided from regenerative energy sources like wind, water and solar energy [1]. Advances in these technologies are necessary to find energetically and economically sensible means for power generation.

Current photovoltaic applications are mainly based on inorganic semiconductors such as silicon. These have found widespread use as active material in transistors and computer technology, and resulted in the rise of global computer technology companies. However, the manufacture of efficient photovoltaic panels from silicon is quite expensive and a substantial amount of energy has to be used during fabrication to melt the inorganic semiconductors. This raises the question of alternative materials for photovoltaic applications with more favourable properties. During the 20th century a new class of materials has been invented, which have found great interest in academia and industry: organic semiconductors [2–4]. These materials are closely related to common plastics, like e.g. polystyrene, and consist mainly of carbon atoms. It is possible to design these materials by means of organic chemistry, which allows synthesising a variety of different compounds. Additionally like other plastics, they can be fabricated

in almost every shape, are flexible and light- weight, and offer room temperature processability with simple technologies, as for example ink-jet printing. So far these materials have found everyday application in organic light emitting diodes (OLEDs) for displays and lighting [5,6]. Several companies already sell consumer products with OLEDs for the mass market, like smartphones and tablet computers. These products show the competitive advantage of organic semiconductors in applications, where weight reduction and compactness are key factors.

In the last years, organic semiconductors have also found increasing use in photovoltaic applications. Starting from a low overall efficiency of around 2% in 2000, recently a value of 10% has been reached [7,8] (Figure 1.1).

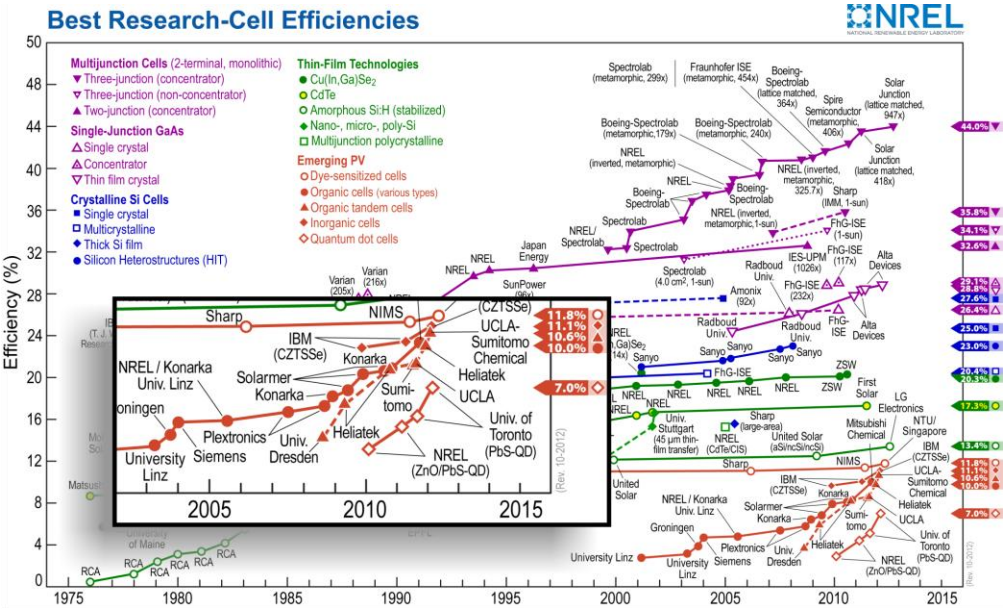

Figure 1.1 Improvement of maximum power conversion efficiencies for different photovoltaic technologies measured under laboratory conditions from 1970 to 2012. The inset shows a zoom on the development of organic solar cells (full circles) in the last years. Image adapted from www.nrel.gov.

Despite these advances, silicon solar panels still show a significantly higher power conversion efficiency of above 20% [9]. Further advances are therefore necessary to bring the promising organic photovoltaic technology into the market. Two critical missing requirements for mass market application of organic photovoltaics are higher efficiencies and long-term stability. Without improvements in power conversion efficiency and lifetimes of panels of about 10 years, the market will not accept this new

technology. It is the task of research to address these challenges. For power generation the energy cost versus the energy produced is a critical parameter. For an optimal device this ratio should be as small as possible. Especially in this respect, organic photovoltaics present a promising technology, since their fabrication involves no energy-intensive step, i.e. the melting and purification of silicon for standard solar cells. Just like last century has been the century of silicon based technology, maybe the current century will be the century of organic semiconductors, due to their fascinating properties and promising applications at low cost.

One main step in solar cell operation is the conversion of absorbed photons into charge carriers. In organic semiconductors this process involves the photo-excitation of strongly bound excitons, which have to be separated into free charge carriers. The present thesis studies the effects of *small molecule* doping on this charge separation process in organic semiconductors. On the one hand, changes in the electronic structure of a low-bandgap polymer:fullerene blend, induced by doping with electron acceptors, are shown to reduce recombination via CT excitons and enhance charge separation. On the other hand, degradation effects on exciton and polaron populations in polymer-fullerene blends, induced from oxygen doping, are discussed. As one of the earliest examples of doping in organic semiconductors, the conductivity of polyacetylene was increased by exposure to iodine vapour [4] in 1977. In recent years, the topic of controlled doping of polymer films with small electron acceptor molecules has been addressed with focus on changes in the transport properties of the organic semiconductor [10,11]. In parallel, other groups used dopant molecules to study the fundamental mechanisms of charge transfer in highly ordered systems. For example, pentacene monolayers including single dopant molecules were investigated with photoemission spectroscopy and scanning tunnelling microscopy [12,13]. In summary, studies on the effect of doping in organic semiconductors have been limited to transport phenomena or basic electronic properties. It remains still an open question how doping affects other properties of organic semiconductors besides transport. Therefore, this thesis investigates the effects of small molecule doping on the charge separation process at the heterojunction of conjugated polymer-fullerene blends.

The thesis is structured in the following way: In Chapter 2 we give an overview on the fundamental theories relevant for photo-induced charge generation in organic semiconductors. First, the general properties of organic semiconductors and their

differences compared to inorganic semiconductors are discussed. Subsequently, the energy structure and the quantum mechanical description of the molecules' energy levels are presented. Additionally, the principal neutral and charged excitations are described together with the optical transitions used to study these materials spectroscopically. The possibility to transport energy in the material and the corresponding theories are presented. Furthermore, the basic theory of photocarrier generation is described based on the Onsager-Braun formalism. In the last section charge transport and basic properties of solar cell operation are briefly outlined.

Chapter 3 gives an overview of the materials and methods employed. The basic chemical and physical properties of the conjugated polymers PCPDTBT (*Poly[2,1,3-benzothiadiazole-4,7-diyl[4,4-bis(2-ethylhexyl)-4H-cyclopenta[2,1-b:3,4-']dithiophene-2,6-diyl]]*) and P3HT (*Poly(3-hexylthiophen-2,5-diyl)*) are described together with the electron acceptor molecule $PC_{60}BM$, which is a fullerene derivative. Additionally, the small molecule dopant F_4TCNQ (*2,3,5,6-Tetrafluoro-7,7,8,8-tetracyanoquino-dimethane*) is introduced, which is a strong electron p-type dopant molecule. Further, the fabrication of thin film samples from liquid solutions of the materials is described. In the last section, the employed experimental techniques are outlined. The basic principle of steady state and time resolved spectroscopic techniques are explained and the microscopy setups, used to study the film morphology, are presented.

Chapter 4 deals with the influence of small molecule doping on the thin film morphology of conjugated polymers. The effect of F_4TCNQ incorporation on PCPDTBT and P3HT films is studied with atomic force microscopy (AFM), scanning electron microscopy (SEM) and confocal laser scanning photoluminescence (PL) mapping. It is shown that the distribution of dopant molecules can be assessed from an increased contrast between doped and undoped regions in low-voltage SEM images. In the last part of this chapter, the physical origin of the increased contrast in SEM images of doped films is discussed.

Chapter 5 discusses the effect of dopant induced changes in the electronic structure of PCPDTBT:PCBM blends on the charge generation process. In particular, the impact of doping on the recombination of charge transfer (CT) excitons is studied. Steady-state and time-resolved PL spectroscopy are employed to study the CT exciton emission in doped films. Concomitantly, the polaron yield is investigated from transient absorption measurements. Furthermore, a rate equation model is employed to model the transient

photoluminescence and transient absorption data. Finally, solar cells with doped PCPDTBT:PCBM blends are presented, to compare the spectroscopic experiments with solar cell performance.

Chapter 6 discusses the effects of oxygen doping on the photogeneration of charges in P3HT:PCBM blends. Usually, oxygen doping has a detrimental effect on organic solar cells, which is termed degradation. First, steady state absorption and photoluminescence spectroscopy are used to quantify the effect of oxygen doping on excitons. Additionally, the effect of degradation on the charge generation is investigated from transient absorption experiments on excitons and polarons for different degradation levels. The most relevant degradation mechanisms are identified from a rate equation model fitting the transient absorption data. The spectroscopic results are compared with the photovoltaic performance of degraded solar cells.

Chapter 7 summarizes the findings and gives an outlook on possible future experiments and applications.

2 Fundamental concepts of photo-induced charge generation in organic semiconductors

This chapter gives an overview on the theoretical background of the photo-induced charge generation process in organic semiconductors: after absorption of photons in a donor-acceptor blend, excitons are generated. These diffuse to the donor-acceptor interface (heterojunction) by energy transfer in pure domains of the materials. Exciton dissociation and charge generation primarily occurs at the heterojunction. In a solar cell the generated charges are transported to the electrodes and extracted.

We start with a description of the general properties of organic semiconductors and their basic properties. Theoretical methods to calculate the energy levels of organic semiconductor molecules are explained and the respective neutral and charged molecular excitations are presented. The optical excitation and the transport of energy through the material are detailed. The photogeneration of charge carriers and the relevant Onsager-Braun theory are discussed. The role of charge transfer excitons in charge dissociation is outlined. In the last part, a short explanation of photovoltaic operation and the critical solar cell parameters is given.

2.1 Molecules with delocalized π-electron systems

Organic semiconductors can be obtained in a variety of different molecular sizes. The scale ranges from small molecules with less than ten atoms to large polymeric macromolecules with more than hundred repeat units. Most of the research concerns polymeric macromolecules with a delocalized electron system, which gives rise to semi-conducting properties. Interestingly, these materials also exist in nature, with Melanin being one important example. In 1963, Bolto and McNeill demonstrated that doping of Melanin with iodine substantially increases its conductivity [2,3,14]. Thin films of synthetic Melanin were fabricated in 1974 [15] and in 1977 Shirakawa *et al.* achieved a large change in conductivity by iodine doping of these synthetic polymers [16]. For these discoveries, Shirakawa, Heeger and MacDiarmid were awarded the Nobel Prize in Chemistry in 2000 [17]. Besides the fundamental research on the electronic properties, in recent years this class of materials also found applications in light-emitting diodes [18–20], photovoltaics [21–25], field-effect transistors [26–29] and optically pumped lasers [30,31]. The following paragraphs give an overview of the fundamental theories of organic semiconductors, referring to the seminal literature [32–35].

The main building blocks of organic semiconductors are carbon atoms. Due to a delocalization of valence π-electrons, the molecules show semiconducting properties. The reason for the delocalization lies in the special type of bonding between two carbon atoms, described in the following. The ground state electron configuration of a carbon atom is $1s^2 2s^2 2p_x^1 2p_y^1$. Hybridization of the orbitals occurs by forming three degenerate sp^2 orbitals from one *s* and two *p* orbitals, as shown in Figure 2.1.

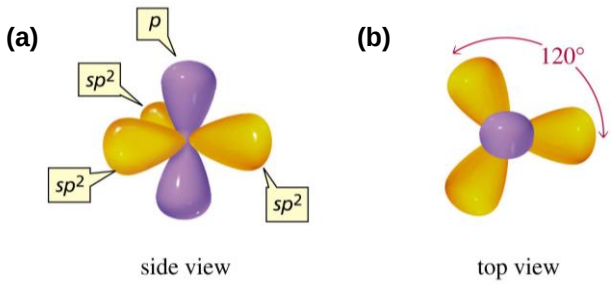

Figure 2.1 Schematic representation of the orbitals in an sp^2 hybridized carbon atom seen from the side (a) and top (b). Yellow represents the hybrid orbitals while purple shows the residual p_z-orbital perpendicular to the plane of sp^2 orbitals. Image adapted from [36].

The sp^2 orbitals are coplanar and arranged at an angle of 120° to each other. The residual $2p_z$ orbital is perpendicular to the plane of hybrid orbitals. As an example how hybridization leads to the formation of delocalized orbitals, the schematic orbital geometry for ethene is shown in Figure 2.2. The bond between the carbon atoms is created by the overlap of sp^2 orbitals, forming σ-bonds, which are the strongest type of covalent chemical bonds.

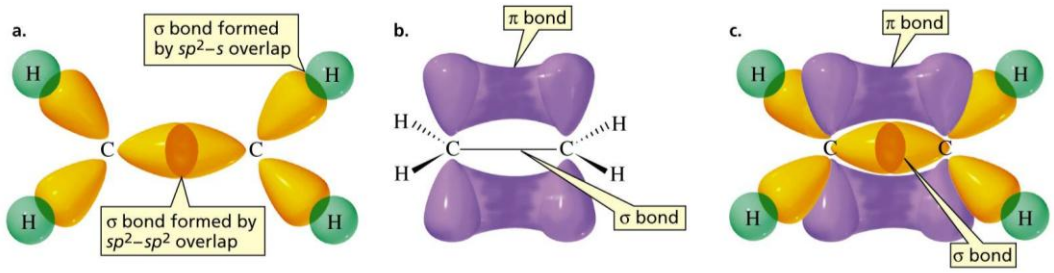

Figure 2.2 Schematic representation of the orbital structure in ethene (c). Yellow represents the hybrid orbitals while purple shows the residual $2p_z$-orbitals perpendicular to the plane of sp^2 orbitals. σ-bonds are shown in (a), while π-bonds are depicted in (b). Image adapted from [36].

The remaining $2p_z$ orbitals form a so called π-bond. Figure 2.2c depicts how the electron density in the π-bond cannot be assigned to one carbon atom, but is spread along the whole molecule above and below the central axis connecting the carbon atoms. This delocalization of the electron density is called π-conjugation and is a characteristic of organic semiconductors. Due to the lower overlap of the $2p_z$ orbitals, the π-bonds are much weaker and more polarizable than σ-bonds.

The overlap of two σ-(π-)orbitals from individual carbon atoms creates one bonding σ-(π-)orbital and one anti-bonding σ*-(π*-)orbital (Figure 2.3). In the ground state only the bonding orbitals are populated with two electrons each, since the anti-bonding orbitals are higher in energy. The lowest electronic transitions occur therefore between the highest bonding and the lowest anti-bonding orbital, which are most commonly π- and π*-orbitals. In general, the highest occupied molecular energy level is called highest occupied molecular orbital (HOMO), while the next higher energetic level is called lowest unoccupied molecular orbital (LUMO).

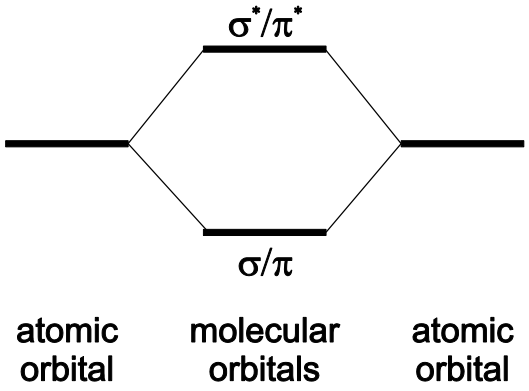

Figure 2.3 Sketch of the energy levels for atomic and molecular orbitals. The overlap of two atomic σ-/π-orbitals generates binding (σ/π) and anti-binding (σ*/π*) molecular orbitals, which are shifted in energy.

The concept of electron density delocalization is not limited to small molecules, but also observed, and especially relevant, for larger molecules, i.e. benzene or anthracene, where conjugated alternating bonds are found. Another important class of organic semiconductors are conjugated polymers which show a delocalization of the electron density along the backbone of the polymer chain. These materials have a substantial higher molecular weight compared to small molecule organic semiconductors. One model compound for conjugated polymers is polyacetylene. A significant feature of conjugated polymers is the alteration of single and double carbon bonds along the chain (Figure 2.4), which leads to the delocalisation of the electron density along the chain.

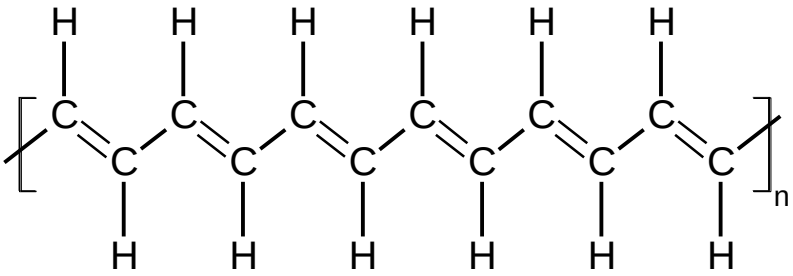

Figure 2.4 Chemical structure of the conjugated polymer polyacetylene with alternating single and double bonds between carbon atoms, giving rise to delocalized electron densities.

For a perfect infinite chain of alternating single and double bonds the overlap of orbitals results in a semi-filled band of energies, which leads to metallic behaviour. However, semiconducting properties are observed in conjugated polymers. Peierls showed that in

a one-dimensional system with incompletely filled bands, instabilities cause a lattice distortion which induces differences in bond lengths between single and double bonds [37]. Accordingly the length of the elementary cell of the one-dimensional chain is doubled, leading to an energy gap E_g between the bands of bonding and antibonding orbital configurations of a conjugated polymer chain. For this reason conjugated polymers behave like semiconductors rather than metals. The value of the energy gap depends on the length over which the electron density is delocalized. However, for conjugated polymers with a high molecular weight, the ideal case of delocalization over the whole chain is not observed. After a certain number of repeat units the conjugation is broken, e.g. by kinks in the planar configuration of the chain or by chemical defects, resulting in a reduced conjugation length. Control of the conjugation length by varying the size or conformation of the polymer allows tuning the energy gap in the range of 1.5 eV to 3 eV [33].

2.2 Energy levels of organic semiconducting molecules

In order to understand the properties of organic semiconductors, knowledge about the energy levels is critical. The starting point for these calculations is the time-independent Schrödinger equation together with a suitable molecular Hamiltonian and an ansatz for the wavefunction according to molecular orbital theory [38]. Due to the complexity of this many-body system, involving the coordinates of all electrons and nuclei, simplifications and approximations for the Hamiltonian and the wavefunction have to be employed to obtain a solution.

2.2.1 General Hamiltonian for molecular systems

Let's consider the case of a molecule with N_{nuc} atoms with atomic numbers $z_1, \dots, z_{N_{nuc}}$ and N_{el} electrons with Cartesian coordinates $\boldsymbol{r}_j$ for the j^{th} electron. The momentum of the j^{th} electron is denoted with $\boldsymbol{p}_j$. The Cartesian coordinates and momenta for the nuclei are $\boldsymbol{R}_n$ and $\boldsymbol{P}_n$ respectively. The general Hamiltonian operator for the system is then of the form

$$H_{mol} = T_{el} + T_{nuc} + V_{el-el} + V_{nuc-nuc} + V_{el-nuc}\,. \qquad \textbf{(2-1)}$$

Here the kinetic energy of electrons T_{el} and nuclei T_{nuc} is given by

$$T_{el} = \sum_{j=1}^{N_{el}} \frac{\boldsymbol{p}_j^2}{2m_{el}} \tag{2-2}$$

and

$$T_{nuc} = \sum_{n=1}^{N_{nuc}} \frac{\boldsymbol{P}_n^2}{2M_n} \tag{2-3}$$

respectively, with the electron mass m_{el} and the mass of the n^{th} nucleus M_n. Due to the negative charge of electrons and the positive charge of nuclei, attractive and repulsive Coulomb forces have to be taken into account. The repulsive Coulomb pair interaction between electrons is described by

$$V_{el-el} = \frac{1}{2} \sum_{i \neq j} \frac{e^2}{|\boldsymbol{r}_j - \boldsymbol{r}_i|} \tag{2-4}$$

and for nuclei by

$$V_{nuc-nuc} = \frac{1}{2} \sum_{m \neq n} \frac{z_m z_n e^2}{|\boldsymbol{R}_m - \boldsymbol{R}_n|}. \tag{2-5}$$

Finally, for the attractive interaction of electrons and nuclei we have

$$V_{el-nuc} = \frac{1}{2} \sum_{j,n} \frac{z_n e^2}{|\boldsymbol{R}_n - \boldsymbol{r}_j|}. \tag{2-6}$$

All information about the quantum system is now contained in the time-independent Schrödinger equation

$$H_{mol} \cdot \Psi(r, R, \sigma) = \mathcal{E} \cdot \Psi(r, R, \sigma) \tag{2-7}$$

with the wavefunction $\Psi(r, R, \sigma)$ and the eigenenergies $\mathcal{E}$. The quantum number σ had to be introduced to account for the electron spin, since the non-relativistic Hamiltonian **(**2-1**)** does not allow for a rigorous introduction of spin operators. The formulation of the Cartesian coordinates was simplified as $r = (\boldsymbol{r}_1 \boldsymbol{r}_2, \ldots \boldsymbol{r}_{N_{el}})$ and $R = (\boldsymbol{R}_1 \boldsymbol{R}_2, \ldots \boldsymbol{R}_{N_{nuc}})$. Without knowing the explicit formulation of the wavefunction $\Psi(r, R, \sigma)$, we can already make several statements about its general features:

(1) From the spin-independent formulation of the molecular Hamiltonian **(**2-1**)** we conclude that the wavefunction can be separated in two parts according to

$$\psi(r, R, \sigma) = \phi(r, R) \cdot \zeta(\sigma) \quad \textbf{(}2\text{-}8\textbf{)}$$

with $\zeta(\sigma)$ being the spin function for the electrons. The values of the spin states σ_j are either parallel (spin up) or antiparallel (spin down) to a certain spatial direction.

(2) According to the Pauli principle the wavefunction of a system of electrons, which are fermions, has to be antisymmetric under exchange of any two electronic indices. This means that $\Psi(r, R, \sigma)$ has to be antisymmetric in Cartesian and spin coordinates. The fact that the Pauli principle applies also to identical nuclei is often neglected, since the wavefunctions of nuclei are more localized.

(3) The solutions of Equation **(**2-7**)** will give a series of eigenenergies $\mathcal{E}_\lambda$ with corresponding eigenfunctions $\Psi_\lambda(r, R, \sigma)$. The lowest eigenenergy $\mathcal{E}_0$ will define the ground state of the system. These values are the molecular energy levels.

2.2.2 Simplifications of the full molecular Hamiltonian

The *Born-Oppenheimer approximation* is the most critical simplification of the molecular Hamiltonian and is based on the difference in electron and nuclear masses ($m_{el}/M_{nuc} < 10^{-3}$). This relation implies that electrons move much faster than the nuclei and respond to changes in the nuclear configuration almost immediately. The Born-Oppenheimer approach therefore assumes a constant nuclear distribution in which the electrons move. With this, it is now possible to define a purely electronic Hamiltonian, which only depends parametrically on the coordinates R of the nuclei:

$$H_{el}(R) = T_{el} + V_{el-el} + V_{el-nuc}(R) + V_{nuc-nuc}(R). \quad \textbf{(}2\text{-}9\textbf{)}$$

The solutions $\phi(r, R)$ to the Schrödinger equation employing the electronic Hamiltonian

$$H_{el}(R)\, \phi_a(r, R) = [E_a(R) + V_{nuc-nuc}]\, \phi_a(r, R) \quad \textbf{(}2\text{-}10\textbf{)}$$

describe the motion of electrons in the static nuclear configuration. The nuclear-nuclear interaction $V_{nuc-nuc}$ does not play a role in the calculation of the electronic wavefunctions. It is simply a constant that arises on both sides of the equation and cancels out, leading to the following Schrödinger equation for the electronic wavefunctions:

$$[T_{el} + V_{el-el} + V_{el-nuc}]\, \phi_a(r, R) = E_a(R)\, \phi_a(r, R) \qquad \textbf{(}2\text{-}11\textbf{)}$$

The solutions to Equation **(**2-11**)** depend parametrically on the coordinates R. The index a describes the different energy levels E_a and the corresponding wavefunction ϕ_a. The full molecular wavefunction is now constructed using an expansion in the electronic wavefunctions ϕ_a:

$$\psi(r, R) = \sum_a \phi_a(r, R)\, \chi_a(R) \qquad \textbf{(}2\text{-}12\textbf{)}$$

The expansion coefficients $\chi_a(R)$ are interpreted as the nuclear wavefunctions and are found by solving the nuclear Schrödinger equation, neglecting non-adiabatic coupling of electronic states with nuclear motion. This is essentially the Born-Oppenheimer approximation:

$$[T_{nuc} + U_a(R)]\, \chi_a(R) = \mathcal{E}\, \chi_a(R) \qquad \textbf{(}2\text{-}13\textbf{)}$$

In this equation $U_a(R)$ represents an effective potential for the motion of the nuclei, describing their mutual Coulombic interaction and the interaction with the electronic charge distribution given by the electronic wavefunctions:

$$U_a(R) = E_a(R) + V_{nuc-nuc} \qquad \textbf{(}2\text{-}14\textbf{)}$$

With these approximations we still have the quite complicated Hamiltonian of Equation **(**2-9**)** to solve. However the complexity of the problem can be reduced by further simplifications. For this it is convenient to write the electronic molecular Hamiltonian in one- and two-particle terms:

$$H = \sum_{i,j} t_{ij} \left(|\psi_i\rangle\langle\psi_j| + |\psi_j\rangle\, \langle\psi_i| \right) + \sum_{ijkl} V_{ijkl}\, |\psi_i, \psi_k\rangle\langle\psi_j, \psi_l| + V_{nuc-nuc} \qquad \textbf{(}2\text{-}15\textbf{)}$$

with the electronic one-particle part

$$t_{ij} = \int \psi_i^*(r) \left[\frac{p^2}{2m} + V_p(r,R) \right] \psi_j(r) dr^3 \qquad \textbf{(}2\text{-}16\textbf{)}$$

and the electronic two-particle part

$$V_{ijkl} = \iint \psi_i^*(r) \psi_k^*(r') \, V_{el-el}^{eff}(r-r') \psi_j(r) \psi_l(r') dr^3 dr'^3 \, . \qquad \textbf{(}2\text{-}17\textbf{)}$$

In these equations $V_p(r,R)$ is the effective potential for electron-nucleus interactions, V_{el-el}^{eff} describes the effective electron-electron interactions and $V_{nuc-nuc}$ is the interaction between nuclei. The model with the most severe simplifications is *Hückel theory* [39–41] where electron-electron interactions (V_{iiii} , V_{iijj} and $V_p(r,R)$), exchange interactions (V_{ijji}) and nuclear interactions $V_{nuc-nuc}$ are neglected. Additionally the wavefunction is set as a linear combination of atomic orbitals (LCAO method). In a slightly more complex model, electron-phonon interactions ($V_p(r,R) \neq 0$) are introduced, assuming only one mode coupling to the π-electrons. This is the *Su-Schrieffer-Heeger model* [42]. Several other approximations exist, which differ in the considered contributions of the electronic molecular Hamiltonian.

2.2.3 Solution of the Schrödinger equation with the Hartree-Fock method

Since the exact solution of the full electronic Hamiltonian **(**2-9**)** is only possible with several approximations, methods to calculate solutions numerically have been derived. The work-horse for these calculations is Hartree-Fock theory. One starts again from the Schrödinger Equation **(**2-11**)**, but the electronic wavefunction of the molecule is created as a product of single-particle electron wavefunctions solving the equation

$$[T_{el}(i) + V_{el-nuc}(\boldsymbol{r}_i)]\varphi_\alpha(\boldsymbol{r}_i) = \varepsilon_\alpha \varphi_\alpha(\boldsymbol{r}_i) \, , \qquad \textbf{(}2\text{-}18\textbf{)}$$

i.e. the interactions between electrons are switched off. The index α describes the different energy levels ε_α and the corresponding wavefunctions φ_α.

Since we have to take the Pauli principle into account, the total wavefunction of the system is supposed to be antisymmetric, so a Slater determinant is used to generate an ansatz for the wavefunction of all N electrons:

$$\phi(1,..,N) \sim \begin{vmatrix} \varphi_1(1) & \cdots & \varphi_1(N) \\ \vdots & \ddots & \vdots \\ \varphi_N(1) & \cdots & \varphi_N(N) \end{vmatrix} \quad \textbf{(}2\text{-}19\textbf{)}$$

Employing the variational principle using the full Hamiltonian **(**2-9**)** and the wavefunction from **(**2-19**)**, one arrives at a set of coupled integro-differential equations[35], the Hartree-Fock equations:

$$F(\boldsymbol{r})\varphi_\alpha(\boldsymbol{r}) = \mathcal{E}_a\varphi_\alpha(\boldsymbol{r}) \quad \textbf{(}2\text{-}20\textbf{)}$$

with the Fock operator

$$F(\boldsymbol{r}) = [T_{el}(i) + V_{el-nuc}(\boldsymbol{r})] + \sum_{b}^{N/2} [2J_b(\boldsymbol{r}) - K_b(\boldsymbol{r})] \quad \textbf{(}2\text{-}21\textbf{)}$$

the Coulomb operator

$$J_a(\boldsymbol{r}) = \int |\varphi_\alpha(\boldsymbol{r}')|^2 \, V_{el-el}(\boldsymbol{r},\boldsymbol{r}') \; d\boldsymbol{r}'^3 \quad \textbf{(}2\text{-}22\textbf{)}$$

and the exchange operator

$$K_b(\boldsymbol{r})\varphi_\alpha(\boldsymbol{r}) = \left[\int \varphi_b^*(\boldsymbol{r}') \; V_{el-el}(\boldsymbol{r},\boldsymbol{r}') \; \varphi_\alpha(\boldsymbol{r}')\right]\varphi_b(\boldsymbol{r}) \quad \textbf{(}2\text{-}23\textbf{)}$$

For a detailed derivation of these formulations, the reader is referred to the standard literature [33,35]. In the Hartree-Fock equations the interaction of an individual electron with the remaining electrons is only taken into account as an effective potential created from the other electrons, as can be seen from Equation **(**2-22**)**. The computational calculation involves the iterative solution of the Fock equations, since the Fock operator itself contains the orbitals $\varphi_\alpha(\boldsymbol{r})$. Starting from some trial orbitals the Fock equations are solved and the new orbitals are used to calculate an updated Fock operator, which is again used to solve the Fock equations. This iteration is repeated until a self-consistent solution is reached. Therefore this computational approach is termed *Hartree-Fock self-consistent field method*.

2.3 Molecules in the solid state – the effects of disorder

In the previous parapgraphs the properties of organic semiconductors on the level of single molecules were described, taking only *intramolecular* forces into account. Going from individual molecules to the solid state, intermolecular forces have to be considered. In general, there are four types of intermolecular forces: Ionic bonds (long-range Coulomb interactions in ionic crystals), metallic interactions (delocalized electron gas), covalent bonding (sharing of electrons between molecules) and Van der Waals forces (induced electrical dipole forces between neutral molecules). Because of the absence of free electrons in organic semiconductors, mainly Van der Waals interactions play a role. These interactions are attractive forces between two neutral, nonpolar molecules due to temporally fluctuating charge distributions. The fluctuations induce dipoles in neighbouring molecules, which results in an attractive force. On the other hand, also repulsive forces exist, which are due to the Pauli principle. These forces concern the interaction of electrons in corresponding orbitals but from different molecules. The superposition of attractive and repulsive forces results in an overall potential, which is modelled with the Lennard-Jones potential:

$$V = \frac{C_{12}}{r^{12}} - \frac{A}{r^{6}} \qquad \textbf{(}2\text{-}24\textbf{)}$$

The terms A and C_{12} are independent of the molecules' distance r and contain information on the molecules' properties, e.g. the ionisation energy. Only interactions between neighbouring molecules will play a role, due to the strong dependence of the potential on the intermolecular distance. Therefore, any long range interaction in organic semiconductors is negligible. Crystal formation is limited to special cases or to molecules with additional ionic contributions to the intermolecular forces. In these systems a band-like energy structure is observed, given by a periodic potential in analogy to inorganic semiconductors. However, the bandwidth is only of the order of a few meV, due to the low intermolecular interactions compared to inorganics.

The typical conformation and structure of organic semiconductors in the solid state is therefore amorphous with substantial disorder. Furthermore, due to the weak intermolecular interaction, the properties of molecules in the solid state differ only slightly from isolated molecules and many properties can be already derived from the single isolated molecule properties as calculated from the models in Paragraph 2.2. However, the disorder present in the film has an impact on the energy levels of the

individual molecules. First, every molecule is positioned in a different dielectric environment, which affects the electronic states. A simple analogy is the energy shift of molecular absorption spectra for different solvents. Second, every molecule differs slightly in geometrical conformation, e.g. due to twists and kinks in the backbone for the case of polymers, leading to a distribution of conjugation lengths and accordingly, energy levels. The resulting shifts in molecular energies give rise to a Gaussian distribution [43–45] of states around a most probable energy value (Figure 2.5a). The large number of molecules in the film leads to a quasi-continuous distribution of energy levels within the Gaussian broadened density of states. For this reason one often refers to an "energy band", however it is important to note that the origin of this "band" is not due to a periodic potential, as for inorganic semiconductors, but to spatial disorder. The Gaussian distribution of energy levels exists for neutral excitons as well as for charged (polaron) states. The energy level distribution upon formation of an amorphous film is shown in Figure 2.5b for the HOMO and LUMO levels. The energy level broadening plays a critical role in the description of charge and energy transport phenomena as discussed below.

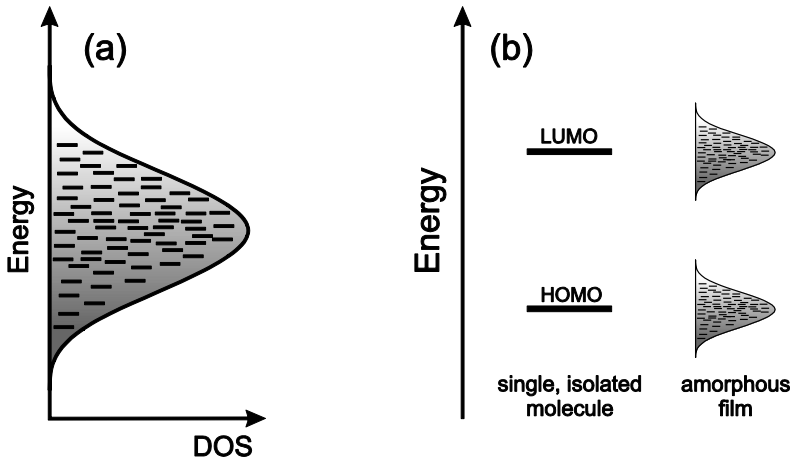

Figure 2.5 (a) Schematic representation of the disorder induced Gaussian broadening of the density of states for a molecular energy level in a disordered film. The maximum of the distribution relates to the energy level of an isolated molecule. (b) Broadening of HOMO and LUMO energy levels on the transition from the single isolated molecule to an amorphous film.

2.4 Neutral and charged excitations

2.4.1 Excitons

Optical excitation of an inorganic semiconductor generally leads to free charges, because the high dielectric constant of the material screens the interaction of positive and negative charges. In organic semiconductors the dielectric constant is low ($\varepsilon \sim 3$-4) and electron-electron interactions are dominant. Therefore, once an electron is excited, it forms in combination with the hole a bound state. This neutral excitation of the system is termed exciton. The binding energy E_b of the exciton is defined by the Coulomb attraction and is basically determined by the energy difference between the bound electron-hole pair and the configuration corresponding to free charges. In inorganic semiconductors the thermal energy kT is sufficient to separate the electron-hole pair, while in organic semiconductors the exciton binding energy can be as high as 0.5 eV up to 1 eV [46–49]. Based on the spatial extension of the exciton, which depends on the binding energy E_b, one differentiates different types of excitons (Figure 2.6). There is the strongly delocalized Wannier-type exciton, which is usually found in inorganic semiconductors. For this type of exciton, the radius of the electron-hole pair covers several molecules or lattice sites.

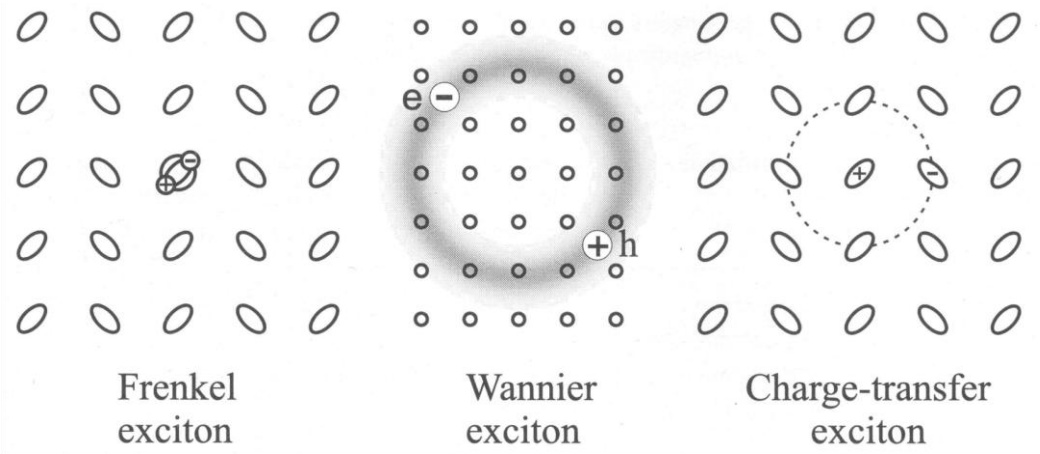

Figure 2.6 Schematic representation of Frenkel, Wannier and CT excitons. Frenkel excitons are localized on one molecule while Wannier and CT excitons are extended over several molecules. Reproduced with permission from reference[34].

A second type of exciton is the strongly localized Frenkel exciton with a radius of 1 - 3 nm [50]. In this case, the electron-hole pair resides on one molecular site. This type of

exciton is most commonly observed in organic semiconductors. The lifetime of Frenkel excitons can be rather long (ns to µs) and having the excitation a strong dipolar momentum, it can move through the solid by energy transfer (see Paragraph 2.6). A last type of exciton is called charge transfer exciton. In this case, the excited electron is (partially) transferred to a neighbouring molecule, but remains bound to the hole on the initially excited molecule. The charge transfer exciton is neutral, but has a pronounced dipolar character. A more specific concept is the exciplex, which describes a delocalized excitation over two neighbouring molecules from different species. Usually, the molecules involved in the formation of the exciplex possess strong electron donor and acceptor character, respectively. The energy of a CT exciton, E_{CT}, is given by

$$E_{CT} = I_D - E_A - P_{eh}(r) - C(r) \quad \textbf{(}2\text{-}25\textbf{)}$$

with the ionisation potential of the donor I_D, the electron affinity of the acceptor E_A, the polarisation energy $P_{eh}(r)$ of the surroundings, due to the electron hole pair with separation *r*, and the Coulomb attractive energy $C(r)$ between the electron and the hole. CT excitons are difficult to observe in optical measurements due to their weak oscillator strength [34] $f = 10^{-4} - 10^{-2}$.

So far, we have not addressed the influence of spin on these excitations. The strong electron-electron interactions in organic semiconductors lead to significant stabilization of the triplet state and a lifting of the degeneracy between singlet and triplet states. Since the triplet state consists of electrons with parallel spins and the Pauli principle excludes two electrons in the same orbital, the electrons in a triplet state have to occupy different orbitals. Therefore they are on average further separated, compared to singlet electrons. As a result, the energy of the triplet is lowered with respect to the singlet due to the reduced electron repulsion. The difference between the energies of singlet and triplet is given by the exchange integral [51,52]. Notably, since CT excitons are spatially more separated, the exchange interaction is lower compared to Frenkel excitons. This leads to a reduced splitting between singlet and triplet CT excitons, affecting the energetics and photophysics of the system. For example, the recombination of initial singlet Frenkel excitons to triplets might be enhanced by intersystem crossing in an intermediate CT exciton level [53].

2.4.2 Polarons

A charged state can be formed by addition/removal of an electron to/from the ground state of the molecule. The low electrostatic screening in organic semiconductors allows a polarisation of the material in the vicinity of the charge and a concomitant deformation of the molecular structure. A localized charge surrounded by a region of molecular distortion is formed. The quasiparticle describing the charge combined with the molecular deformation is termed polaron [54,55]. The general concept of a polaron was first introduced by Landau to describe an electron propagating in a polarizable lattice carrying the lattice deformation with its position [56] (Figure 2.7).

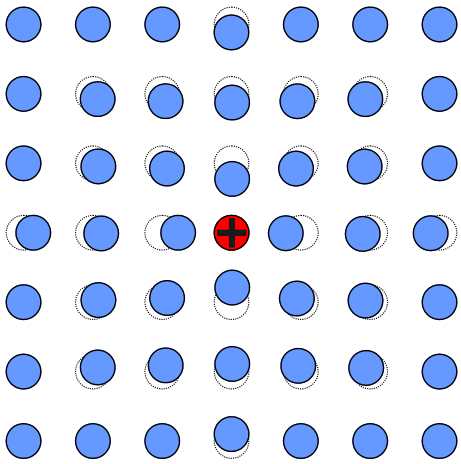

Figure 2.7 Schematic representation of a polaron. A positively charged particle (red) in a lattice of molecules (blue) polarizes the surroundings, which leads to displacement of the molecules from their equilibrium positions (circles). The entity of charge and lattice deformation is termed polaron.

Due to the strong coupling between charge and molecular vibrations in organic semiconductors, only the environment in the close vicinity of the charge is affected, leading to a "small" polaron. For the case of conjugated polymers the polaron involves a deformation of the bond lengths in the molecule, i.e. along the polymer backbone. Accordingly, a polaron has a certain polaron binding energy or reorganization energy, which is related to the deformation-induced energy and additionally leads to a self-localization of the charge. The energy levels of polarons are positioned between HOMO and LUMO level of the organic semiconductor (Figure 2.8). Additional optical transitions (P_1, P_2) are activated upon formation of polarons, allowing the investigation of these states with spectroscopic tools [57,58].

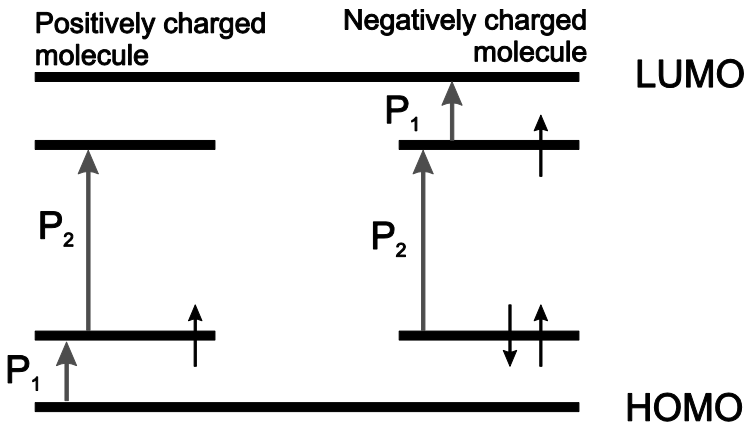

Figure 2.8 Schematic representation of polaron transitions for positively (radical cation) and negatively (radical anion) charged molecules. For the cation one electron is removed from the molecule while for anions an electron is added. Intraband transitions are indicated as P_1, while P_2 denotes interband transitions.

The P_1 transitions are in the energy region around 0.3 eV, while the P_2 transitions are in the near-infrared around 1 eV [59]. The energy of the P_1 transition is a measure for the relaxation in energy connected to the distortion of the molecular structure. It has been found that the energy of the P_1 transition is associated with the delocalization of the π-electrons and the delocalization length l_D can be related to the transition energy E_{P_1} based on $E_{P_1} \sim 1/l_D + const.$ [60]. Since polarons in organic semiconductors, in a chemical description, are similar to a charged molecule, the expressions radical cation (positively charged molecule) and radical anion (negatively charged molecule) are also used to describe polarons.

2.5 Optical transitions

The energy difference between the ground state S_0 and the first excited state S_1 of organic semiconductor molecules is usually in the range 1 - 3 eV, which enables excitation of transitions with visible light. This allows us to study the electronic structure of organic semiconductors with optical spectroscopic methods. Upon excitation with light, the molecule undergoes a transition from the ground state to an excited state. Eventually, emission might occur through the radiative relaxation of the excited state. We limit our discussion to the case of transitions between the ground state S_0 and the first excited state S_1. In Figure 2.9 the potential energy curves for the ground and excited state are shown versus the molecular configuration coordinate *Q*. Excitation

of the system leads to a reconfiguration of the electronic structure and a shift in the position of the nuclei. Therefore, the electronic potential of the excited state is shifted along the *Q* axis with respect to the ground state.

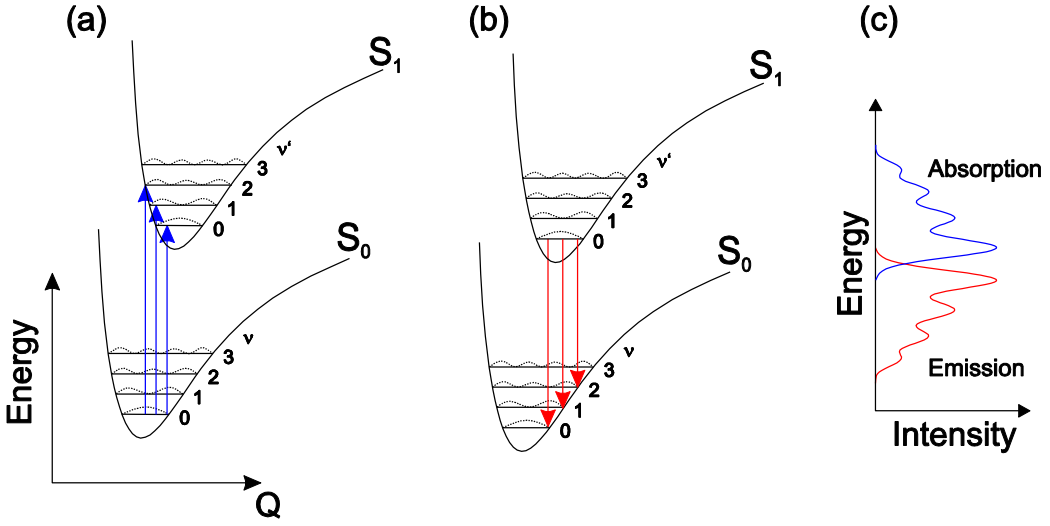

Figure 2.9 Energy diagram of the absorption (a) and emission (b) transitions (arrows) in a two level system. The energy potentials for ground and excited state S_0 and S_1 are plotted against the configuration coordinate Q. Vibrational modes are indicated as dotted lines and energy levels within the electronic potential. Exemplary absorption and emission spectra with vibronic progressions are shown in (c).

The small electron mass compared to the mass of the nuclei allows assuming that electronic transitions initially do not affect the nuclear configuration (Born-Oppenheimer approximation) and can be drawn as vertical lines in the energy diagram. Since molecules feature different vibrational modes ν, both, in the ground and excited state, transitions to these vibronic energy levels are possible. Absorption processes occur from the lowest vibronic level of the ground state, since the thermal energy at room temperature is not sufficient to populate the first vibrational mode $S_{0,1}$, about 100meV above the lowest energy level $S_{0,0}$. However, transitions to higher vibronic modes in the first excited electronic state are possible. These are visible as progressions above the energy of the $S_{0,0} \rightarrow S_{1,0}$ transition in the absorption spectrum (Figure 2.9c). The transition probability of vibronic transitions is ultimately determined by the wavefunction overlap for the initial and final state (Franck-Condon principle[61,62]). This is formally described by the following formula for the absorption coefficient

$$\alpha(\omega) \propto \omega \cdot \left| \langle \phi_f | \sum_j e\boldsymbol{r}_j \, | \phi_i \rangle \right|^2 \cdot \sum_N \frac{e^S S^N}{N!} \cdot \delta(\omega - \omega_{fi} - N\omega_{vib}) \qquad \textbf{(}2\text{-}26\textbf{)}$$

with the so called Huang-Rhys parameter *S*, the frequency of the absorbed light ω, the frequency of the vibrational mode ω_{vib}, the order of the vibrational mode *N* and the frequency correlating to the energy difference between initial and final state ω_{fi}. The last term indicates a delta function.

The derivation of Equation **(**2-26**)** is based on Fermi's Golden Rule for the transition rate k_{fi} between an initial state $|\psi_i\rangle$ and a final state $|\psi_f\rangle$

$$k_{fi} = \frac{2\pi}{\hbar} \cdot \left| \langle \psi_f | \sum_j e\boldsymbol{r}_j \cdot \boldsymbol{E}(t) \, | \psi_i \rangle \right|^2 \cdot \delta(E_f - E_i) \qquad \textbf{(}2\text{-}27\textbf{)}$$

with the electromagnetic field vector ***E(t)*** and the energies of the final and initial states E_f, E_i. The Franck-Condon principle is a direct consequence of the Born-Oppenheimer approximation. It has the effect, that changes in the nuclear wavefunction are neglected for the calculation of the transition dipole moment μ_{fi}. This leads to the simplified expression

$$\mu_{fi} = \langle \psi_f | \sum_j e\boldsymbol{r}_j \, | \psi_i \rangle = \mu_{fi}^e \cdot \langle \chi_f | \chi_i \rangle \qquad \textbf{(}2\text{-}28\textbf{)}$$

with the instantaneous overlap of the nuclear wavefunctions $\langle \chi_f | \chi_i \rangle$ and the purely electronic transition dipole operator μ_{fi}^e. The right hand side of the equation shows the factorization of the total vibronic wavefunction Ψ into the electronic ϕ and the vibrational part χ. Equation **(**2-26**)** is finally obtained by evaluating the overlap of the nuclear wavefunctions between the lowest vibrational state $N = 0$ and higher vibrational states *N*.

After excitation of an energy level $S_{1,v}$ non-radiative decay processes lead to a fast relaxation of the system to the lowest excited state $S_{1,0}$ on a time scale of 10^{-13} s [33,34,63,64]. Therefore, emission processes are usually observed from the lowest excited state $S_{1,0}$ only. Just like for absorption, transitions are also possible to vibronic levels of the ground state, giving rise to progressions at lower energies with respect to the $S_{0,0} \rightarrow S_{1,0}$ transition. This is illustrated in Figure 2.9c. Spontaneous emission can be

described by the Einstein spontaneous emission coefficient or again Fermi's Golden Rule. In both cases the transition rate is given by

$$A \propto \omega^3 \cdot \left| \mu_{fi}^e \right|^2 \sum_{m,n} \left| \langle \chi_{f,n} | \chi_{i,m} \rangle \right|^2 \cdot \delta\left(E_{f,m} - E_{i,n} - \hbar\omega\right). \qquad \textbf{(2-29)}$$

The spectral shift between absorption and emission maxima (Figure 2.9) is known as Stokes-Shift. The main reason for this effect lies in an energy loss due to relaxation of the molecule after excitation. Also solvent effects, excited state effects or energy transfer, e.g. in a broadened density of states, can play a role [65,66].

So far, we have considered only a simple two level system and did not take the spin of the excitation into account. The spin plays an important role in organic semiconductors and gives rise to singlet and triplet states, as discussed in Paragraph 2.4.1. A convenient way to represent the complete photo-physical processes is a so-called Jablonski diagram (Figure 2.10). It shows the ground state S_0 together with higher excited singlet states S_1/S_2 and also triplet states T_1/T_2. Each level splits further into vibronic levels due to coupling of the electrical states to molecular vibrations.

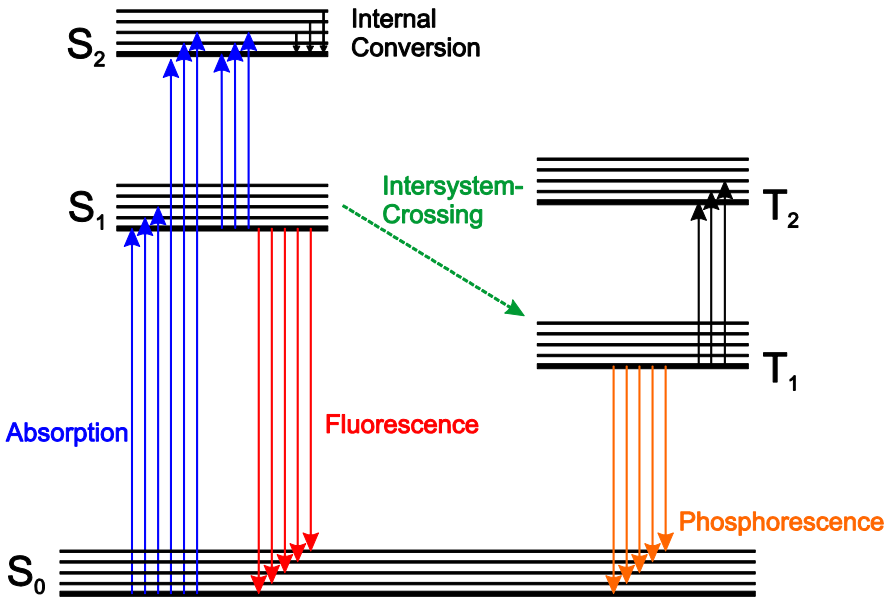

Figure 2.10 Jablonski diagram for the optical transitions in an organic semiconducting molecule. Singlet (S_i) and triplet levels (T_i) are shown together with absorption, fluorescence and phosphorescence. Intersystem crossing occurs between singlet and triplet levels.

Optical excitation from the ground state is only possible to excited singlet states due to spin conservation rules. Once a higher lying state S_i is created, fast non-radiative internal relaxation among the electronic excited states occurs on a ps-time scale until the first excited singlet state S_1 is reached (Kasha's rule) [32,33,67,68]. As discussed in Paragraph 2.4.1, the energy of triplets is lowered by twice the amount of the exchange integral compared to the singlet state [35,66], i.e. about 0.8 eV [51,69]. Formally, transitions from the singlet to triplet states are forbidden, since the spin conservation condition is not fulfilled. However, spin-orbit coupling can make these transitions weakly allowed and intersystem crossing occurs. For the same reason, the decay from the triplet to the ground state (phosphorescence) is weakly allowed, with lifetimes of about 10^{-6} to 10^{-2} s. On the other hand, the lifetimes corresponding to transitions from excited singlet states to the ground state (fluorescence), are in the region of 10^{-9} to 10^{-7} s. The transition from the S_1 state to separated charges (charge dissociation) is an additional process which is especially relevant for photovoltaic applications. A detailed discussion of this process is given in Paragraph 2.7.

2.6 Energy transport and exciton diffusion

The existence of long-lived neutral excitations (excitons) in organic semiconductors allows energy transfer between molecular sites. Energy transfer is of critical importance for photovoltaic applications using organic semiconductors, since the primary excitations in the polymer have to diffuse to the heterojunction between donor and acceptor for efficient charge separation. Exciton transfer processes are described by hopping of an exciton from one molecule to the other. Energy transfer can take place either between different types of molecules with donor and acceptor properties, or within the Gaussian broadened density of states of a pure organic semiconductor [63,70]. The physical property describing the range of energy transfer is the exciton diffusion length, which gives a value for the distance an exciton can travel before recombining. A typical method to experimentally determine values for the exciton diffusion length is the measurement of photoluminescence quenching in donor-acceptor bilayers as a function of layer thickness [71]. The obtained values depend on the investigated material and are, for example, in the range of 3 - 9 nm for P3HT films. The radiation-less energy transfer can either occur due to dipole-dipole interactions (Förster mechanism) or based on electron exchange interactions (Dexter mechanism).

In Förster theory [72,73] the transfer rate $k_{Förster}$ between a Donor (D) and acceptor (A) molecule is given by

$$k_{Förster} = \frac{1}{\tau_D}\left(\frac{R_0}{r_{DA}}\right)^6 \quad \textbf{(2-30)}$$

with the Förster radius

$$R_0 = \frac{3c^2}{4\pi n^2}\int_0^\infty \frac{f_D(\omega)\,\sigma_A(\omega)}{\omega^4}\,d\omega \quad \textbf{(2-31)}$$

and the distance between donor and acceptor r_{DA}, the radiative lifetime of the donor τ_D, the normalized emission spectrum of the donor $f_D(\omega)$, the absorption cross section of the acceptor $\sigma_A(\omega)$ and the frequency of light ω. The transfer rate shows a strong dependence on the donor-acceptor distance ($\propto {r_{DA}}^{-6}$). Additionally, substantial overlap of emission and absorption spectra of donor and acceptor is required. In most organic semiconductors the spectral overlap between absorption and emission is given, so that the distance dependence is the main factor limiting transfer.

The transfer rate in Dexter theory is determined by the electron exchange interaction [74]. Therefore, the wavefunction overlap between donor and acceptor is relevant and Dexter transfer only occurs at short distances between donor and acceptor [65], i.e. smaller than 1.5 nm. The formula for the Dexter transfer rate is

$$k_{Dexter} = J \cdot \exp\left(-\frac{2r_{DA}}{L}\right) \quad \textbf{(2-32)}$$

with the spectral overlap integral *J* of donor emission and acceptor absorption and the sum *L* of the Van der Waals radii of donor and acceptor. The last value is a measure for the spreading of the wavefunction into the surrounding environment.

As an important difference between the two mechanisms, in Förster theory the spin of the individual components has to be conserved independently, while for Dexter theory this conservation applies to the total spin of the system. Therefore, Förster mechanism does not allow singlet-triplet exciton transfer, while with Dexter mechanism also triplets can be transferred.

2.7 Photogeneration of charge carriers in donor-acceptor blends

The photogeneration of charges in organic semiconductors occurs in several steps. First, absorption of a photon creates an exciton, which diffuses to the interface between donor and acceptor regions. The boundary between donor and acceptor domains is called-heterojunction (Figure 2.11). For the case of a staggered offset in HOMO and LUMO levels of donor and acceptor, a type II-heterojunction is formed. When an electron is transferred from donor to acceptor, the downhill energy step from donor to acceptor LUMO provides additional energy. This energy is used to overcome the substantial exciton binding energy of organic semiconductors. After transfer to the acceptor the electron typically remains coulombically bound to the hole on the donor, creating a charge transfer exciton. This bound charge pair can either recombine or dissociate into free charges.

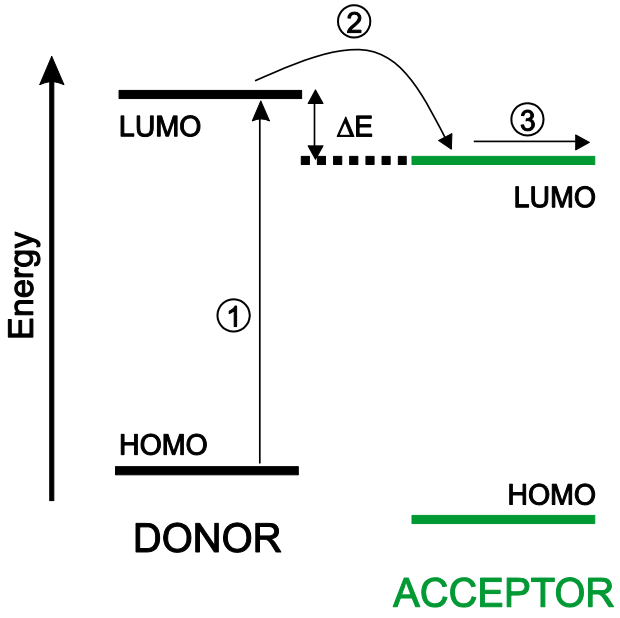

Figure 2.11 Schematic representation of the energy levels at a donor-acceptor heterojunction. Charge generation occurs in three steps: (1) Absorption of a photon and generation of a bound exciton in the donor domain. (2) Electron transfer from donor to acceptor at the heterojunction and formation of a CT exciton. The energy step ΔE at the heterojunction provides additional energy to separate the exciton. (3) Charge dissociation and diffusion of the separated charges from the heterojunction.

The main limitation for efficient separation of charges in organic semiconductors is the low screening of Coulomb forces due to the materials' low dielectric constant. A further complication is the low charge mobility in organic semiconductors, which is discussed

in Paragraph 2.8. The present paragraph will give an overview on the theories related to the charge dissociation process, i.e. the escape of the bound charge pairs from the common Coulomb potential, leading to free charge carriers. For a more detailed treatment of this topic, the reader is referred to the literature [32,34,35,75].

2.7.1 Marcus theory of charge transfer

To describe the escape of the bound charges from the Coulomb potential, first a microscopic theory of charge transfer between molecules is necessary. The standard quantum theoretical formulation of the charge transfer between molecules is Marcus theory [76,77]. One assumes the charge transfer from an initial state (reactant) to a final state (product). The charge transfer probability can be derived from Fermi's golden rule under the Franck-Condon approximation:

$$k_{ET} = \frac{2\pi}{\hbar} \cdot |\langle \phi_R | H | \phi_P \rangle|^2 \cdot |\langle \chi_R | \chi_P \rangle|^2 \cdot \delta(E_R - E_P) \quad \textbf{(}2\text{-}33\textbf{)}$$

It depends on the vibronic states of reactant and product $|\phi_R\rangle$ and $|\phi_P\rangle$, the overlap between the vibrational states $|\chi_R\rangle$, $|\chi_P\rangle$, and the energies of product and reactant E_P, E_R. One can approximate the vibronic states as harmonic oscillators and treat the inter-molecular vibrational modes classically, which leads to the formulation of semi-classical Marcus theory:

$$k_{ET} = \frac{2\pi}{\hbar} \cdot H_{RP}^2 \cdot \left(\frac{1}{4\pi\lambda_0 kT}\right)^2 \cdot F(\omega, T) \quad \textbf{(}2\text{-}34\textbf{)}$$

with the electronic coupling term H_{RP}^2, the medium reorganization energy λ_0, the temperature *T* and

$$F(\omega, T) = \sum_{m=0} \rho(m) \sum_{n=0}^{\infty} exp(-S) \frac{S^n}{n!} exp\left(\frac{-(\lambda_0 + (m-n)\hbar\omega + \Delta G_0)^2}{4\lambda_0 kT}\right). \quad \textbf{(}2\text{-}35\textbf{)}$$

Equation **(**2-34**)** describes the charge transfer between a reactant molecule in the ground state and product molecule with several vibrational modes (Figure 2.12). The Franck-Condon factor $F(\omega, T)$ takes into account the sum of all vibration overlap integrals between reactant ground state and product excited modes *m*,*n*. The effective electron-phonon coupling is described by the Huang-Rhys parameter *S*. The last term in Equation

(2-35**)** is a Boltzman expression for the probability to obtain the necessary activation energy to overcome the difference in Gibbs free energy ΔG_0 between reactant and product. The reorganization energy λ_0 refers to the energy difference between reactant and product configurations. It contains an inner component related to changes in the molecules' nuclear geometry and an outer component related to changes in the configuration of the surroundings. Higher excited modes of the reactant are considered by summation over vibrational modes *m*, each with an activation density $\rho(m)$. Marcus theory shows how vibrational excess energy can help dissociating charge carriers by compensating Coulomb binding or reorganization energy as seen in Equation **(**2-35**)**. Additionally the activation of higher-lying vibrational modes of the reactant can lead to better overlap with modes of the product and to fast and efficient charge transfer. This interpretation is supported by the observation of fast formation of free charges in organic semiconductors [78–80]. As a more basic alternative to Marcus theory, Miller-Abrahams theory [81] is sometimes used for the calculation of charge transfer processes in transport theories.

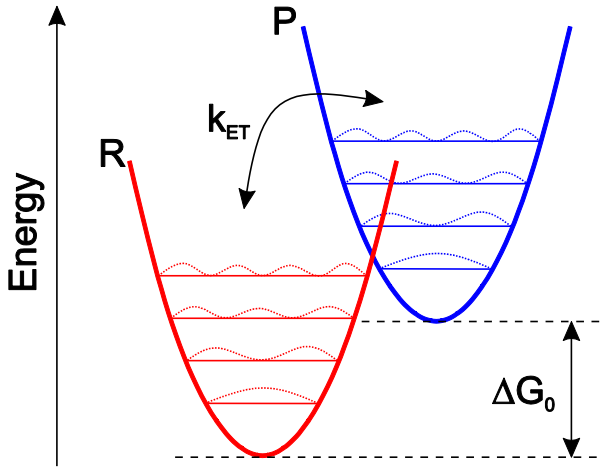

Figure 2.12 Schematic representation of the charge transfer between a reactant (R) and product (P) molecule. Higher vibrational modes are shown as horizontal lines within the harmonic potential. The energy difference between the reactant and product is the Gibbs free energy ΔG_0.

2.7.2 Onsager-Braun theory of charge dissociation and recombination

The macroscopic description of the charge dissociation process is based on the discussion of charge separation rates. The fundamental theory was developed by Onsager and deals with the escape of ions from their mutual Coulomb potential [82,83].

The theory assumes that the ions form a bound charge pair attracted by a Coulomb force. Additionally, the medium is considered to consist of only one type of molecule. Any influence of an external field on the initial formation of the bound charge pair is neglected. The binding energy of the charge pair at a distance r_B is calculated from

$$E_B = \frac{e^2}{4\pi\epsilon\epsilon_0 r_B} \tag{2-36}$$

with the elementary charge *e*, the dielectric constant ε and the electric field constant ε_0. Onsager theory calculates the probability that a thermalized charge pair dissociates under the influence of an external field *F*. The theory is based on the concept of Brownian motion of a charge carrier in the Coulomb potential of a second, oppositely charged carrier with a superimposed external electrical field. The polaron pair is generated from a higher excited state S_2 which can either form charge pairs or relax non-radiatively to a lower state S_1 (Figure 2.13).

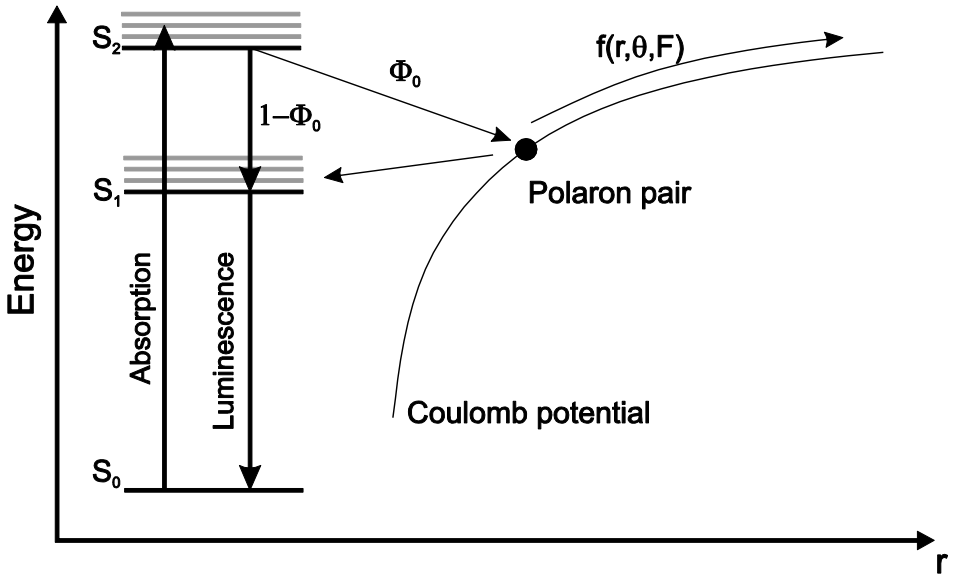

Figure 2.13 Schematic representation of the charge carrier dissociation process in Onsager theory. The polaron pair is formed from a higher excited state S_2 with a probability Φ_0 and consequently escapes the Coulomb potential with a probability f(r,θ,F).

Under the assumption of a homogeneous system with a low density of charge pairs, so that interactions between them can be neglected, the following expression for the dissociation probability is obtained:

$$f(r,\theta,F) = \exp(-A)\cdot(1+A\cdot B) \quad \textbf{(2-37)}$$

with

$$A = \frac{2e^2}{8\pi\epsilon\epsilon_0 kT}\cdot\frac{1}{r} \quad \textbf{(2-38)}$$

and

$$B = r\cdot\frac{eF}{2kT}(1+cos\theta)\,. \quad \textbf{(2-39)}$$

The dissociation probability depends on the initial distance vector between the charges ***r*** and the angle θ between ***r*** and the applied electrical field ***F***. The total carrier quantum yield Φ is obtained by integration over space, with the probability per unit volume *g(**r**,θ)* to find the free electron in the volume *dV*, and the initial quantum yield of charge pairs per absorbed photon Φ_0:

$$\Phi = \Phi_0\cdot\int g(\boldsymbol{r},\theta)\cdot f(\boldsymbol{r},\theta)\,dV \quad \textbf{(2-40)}$$

Onsager theory was further extended by Braun [84] to the case of the field-assisted ionization in *donor-acceptor* systems. This was necessary since the thermalization distances calculated from Onsager theory for this case were substantially too large, compared to experimental observations [85]. The Onsager-Braun model considers an initially generated charge transfer state CT_1 in thermal equilibrium with free charges D^+/A^-. Unlike in Onsager theory, the charges do not recombine immediately when they meet. The CT state has a finite lifetime during which several dissociation attempts are possible before recombination eventually occurs. The decay rate of the CT_1 state to the ground state *DA* is finite and given by k_f:

$$DA \xleftarrow{k_f} CT_1 \xleftrightarrow{k_d} D^+ + A^- \quad \textbf{(2-41)}$$

With this model the probability for dissociation of a CT state is

$$P(F,T,r) = \frac{k_d(F)}{k_f + k_d(F)} \quad \textbf{(2-42)}$$

In this equation, *F* stands for the electric field, *T* for the temperature and *r* for the separation of the charge pair. The decay rate to the ground state k_f can be determined from fluorescence lifetime experiments. The final expression for $k_d(F)$ derived from Onsager-Braun theory is [84]

$$k_d(F) = \frac{3\langle\mu\rangle e}{4\pi\epsilon_0\langle\epsilon\rangle r^3} exp\left(\frac{-\Delta E}{kT}\right)\left(1 + b + \frac{b^2}{3} + \frac{b^3}{18} + \cdots\right). \quad \textbf{(2-43)}$$

In this equation $\langle\epsilon\rangle$ and $\langle\mu\rangle$ are the spatially averaged dielectric constant and electron/hole mobilities, respectively. The argument *b* in the expansion is

$$b = \frac{e^3 F}{8\pi\epsilon_0\langle\epsilon\rangle k^2 T^2}. \quad \textbf{(2-44)}$$

The expression for ΔE depends on the model used to describe the CT state, e.g. for an ion-pair model as in Onsager theory it can be written as

$$\Delta E = \frac{e^2}{4\pi\epsilon_0\langle\epsilon\rangle r} \quad \textbf{(2-45)}$$

In the last step, the dissociation rate has to be integrated over the distribution of charge pair separation distances, to obtain the probability of charge pair dissociation:

$$P(T,F) = \int_0^\infty P(r,T,F)\cdot f(r)dr \quad \textbf{(2-46)}$$

The exact expression for the distribution of charge pair distances, *f(r)*, depends again on the specific case, but is often assumed to be a Delta or Gaussian function. The comparison of Onsager-Braun theory with experiments shows better agreement of thermalization radii and temperature dependence, compared to the pure Onsager model. Interestingly, at low temperatures disorder helps dissociating the charge pairs and has the effect of a lower activation energy for dissociation [87,88]. However, as a severe limitation, it is still not possible to exactly predict the thermalization distance, i.e. the initial separation of the relaxed CT exciton. As a further restriction, changes in entropy are usually not taken into account. For the case of charge carriers bound at an interface, as in organic semiconductor heterojunctions, the separation from the opposite charge and the interface leads to an increase in the degrees of freedom and accordingly to an

increase in entropy. This affects the value for Gibbs free energy, used in Marcus theory to describe the individual charge transfer steps. So far, the possible beneficial effect of entropy on charge transfer has not yet obtained substantial investigation. Another deviation from theory is found in the temperature independence of the dissociation yield for weakly disordered polymers [89]. Also the effect of an initially excited state, e.g. a "hot" CT exciton, cannot be described. However, this case is of importance, because the excess energy of the system might facilitate charge separation by bringing the system closer to the dissociation energy. In conclusion, there still remain open questions concerning the exact mechanism of charge dissociation in organic semiconductors. Particularly, the exact influence of the CT exciton thermalization radius on charge dissociation has not yet been clarified.

2.7.3 Role of charge transfer excitons

From Onsager-Braun theory, outlined in the previous Paragraph 2.7.2, it is evident that CT excitons play a critical role in the charge separation process as intermediate states between Frenkel excitons and free charge carriers. The role of CT excitons has been investigated in both, theoretical and experimental studies [90,91].

Experimentally, evidence for CT excitons was found by measuring the thermal dissociation energy. A constant dissociation energy was observed for a considerable range of excitation energies. This suggests that the initial excitation loses energy by internal conversion and relaxes to an intermediate state from which ionization occurs. In general, the low oscillator strength complicates the spectroscopic investigation of charge transfer excitons. However, it is possible to detect a weak ground state absorption with photo-thermal deflection spectroscopy [92,93]. It was shown, that the excitation of CT excitons with below gap energies, i.e. without initial formation of Frenkel excitons, is possible and leads to the formation of charge carriers [94,95]. However, these polarons are not yet completely separated. Recent findings highlighted, that also the weak emission of CT excitons can be studied in photoluminescence [96–98] and electroluminescence [99,100] measurements. Typically, the emission band of CT excitons is red-shifted with respect to the Frenkel exciton emission and not present in either of the pure materials' emission spectra. The correlation between reduced CT exciton emission intensity and increased photovoltaic performance, as shown by Hallermann *et al.* [101], underlines the importance of CT excitons in the charge generation process.

Additionally, a linear relation between open circuit voltage of solar cells and the energy of the CT exciton emission band has been found [100,102], which further highlights CT excitons as an intermediate step in charge generation. Since CT excitons are formed at the interface between donor and acceptor regions, the morphology of the blend has an impact on the CT exciton population. Increased CT exciton emission has been observed in blend films with intermixed, compared to a more phase-separated, morphology [103].

The decay of CT excitons either occurs to the ground state, a lower-lying triplet state or results in dissociation to free charges. The transfer rates between the different levels are given by the energy difference and the overlap integral of the involved orbitals [104,105]. Experimentally, the decay of CT excitons can be studied from transient photoluminescence measurements [106,107]. Notably, one finds a discrepancy between the CT lifetimes used in Monte-Carlo simulations of photovoltaic cells (1-100 ns) and the experimentally observed values (several hundred ps). This underlines the problem that CT exciton dissociation is not yet fully understood in physical and quantitative terms. Further experimental investigations on the role of CT excitons in charge separation are necessary.

Theoretically, Huang *et al.* [108] found that for polymer-polymer systems a range of CT excitons exists. These show emitting, as well as non-emitting properties. The structure of the individual states depends on the geometry of the molecules, i.e. the intermolecular interactions. The more specific concept of a CT exciton is an exciplex. Eventually the relative contribution of ionic and excitonic terms defines the properties of the exciplex [109,110]. The character of an exciplex can vary from almost purely ionic to purely excitonic, depending on which contribution dominates the exciplex wavefunction. Decay rates between electronic states are based on the coupling matrix elements. It has been shown that the composition of the exciplex wavefunction defines the possible decay channels [105,109]. Since the wavefunction overlap influences the character of the CT exciton, the molecular packing, i.e. the film morphology, plays a significant role on the properties of the CT excitons [103,111]. Theoretical modelling of organic semiconductor morphologies has to deal with a complex system of molecules which interact through Van der Waals and electrostatic interactions. Therefore, full modelling of a disordered organic semiconductor system is a very challenging task and makes theoretical statements about CT excitons difficult [91]. In conclusion, full understanding of the charge separation process and the role of CT excitons therein is still missing, and will be one topic of the work presented in this thesis.

2.8 Charge transport in disordered systems

In photovoltaic applications, extraction of charges after separation is an important step for efficient operation. The microscopic description of charge transport between molecules is again Marcus theory as detailed in Paragraph 2.7.1. Macroscopic models for charge transport in disordered media have been developed by Bässler *et al.* based on a hopping transport model and Monte-Carlo simulations[112–115]. In this model, a Gaussian distribution of energy levels with width σ is assumed for the localized polaron, leading to a distribution of energy levels and transfer rates. This type of disorder is called diagonal disorder. The transfer between sites is based on a hopping motion of charge carriers, equivalent to a tunnelling process through an energy barrier. Therefore mobilities in disordered media are generally orders of magnitude lower than in crystalline materials. In the Monte-Carlo simulations, the transfer rate between two sites is expressed by the Miller-Abrahams formulation [81]

$$\nu_{ij} = \nu_0 \exp\left(-2\gamma\Delta R_{ij}\right) \begin{cases} \exp\left(-\dfrac{E_j - E_i - eF\left(x_j - x_i\right)}{kT}\right) & if\ E_j > E_i \\ 1 & if\ E_i \geq E_j \end{cases} \quad \textbf{(2-47)}$$

where E_i and E_j are the energies of the transport sites, F is the applied field, ΔR_{ij} is the distance between the sites and γ, ν_0 are constants. Disorder leads to a distribution of overlap parameters $2\gamma\Delta R_{ij}$. This type of disorders is termed non-diagonal, since it depends on the disorder of two molecules, i.e. initial and final charge transfer sites. Expression **(**2-47**)** takes into account that for downward jumps in energy no activation is necessary and therefore the exponential term equals one. The Bässler model cannot be solved analytically, so Monte-Carlo simulations have been employed and show good agreement with experimental results [47,112,113]. The findings obtained from the simulations show that after excitation charges relax in the density of states to an equilibrium energy which is given by

$$\langle E \rangle = -\frac{\sigma^2}{kT}. \quad \textbf{(2-48)}$$

with the width of the Gaussian distribution of energy levels σ, the temperature *T* and the Boltzmann constant *k*. This expression is equivalent to a thermal activation energy $\langle E \rangle$ for charge transport.

The mobility in disordered organic semiconductors according to the Bässler model is then

$$\mu(\sigma, \Sigma, F, T) = \mu_0 \exp\left\{-\left(\frac{2\sigma}{3kT}\right)^2 + C\left[\left(\frac{\sigma}{kT}\right)^2 - \Sigma^2\right]\sqrt{F}\right\} \quad \textbf{(2-49)}$$

which shows the experimentally observed $\mu \propto \exp(\sqrt{F})$ proportionality [86]. Typical measurement techniques for charge transport are time-of-flight or field-effect transistor studies. Mobilities in the range of $\mu_h = 10^{-3}\ \mathrm{cm^2V^{-1}s^{-1}}$ for holes and $\mu_e = 10^{-5}\ \mathrm{cm^2V^{-1}s^{-1}}$ for electrons [116,117].

Besides the organic material itself, also the contact between the electrodes and the organic semiconductor affects the charge transport when measured in electronic devices. In the case of a contact providing fewer electrons than the organic semiconductor can transport, the current is limited by the injection of electrons into the material. This case is termed injection limited current. On the other hand, for an Ohmic contact between electrode and semiconductor charge transport is limited by the mobility in the organic. This leads to an increasing build-up of charge near the electrode with increasing voltage, since the charges are transported through the material with a lower rate compared to the injection rate. A space charge region is formed. This is the case of space-charge limited currents giving rise to the following dependence of current density *j* on voltage *V*

$$j = \frac{9}{8}\epsilon\epsilon_0\mu\frac{V^2}{d^3} \quad \textbf{(2-50)}$$

with the thickness of the sample *d* and the dielectric constant of the material ϵ.

2.9 Basic principle of solar cell operation

This paragraph gives a short overview on the working principle of solar cells. The total efficiency of a solar cell is given by the product of the efficiencies for the individual

steps of operation: absorption of photons (η_{abs}), dissociation of excitations into free charges (η_{diss}), charge transport (η_{trans}) and charge extraction (η_{extr}):

$$\eta = \eta_{abs} \cdot \eta_{diss} \cdot \eta_{trans} \cdot \eta_{extr} \qquad (2\text{-}51)$$

The theoretical limit for power conversion efficiency is 33.7% for a simple p-n-junction as calculated from Shockley and Queisser in 1961[118]. In the last years, a new class of low-bandgap polymers, which cover a broader part of the solar spectrum, has been employed to advance solar cells efficiencies [119–121]. The efficiency record for a solar cell with organic semiconductors in a single junction is currently set at 9.3%, achieved from the South China University of Technology in cooperation with Phillips 66 and Solarmer [122]. Higher efficiencies of 10.7% have been reached with multi-junction cells [7]. For the characterisation of solar cells the current density *j*, measured under illumination with a solar simulator, is plotted against the voltage *V* (Figure 2.14).

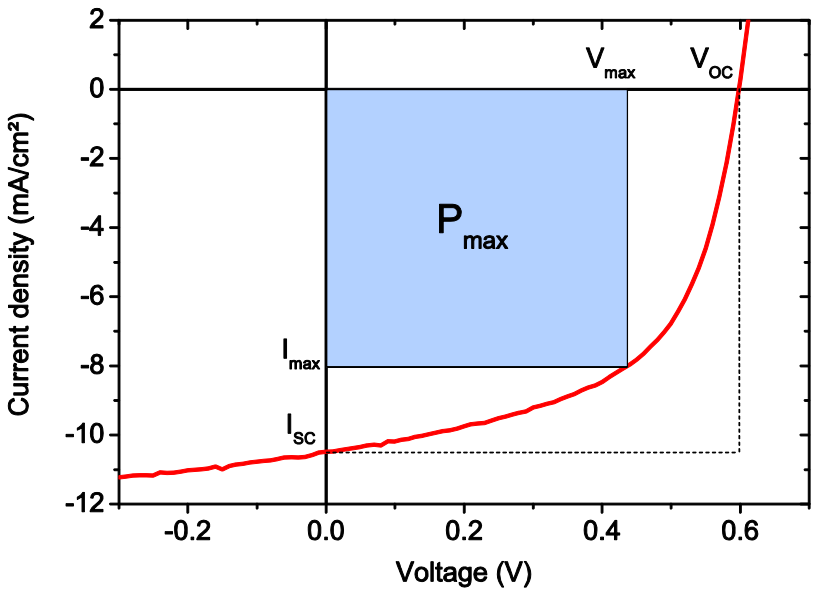

Figure 2.14 Exemplary IV-curve of a PCPDTBT:PCBM (1:1) solar cell measured under AM1.5 solar simulator irradiation and inert conditions. The intersection points with the horizontal/vertical axis are the open circuit voltage V_{OC} and short circuit current I_{SC}, respectively. The blue shaded area describes the maximum power P_{max} extractable from the solar cell, defined by the voltage and current at the maximum power point (V_{max}, I_{max}).

The key parameters of a solar cell are the open circuit voltage V_{oc}, the short circuit current I_{sc} and the fill factor *FF*. The intersection points with the horizontal/vertical axis are the open circuit voltage V_{OC} and short circuit current I_{SC}, respectively. The V_{oc} is a measure for the electrical potential in the cell and is related to the offset between donor

HOMO and acceptor LUMO. On the other hand, the I_{sc} is connected with the number of photo-generated charges. The fill factor *FF* reflects the amount of charge recombination and is defined by

$$FF = \frac{P_{max}}{V_{oc} I_{sc}} \quad \textbf{(}2\text{-}52\textbf{)}$$

with the maximum power extractable from the solar cell $P_{max} = V_{max} I_{max}$. Geometrically, P_{max} is defined by a rectangle with one corner at the origin and the other at the so called maximum power point on the IV-curve (blue shaded area in Figure 2.14). The stronger recombination effects are, the lower the value of the fill factor will be. The eventual power conversion efficiency is calculated from these values as

$$\eta = \frac{V_{oc} I_{sc} FF}{P_{in}} \quad \textbf{(}2\text{-}53\textbf{)}$$

with the incident photon flux P_{in} from the sun or solar simulator. The detailed discussion of further, more applied parameters influencing solar cell performance, e.g. film morphology or solar cell geometry, is beyond the scope of this thesis. For this, the reader is referred to the seminal literature [23,25,123,124] and references therein.

3 Materials and Experimental Methods

3.1 Materials

3.1.1 PCPDTBT

PCPDTBT (Poly[2,1,3-benzothiadiazole-4,7-diyl[4,4-bis(2-ethylhexyl)-4H-cyclopenta [2,1-b:3,4-b']dithiophene-2,6-diyl]]) is an example of the recent class of so called low-bandgap polymers. The characteristic feature of these polymers is a reduced energy gap between HOMO and LUMO compared to standard organic semiconducting polymers. This class of polymers has recently found interest due to its possible use in photovoltaic applications. The main difference to standard organic semiconducting polymers consists in the backbone of the polymer, which is build up from electron accepting (acceptor) and electron donating (donor) moieties. In the case of PCPDTBT the donor is a dialkyl-cyclopentabithiophene unit, while the acceptor is a benzothiadiazole. One repeat unit of the polymer is shown in Figure 3.1.

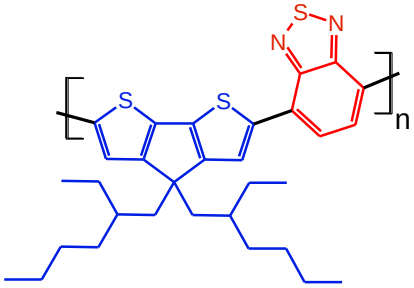

Figure 3.1 Chemical structure of one monomer unit of the low-bandgap conjugated co-polymer PCPDTBT constituted of a bithiophene donor (blue) and a benzothiadiazole acceptor (red) unit.

The combination of donor and acceptor moieties in one polymer leads to a reduced band gap, due to intra-molecular charge transfer, reduced bond-length alterations [125] and stabilization of the low-bandgap quinoidal forms of the polymers [126]. For PCPDTBT, the energies for HOMO and LUMO are at -4.9eV and -3.5eV respectively, which leads to a band gap of 1.4eV [127]. This value is close to the optimum bandgap of 1.5 eV for photovoltaic applications in polymer-fullerene blends, as shown in theoretical

calculations [128]. PCPDTBT has been used in several studies together with soluble fullerene derivatives for photovoltaic applications and efficiencies up to 5.5% have been reported [121,129,130]. The main limiting factor for higher efficiencies is the strongly intermixed morphology between PCPDTBT and PCBM, which limits charge extraction. However, it has been shown recently that the use of additives promotes a more favourable morphology [130,131]. In the low-bandgap polymer PCDTBT internal photo-conversion efficiencies as high as 100% have been found [119].

3.1.2 P3HT

Polythiophenes are one of the model systems for organic polymer semiconductors [132]. Since polythiophenes with more than 10 monomers are insoluble in common organic solvents, it is necessary to substitute them with side chains. Poly-3-hexyl-thiophene (P3HT) is one of the most common thiophene polymers and has been under investigation for many years now. The energy levels of HOMO and LUMO are at -5.1 eV and -3.2 eV, respectively [127]. In order to achieve high charge conductivities a regioregular head-tail configuration is beneficial. A synthesis protocol by McCullough [133,134] allowed to obtain this special chemical structure, leading to a very high regioregularity of above 95% and conductivities of up to 1000 Ω^{-1} cm^{-1}. Figure 3.2 shows the chemical structure of regioregular P3HT.

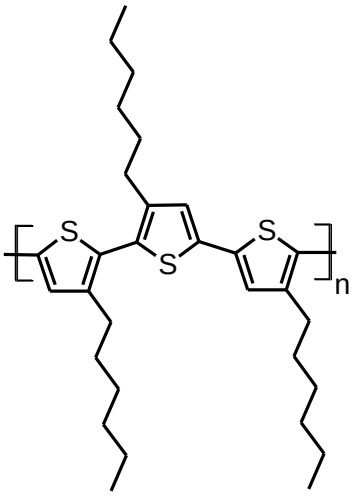

Figure 3.2 Chemical structure of three repeat units of the regioregular type of the conjugated polymer P3HT with alternating head-to-tail configuration.

Films of P3HT exhibit a mixture of crystalline and amorphous regions. In the crystalline regions, stacks of P3HT with a spacing of 3.8 Å in z-direction are found, leading to π-π-stacking of the thiophene rings and delocalization of the electron density. In the x-y direction the chains form lamellar structures with a spacing of 16 Å between individual polymer chains. Molecular weight and processing conditions critically affect the formation of ordered domains, which influences the conductivity [135,136]. Dilute solutions of region-regular P3HT show a broad featureless absorption around 2.7 eV, and a structured emission with a main peak around 2.15 eV featuring vibronic transitions [137]. An increase in concentration leads to the formation of a new band in absorption at an energy of about 2.1 eV, which can be correlated to a planarization of the polymer chains and the formation of crystallites. The strength of this transition is a measure for intermolecular interactions and is especially strong in films. The use of P3HT together with PCBM in solar cells for moderate efficiencies around 3-4% is known since several years and defines a model system for polymer-fullerene solar cells [138,139]. Notably, the solar cell efficiency is increasing with regio-regularity. This effect is related to an increase in absorption and mobility. Heating the solar cell to about 130 °C increases the size of the crystalline domains, which leads to a higher charge carrier mobility and a better cell performance. The best efficiencies have been obtained by using mixtures of P3HT molecules with high and low molecular weight [138].

3.1.3 PCBM(60)

Phenyl-C61-butyric acid methyl ester (PCBM) is a derivative of C60 (fullerene) and belongs to the class of small molecule organic semiconductors. Figure 3.3 shows the chemical structure of PCBM60. The main part of the molecule is the football shaped buckyball structure made of 60 carbon atoms arranged in a cage-like structure. Solubility in many organic solvents is given by the attached phenyl-butyric acid side group. Fullerene derivatives are one of the most common organic semiconductor acceptor materials and have been widely studied [140–142], especially for photovoltaic applications in combination with various organic polymers as donators [22,25,143–145]. The present section will therefore only give an overview of the most prominent features and refers the reader to the referenced seminal literature for further information. The position of HOMO (-6.1 eV) and LUMO (-4.3 eV) [127] levels leads to the formation of a type-II heterojunction with most organic semiconducting polymers which is a prerequisite for efficient charge separation. The good photovoltaic performance of

PCBM(60) as acceptor material is partially based on the high mobility values for electron transport [146,147]. It has been shown that the reason for the large mobility values lies in the very ordered morphology of PCBM domains [148–152].

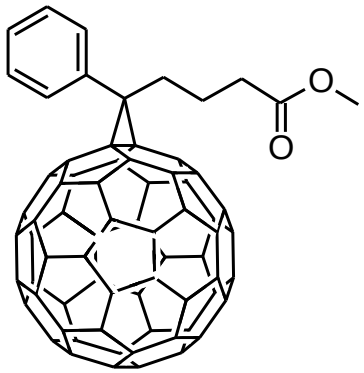

Figure 3.3 Chemical structure of PCBM(60) showing a buckyball geometry consisting of 60 carbon atoms. The phenyl-butyric acid side group allows solubility in organic solvents.

The spectroscopic properties, e.g. absorption and emission, of PCBM(60) have been investigated in detail [153–158]. In this respect, one significant limitation of PCBM(60) is the observation of no significant absorption above 340 nm, which is not optimal for a good coverage of the solar spectrum necessary for efficient solar cells. In the last years, the new fullerene derivative PCBM(70) with 70 carbon atoms forming an egg-shaped buckyball has found attention due to its extended absorption in the visible part of the solar spectrum. The photoluminescence from PCBM(60) is usually strongly suppressed. This is explained by the dipole forbidden transition between the highest occupied electronic level and the lowest unoccupied level. The charge generation process in combination with multiple organic conjugated polymers has been experimentally studied in detail from spectroscopic methods [80,95,159]. Ultra-fast charge transfer from the polymer to the fullerene has been observed which makes charge transfer favourable over other competing processes like, e.g. radiative decay. This is a further factor for the high efficiencies observed in polymer:fullerene blend solar cells.

3.1.4 F_4TCNQ

F_4TCNQ (2,3,5,6-Tetrafluoro-7,7,8,8-tetracyanoquinodimethane) is an electron accepting, small molecule (Figure 3.4). It is a fluorinated derivative of TCNQ

(tetracyanoquinodimethane). The modification with electronegative fluorine atoms increases the electron accepting character, as already known from other similar molecules [160]. The strong electronegativity of F_4TCNQ can be used to dope various materials, like graphene [161,162], small molecules [13] or conjugated polymers [10,11]. The origin of the strong electron accepting nature lies in the low value of the LUMO level (-5.2 eV). Accordingly, the HOMO level is at -8.3 eV. So far, the most common processing method for thin films of F_4TCNQ is thermal evaporation, but also dissolution in organic solvents is possible at elevated temperatures [163].

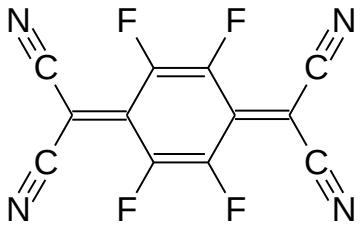

Figure 3.4 Chemical structure of one F_4TCNQ molecule with strong electron acceptor properties. The molecule can be used to p-dope conjugated polymers and increase the background hole density.

Due to the substantial dipole moment of F_4TCNQ, strong interactions with other materials have been observed, leading to clustering already in solutions and a gel-like aggregation. The addition of small amounts of dimethyl sulfoxide (DMSO) in solution reduced the aggregation for mixtures with the conjugated polymer MEH-PPV [10]. This effect was assigned to the screened electrostatic interaction between the molecules by DMSO. F_4TCNQ molecules exhibit a weak, narrow optical absorption around 390 nm [164]. No further significant optical transitions, e.g. emission, have been observed. The TCNQ variation of F_4TCNQ has been extensively investigated in molecular donor-acceptor crystals together with the donor TTF as an exemplary system for donor-acceptor complexes [165–167].

3.2 Sample fabrication

3.2.1 Solution preparation

All materials were received as powder and used without further purification. For processing into thin films, the materials were dissolved in organic solvents (spectroscopic grade, anhydrous). The solutions were stirred for several days on a hotplate. All vials were closed with a sealed cap and *Parafilm©* to minimize solvent evaporation, which would lead to changes in the solution concentration.

3.2.2 Spin-Coating

Thin films (~100nm) of organic semiconductor on various substrates were prepared using the spin-coating technique. The substrates were chosen based on the transmission properties required for the respective experiments. Most optical experiments were either conducted with round quartz substrates (*Ø20mm, Hereaus, Suprasil*) or rectangular coverslips (*15mmx15mm, Menzel-Gläser, #5*). CaF_2 substrates were used for transient absorption measurements with probe energies in the mid-IR. For SEM measurements, silicon wafers without thermal oxide were cut to obtain substrates of about 10 mm x 10 mm size. Before film deposition, all substrates were cleaned in an ultrasonic bath for at least 10 minutes in acetone and isopropanol. Afterwards, the substrates were washed once more with acetone and isopropanol and blown dry in a nitrogen stream.

The spin-coating process consists of four steps. First, a substrate is fixed on a vacuum holder. Next, a small amount of solution is dropped on the substrate with a pipette. Depending on the substrate size, 50-100 µl of solution was used. The substrate is set into rotation, thereby hurling away most of the solution until only a thin film is left. Under these conditions, the solvent evaporates fast, leaving a homogeneous thin film of material deposited on the substrate. Rotation speeds had to be adapted for the different solvents and were between 1000 and 3000 RPM with a spinning time of 30-60 s.

3.2.3 Doctor-blading

For the preparation of doctor-bladed samples a homebuilt doctor-blader was used. The basic setup is shown in Figure 3.5. A blade with a sharp, straight edge is placed less one

millimeter above the substrate. The blade edge has to be parallel to the substrate surface to avoid any unwanted variations of film thickness over the substrate length.

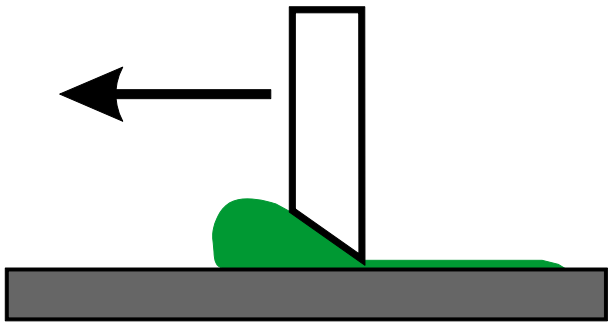

Figure 3.5 Scheme of the doctor-blading setup. The substrate is shown in grey, the organic semiconductor solution in green and the blade is white with black border. The arrow indicates the movement of the blade, which is spreading out the solution on the substrate.

With a pipette a small amount of solution (~5-10 µl) was placed on the substrate close to one side of the blade. By moving the blade over the substrate with a motorized stage (*Thorlabs MTS50/m-Z8 with TDC 001*) the solution was spread homogeneously, creating a thin film of solution. A slow blade speed (0.5 mm/s) was chosen to allow instantaneous drying of the thin solution film behind the blade. The blade movement was stopped before the edge of the substrate and residual solution was removed with a dust free wipe. The blade was cleaned after each run to avoid any cross contamination. The doctor-blading technique allows creating thin (~100 nm) homogeneous films on substrates with various dimensions, which was a requirement for our SEM sample size of 10 mm x 10 mm.

3.2.4 Solar cell fabrication

Solar cells are prepared from solution on glass substrates. A scheme of the cell geometry is shown in Figure 3.6. ITO coated float-glass substrates were bought from *Präzisions Glas & Optik GmbH* (*CEC010S*, 15 mm x 15 mm, sheet resistance ≤ 10Ω/sq.) and used as received. A two millimetres strip of ITO was etched away with HCl (37%) and zinc powder. Afterwards, the substrates were sonicated in distilled water, acetone and isopropanol for 10 min each. Finally, the substrates were cleaned for 5 min in oxygen plasma to remove any organic residue. In the next step, a PEDOT:PSS layer was spin-coated in ambient conditions and dried at 150 °C for 10 min. After

transfer to a nitrogen filled glovebox the active layer was spin-coated onto the samples from organic solvent solution. In the last step, aluminium electrodes were evaporated.

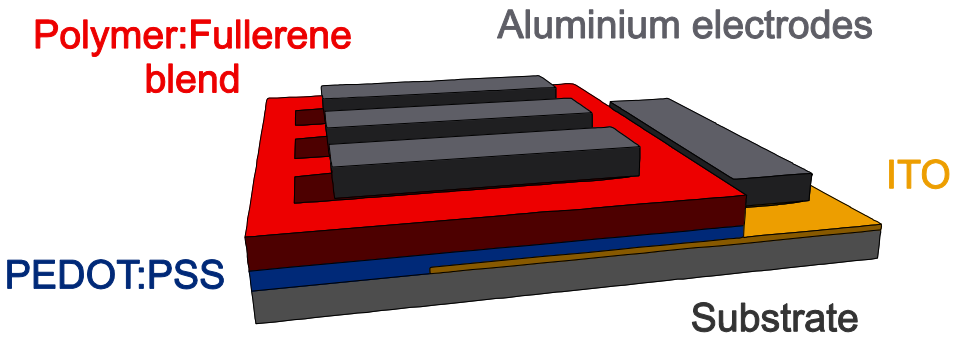

Figure 3.6 Sketch of the solar cell geometry. A PEDOT:PSS layer is spin-coated on an ITO patterned glass substrate. The polymer:fullerene blend is spin-coated on top of the annealed PEDOT:PSS layer. In the last step, aluminium electrodes are evaporated.

The setup for thermal evaporation of the electrodes was integrated in a nitrogen glove box (*MBraun 20G*) and consisted of a vacuum bell (*Leybold Glocke 300*), a turbo-pump to evacuate the bell (*Leybold Turbotronik NT 20*) and a power supply (*Leybold AS 053*). The samples were placed in a sample holder and covered with a mask featuring the pattern of the electrodes. A tungsten boat was mounted between two electrodes inside the bell and filled with the evaporation material. In the case of aluminium several small tungsten pieces were added to prevent a current overshoot when the aluminium starts to melt. The sample holder was placed in the bell and a vacuum of at least $5x10^{-6}$ mbar was generated. The current on the power supply was increased until the material starts to melt and a constant evaporation rate was reached. To deposit the material on the samples, a shutter above the tungsten boat was opened. The thickness of the deposited layer was monitored with an oscillating crystal microbalance. Once the desired thickness was reached, the shutter was closed. The current was reduced to zero and the pressure in the bell was increased to atmospheric pressure.

3.3 Experimental setups

3.3.1 Steady state spectroscopy

3.3.1.1 Absorption spectroscopy

The energies of optical transitions from the ground level (Paragraph 2.5) can be determined by measuring the loss in light transmission through a diluted solution or thin film samples. Such spectroscopic absorption measurements were performed with a *Varian Cary 5000* UV-NIR spectrometer in the range from 200 nm to 3300 nm. The basic principle of the setup is detailed in (Figure 3.7).

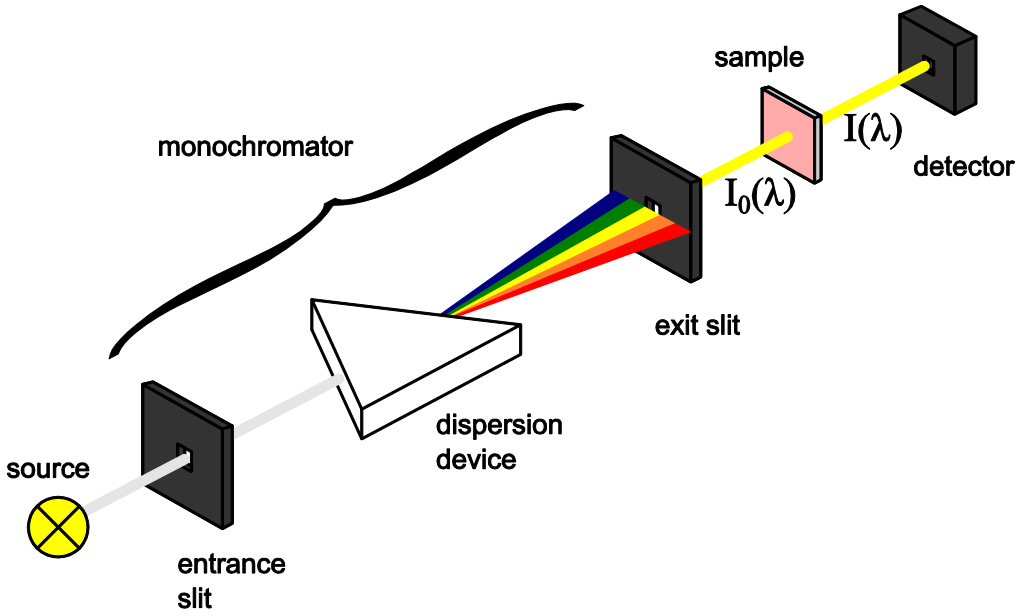

Figure 3.7 Schematic principle of absorption spectroscopy. Monochromatic light is generated by a dispersive element and passed through the sample. The change in transmission, induced by the sample, is measured wavelength dependent with a photodetector.

A strong light source creates white light with a broad spectral distribution from which a selected wavelength is isolated with a monochromator. The monochromatic light is passed through the sample and the intensity in front and behind the sample is measured with a photodiode detector. The wavelength dependent absorbance A(λ) is defined as

$$A(\lambda) = -\log_{10}\left(\frac{I(\lambda)}{I_0(\lambda)}\right), \qquad (3\text{-}1)$$

where $I_0(\lambda)$ is the light intensity in front, and $I(\lambda)$ behind the sample. Under the assumption that scattering can be neglected for clear films, the absorbance is a measure for the number of photons absorbed in the sample.

Experimentally, the monochromatic beam was split into two beams with a beam splitter in the spectrometer. One beam was passed through the sample and gives a measure for $I(\lambda)$, while the other one was used as a reference and gives $I_0(\lambda)$. The correction for substrate induced changes in the transmission spectrum, e.g. reflection or absorption, was performed by measuring a blank substrate to obtain a baseline. This correction was then automatically subtracted from the sample spectrum in the instrument software.

3.3.1.2 Photoluminescence spectroscopy

In photoluminescence spectroscopy optical transitions are induced by an external monochromatic light source tuned to the absorption region of the sample (Figure 3.8). The emitted light from the excitations is passed through a dispersive element and the intensity is measured with a detector.

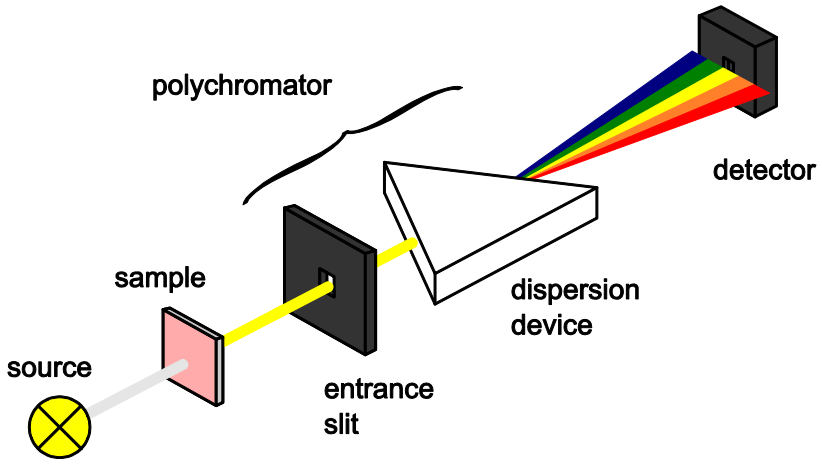

Figure 3.8 Schematic principle of photoluminescence spectroscopy. The sample is excited by monochromatic light and the emitted light is detected spectrally resolved with a photodetector.

Steady state photoluminescence measurements were performed with a *Fluorolog 3 (Horiba Jobin Yvon)* spectrometer. For measurements between 300 nm and 1000 nm a visible double monochromator and a water-cooled photomultiplier tube were used, while for NIR measurements up to 1600 nm an *iHR320* turret monochromator and a thermo-electrically cooled detector *H10330-75 (Hamamatsu)* were employed. High sensitivity measurements were achieved by monitoring fluctuations in the lamp intensity

with a reference photodiode. All measurements were corrected for the quantum efficiency of the detectors.

3.3.1.3 Steady-state photo-induced absorption (PIA) spectroscopy

Steady-state PIA is employed to detect the population of photo-induced states in thin organic semiconductor films or solutions. The schematic setup of this experiment is shown in Figure 3.9.

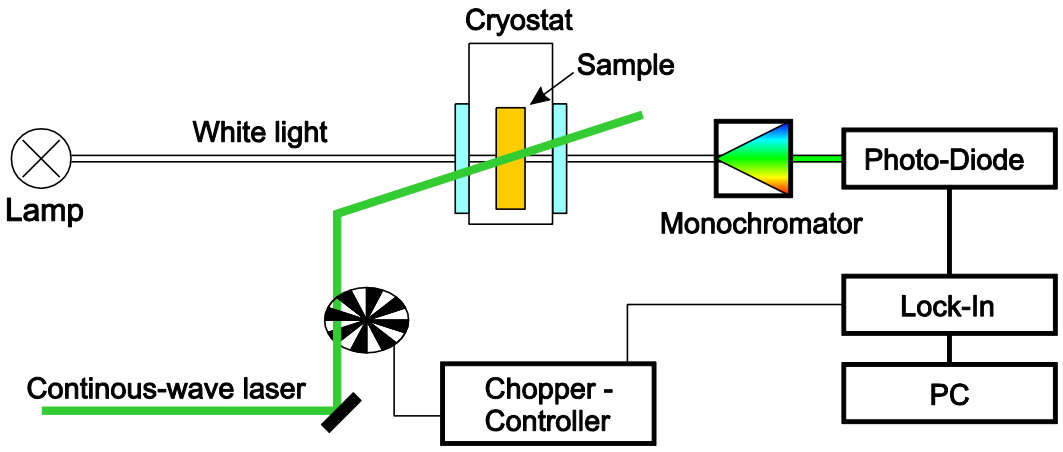

Figure 3.9 Schematic representation of steady-state PIA experiments used to study photo-induced states in organic semiconductor films. The transmission through the sample of a steady state white light (WL) source (e.g. a halogen lamp) is detected with and without excitation by a continuous-wave (cw) laser. The change in transmission is a measure for the photo-induced states. Spectral resolution is obtained by dispersing the WL in a monochromator before detection.

A continuous-wave (cw) laser is used to photo-induce states in the sample, e.g. polarons or triplets. The transmission of a steady-state white light (WL) source through the sample is detected with and without laser excitation. The photo-induced states will lead to additional absorption, hence, reduce the transmission. The relative change in transmission *T* of the probe WL with/without pump laser is proportional to the density of photo-induced states *n*:

$$\frac{T_{Laser\ on} - T_{Laser\ off}}{T_{Laser\ off}} = \frac{\Delta T}{T} \propto \alpha \cdot n \cdot d \qquad (3\text{-}2)$$

In this equation, *d* stands for the film thickness and α is the absorption coefficient of the investigated states at the probe wavelength. The WL is dispersed by a monochromator

and afterwards detected with a photodiode. The steady-state pump laser is modulated with a chopper at a low frequency (<250 Hz). Therefore, also the laser-induced change in transmission ΔT is modulated with this frequency. The value for ΔT is directly obtained by analysing the signal of the photodiode with a Lock-In set to the modulation frequency. The transmission T is determined by measuring the white light spectrum in a second experiment without laser excitation.

3.3.2 Time resolved spectroscopy

3.3.2.1 Femtosecond laser systems

The core of the laser system is the regenerative amplifier system (*RegA 9000, Coherent*) used to amplify laser pulses from a mode-locked Titanium:sapphire oscillator (*Vitesse 2W, Coherent*). A compressor unit behind the RegA 9000 generates ~70 fs laser pulses at around 800 nm wavelength. These pulses are used in optical parametric amplifiers to generate ultra-short laser pulses in the visible to mid infrared energy region. Figure 3.10 gives an overview of the general outlay of the system.

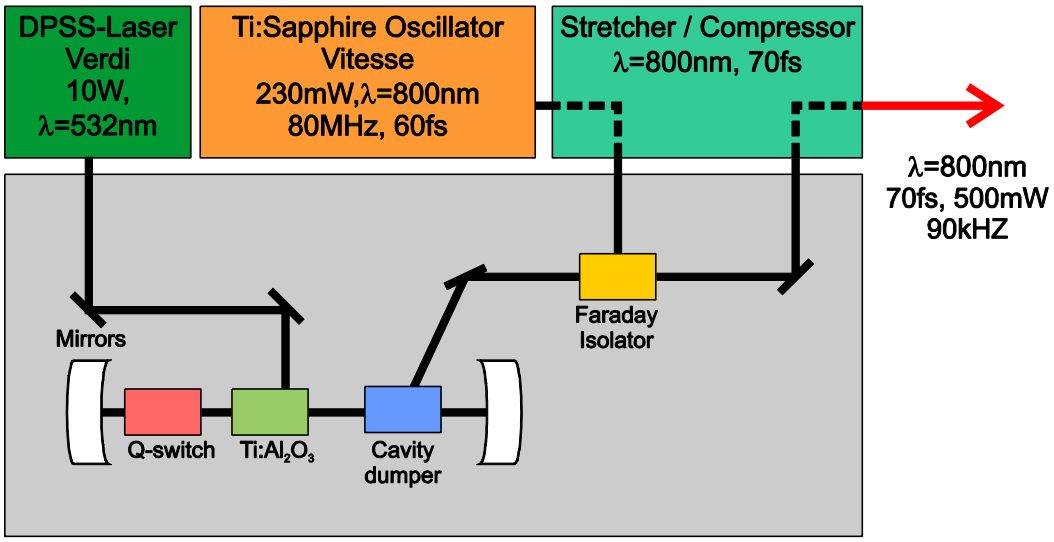

Figure 3.10 Schematic overview of the regenerative amplifier system used to generate femtosecond laser pulses. Femtosecond pulses from a Ti:Sapphire oscillator source are amplified in a Coherent RegA 9000 pumped by a Coherent Verdi cw-laser.

The Vitesse laser system is pumped by a solid state steady-state Nd-YVO_4 laser (*Verdi 2W, Coherent*) at 532 nm and generates sub-100 femtosecond laser pulses at 800 nm centre wavelength with a repetition rate of 80 MHz and 5 nJ pulse energy, using Kerr-

Lens mode-locking. The negative dispersion mirrors in the cavity provide the dispersion compensation needed to produce sub-100 femtosecond pulses.

The pulses from the Vitesse are temporally stretched with a multi-pass holographic grating before entering the RegA 9000. This allows for efficient amplification of the pulses, since during the longer pulse duration more power can be injected from the pump laser (*Verdi V-10, Coherent*). Additionally, lower peak fluences occur in the RegA 9000 preventing damage to optical components. A Q-switch keeps the resonator just below lasing threshold, leading to a build-up of energy stored in the titanium:sapphire crystal. One pulse from the Vitesse seed laser is fed into the resonator through a Faraday isolator using an acousto-optic cavity dumper. At the set repetition rate of 90 kHz every 888th pulse from the Vitesse gets coupled in. The Q-switch is turned off and the strong occupation inversion amplifies the individual pulses during 20 to 30 roundtrips in the cavity. The amplified pulses are out-coupled using the cavity dumper. They pass through the Faraday-isolator and are separated from the seed-pulses with polarization filters. Afterwards, they are compressed down to about 70 fs pulse duration in the compressor unit. Pulse lengths after amplification were checked with a real-time autocorrelator (*Pulse Scope, APE*). In summary, the RegA system generates ~70 fs pulses with a centre wavelength of 800 nm and average power of 6 µJ per pulse at a repetition rate of 90 kHz.

3.3.2.2 Optical parametric amplifier (OPA)

The femtosecond laser system gives pulses with ~70 fs pulse duration and a wavelength around 800 nm. In order to tune the energy of the pulses according to the absorption spectrum of the investigated materials in the visible energy range, an optical parametric amplifier (OPA) from Coherent (*OPA 9400*) was used. Figure 3.11 shows the general outlay of the setup.

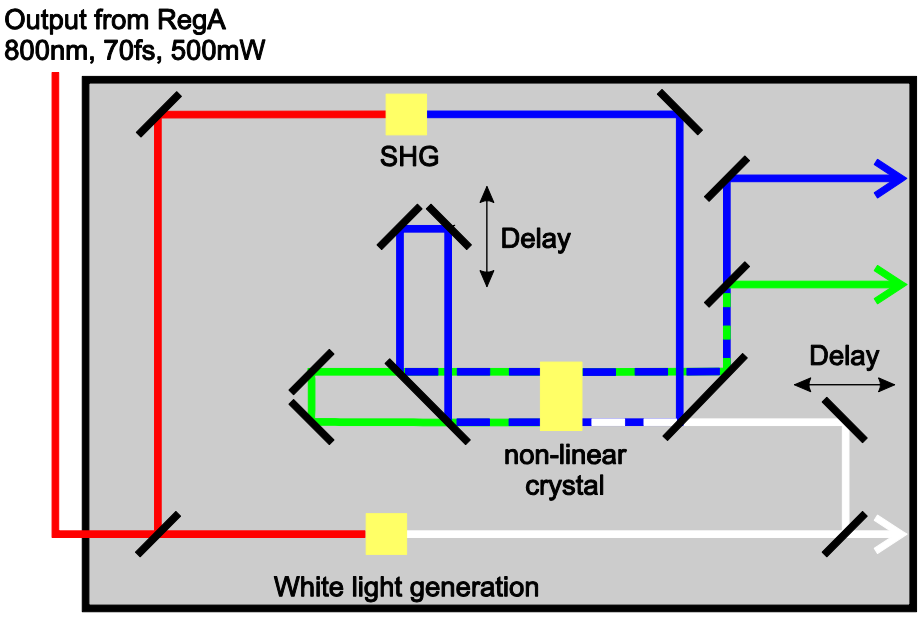

Figure 3.11 Schematic overview of the Coherent OPA 9400 optical parametric amplifier used for tuning the energy of femtosecond laser pulses in the visible range. White light seed and 400 nm pump pules from second harmonic generation (SHG) are superimposed on a non-linear crystal. A narrow part of the white light spectrum gets amplified by hitting the crystal under the corresponding phase matching angle.

The 800 nm RegA output is split into two parts, with 75 % of the signal send to a BBO crystal for second harmonic generation to produce 400 nm pulses (SHG). The remaining 25 % are focused into a sapphire crystal which produces a white light continuum from 450 nm to 1500 nm due to self-phase modulation. A small part of the WL is outcoupled from the OPA through a semi-transparent mirror. The remaining WL passes through a first delay stage, so that the optical path lengths of WL and SHG match when arriving at the non-linear OPA crystal (BBO material) for parametric amplification. Mirrors are used to collimate the SHG and WL beam and superimpose them on the OPA crystal. After the first pass, the SHG and amplified WL component are split and the SHG is send through a second optical delay stage. Afterwards, the beams pass through the OPA crystal for a second amplification. After the second pass the signal, idler and the remnant pump beam exit the OPA. The signal wavelength can be tuned from 500 nm to 700 nm, while the idler wavelengths are between 940 nm and 2400 nm.

3.3.2.3 Non-linear optical parametric amplifier (NOPA)

Measurements of the polaron intraband absorption in the mid-infrared avoid interfering signals from superimposed triplet absorption in the near-infrared. We therefore aim to

probe the polaron signal with ultra-short laser pulses in this spectral region. A two stage non-collinear optical parametric amplifier (*NOPA Ultimate*, *MRX Clark*) is used to generate laser pulses in the near-IR range from 950 nm to 1580 nm (signal) and the mid-IR from 1620 nm to 4800 nm (idler). Figure 3.12 gives an overview on the NOPA geometry.

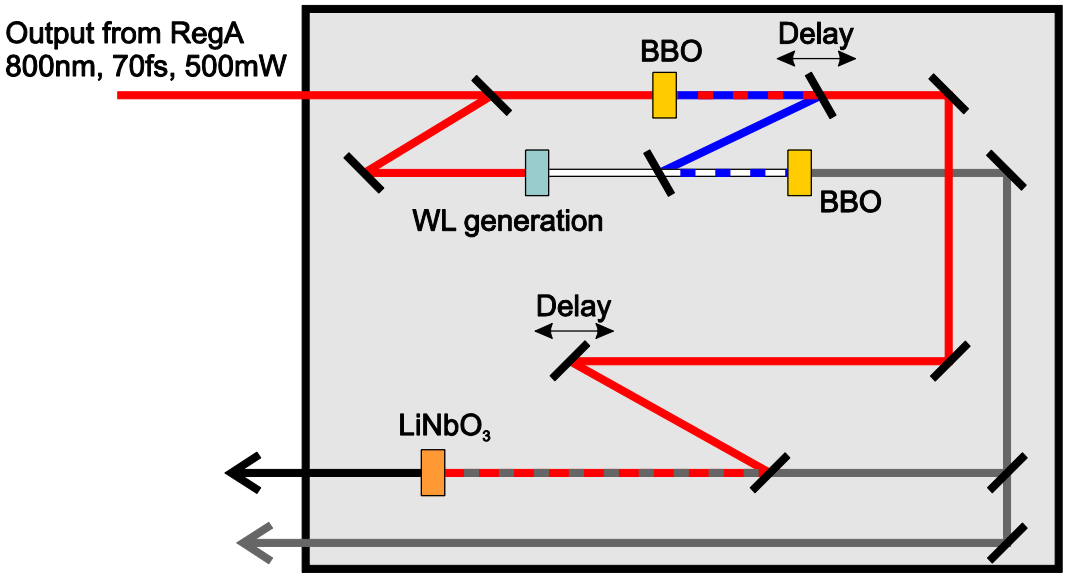

Figure 3.12 Schematic overview of the non-collinear optical parametric amplifier used for tuning the energy of the femtosecond laser in the infrared spectral region. Wavelength selective amplification is achieved by two consecutive amplification stages consisting of non-linear crystals (BBO, $LiNbO_3$). Near-IR pulses generated from white light amplification in the first stage seed the second stage. The first stage is pumped by 400 nm laser pulses while the second stage uses an 800 nm pump.

The output from a RegA 9000 laser system is coupled into the NOPA. One part of the signal is doubled in frequency to 400 nm with second harmonic generation (SHG). With the other part, a white light (WL) super-continuum is generated by self-phase modulation. WL in the visible range is created with a sapphire plate, while for the infrared range an yttrium aluminium garnet (YAG) plate is placed. On the first OPA crystal (BBO) the SHG signal and the WL are superimposed. To reach pulse energies in the mid-infrared around 3000 nm, the first stage has to be tuned to wavelengths in the near-infrared around 1100 nm. Due to the chirped nature of the WL continuum the amplification wavelength can be tuned by changing the temporal delay between SHG and WL pulses. The phase matching angle is adjusted accordingly by tilting the OPA crystal. In the second stage, NIR pulses from the first stage are superimposed with the

800 nm pulses from the RegA 9000 on a $LiNbO_3$ crystal to generate parametric amplification. The idler of the second stage gives ultra-short mid-IR pulses according to formula **(**3-3**)**.

$$\frac{1}{\lambda_{\mathrm{Pump}}} = \frac{1}{\lambda_{\mathrm{Signal}}} + \frac{1}{\lambda_{\mathrm{Idler}}}$$

$$\lambda_{\mathrm{Signal}} = \frac{\lambda_{\mathrm{Idler}} \cdot \lambda_{\mathrm{Pump}}}{\lambda_{\mathrm{Idler}} - \lambda_{\mathrm{Pump}}} \qquad \textbf{(}3\text{-}3\textbf{)}$$

3.3.2.4 Time resolved photoluminescence

For time resolved photoluminescence experiments a femtosecond laser system was used to excite the sample with ultra-short laser pulses (~100 fs). The emission from the sample was spectrally dissolved in a spectrograph and hit the entrance slit of the streak camera. A streak camera (*Hamamatsu C5680, synchroscan unit M5675*) with a measurement range up to 2.2 ns and a maximum resolution of 5 ps was used. The streak tube *N5716-03* was used for measurements in the spectral range from 400 nm up to 900 nm. For measurements in the IR above 900 nm one had to change to a streak camera with tube *N5716-02*. Figure 3.13 shows the basic operating principle of a streak camera. In a first step the photons are multiplied with a photomultiplier and converted into electrons at the photocathode. The time resolution is achieved by sending these electrons through two deflecting electrodes in parallel capacitor configuration. A linear increasing voltage sweep is applied between the plates, initialized by a trigger synchronized to the laser pulse. The first electrons arriving at the capacitor experience only a low voltage and are therefore barely deflected. Electrons arriving later are exposed to a higher voltage and accordingly experience a stronger deflection. This leads to a vertical spread of the electrons. Before reaching the CCD camera, the electrons are amplified in a micro-channel plate and re-converted into photons on a phosphor screen.

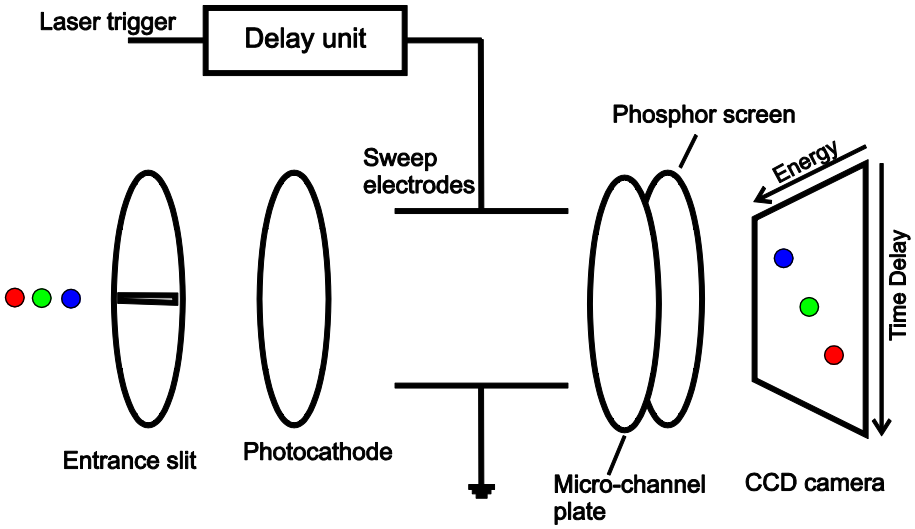

Figure 3.13 Schematic geometry and working principle of a streak camera. Photons excited in a sample with an ultra-short laser pulse are passed through a deflection unit which allows temporally resolved detection.

An exemplary picture on the CCD camera is shown in (Figure 3.14). On the x-axis the signal is spectrally resolved, where temporal resolution is given on the y-axis. The colour coding represents high (red) and low (black) intensities.

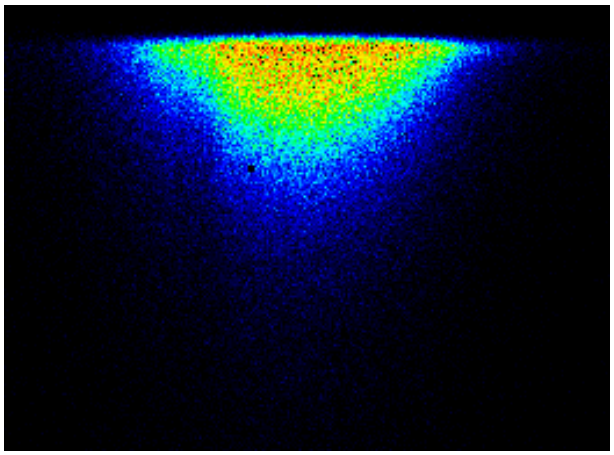

Figure 3.14 Example of a streak camera measurement. Emission from a PCPDTBT thin film excited at 400 nm; emission centre at 835 nm; full vertical dimension of the picture corresponds to 300 ps time range.

3.3.2.5 Pump-probe technique

With the pump-probe technique photo-induced proceses are investigated on an ultra-fast time scale. A femtosecond (fs) “pump” laser pulse excites the sample and creates new

states, e.g. triplets or polarons. A second “probe” laser pulse arrives time delayed with respect to the pump pulse and is absorbed by the photo-induced states, i.e. the states created by the pump pulse. The ratio of transmission $\Delta T/T$ of the probe pulse with/without pump pulse is proportional to the density of photo-induced states n (Equation **(**3-2**)**). In the present setup the pump pulses were either the signal from an OPA in the range 500-700 nm or the frequency doubled direct output (400 nm) from the RegA. As probe pulses, either the while light continuum generated in the OPA (500-1500 nm) or the output of the NOPA (1100 nm – 5000 nm) was used. All laser pulses had the frequency of the amplifier system (90 kHz).

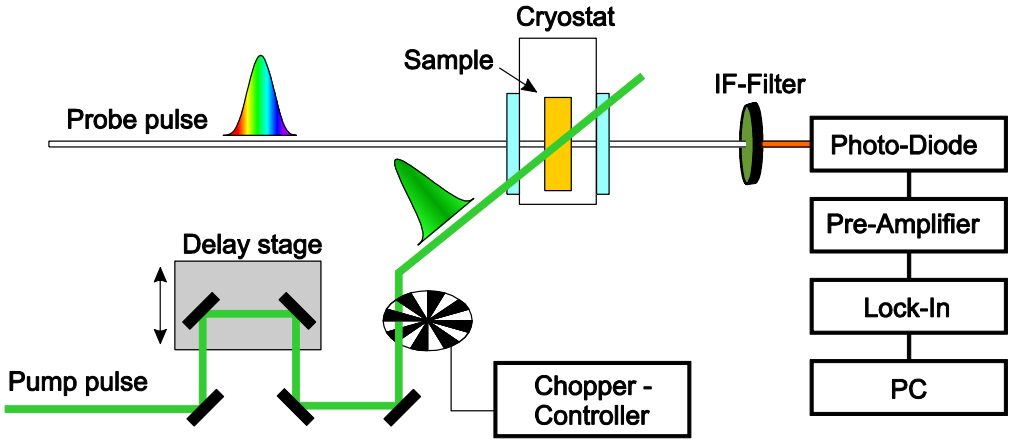

Figure 3.15 Schematic representation of the pump-probe setup used to study photo-induced states in organic semiconductor films. The difference in transmission of a probe pulse through the sample is detected with and without pump pulse. Temporal resolution is achieved by changing the time delay between pump and probe pulses with a delay stage.

For measurements in the mid-IR, using the idler of the NOPA as probe, a germanium plate was placed in front of sample and detector to block photons with undesired energies, i.e. the signal pulses from the NOPA. On the other hand, using the WL pulses from the OPA as probe, interference filters (*Melles Griot CVI*) with the respective energy pass were placed in front of the photodiode to detect at the desired energy.

For probe energies above 1.24 eV a high speed silicon photodiode (*Thorlabs DET 210*) was used. For energies between 1.24 eV and 0.73 eV a high-speed InGaAs detector (*Thorlabs, DET 410*) and for the measurements with mid-IR pulses around 0.4 eV a nitrogen cooled MCT detector (*Infrared Associates, MCT-5-N-2.0*) were employed.

The on/off frequency of the pump pulse was modulated with a mechanical chopper at 6 kHz, which leads to an averaging of 15 probe pulses during one on/off phase. To increase the signal to noise ratio, the signal from the photo-diodes was measured with lock-in detection. Before entering the Lock-Ins (*Stanford Research SR830*), a pre-amplifier (*Stanford Research, SR560*) enhanced the signal. A first lock-in was set to 90 kHz, which is the repetition rate of the probe beam. With this Lock-In the unmodulated transmission through the sample was detected. The output of the first Lock-In was then fed into a second Lock-In, which was set to 6 kHz, i.e. the modulation frequency of the pump beam. Hence, the output of the second Lock-In provides the change in transmission induced by the pump pulse. The ratio of the signals measured at the second (change in transmission) and the first (transmission) Lock-In gives the relative change in transmission $\Delta T/T$, which is a measure for the number of photo-induced states as shown in Equation **(**3-3**)**. The samples were placed in a homebuilt cryostat with CaF_2 windows and evacuated with a turbo pump (*Pfeiffer Vacuum, TSH 071 E*) to pressures below 10^{-5} mbar to keep them under inert conditions. Temporal resolution is achieved by delaying the pump pulse with respect to the probe pulse, using a translation stage (*Aerotech ATS100*). The maximal delay between pump and probe is limited to 1 ns by the length of the stage (0.3 m). For all measurements, any beam walk due to inaccurate coupling to the translation stage was avoided by monitoring the beam on a beam profiler (*Data Ray Inc., WinCamD*). The beam profiler was also used to check the beam diameters in order to keep the probe beam much smaller than the pump. This assures homogeneous excitation over the whole probe beam area. Beam fluences were kept as low as possible (<5 µJ/cm²) to avoid any non-linear effects and to be as close to solar cell operation conditions as possible.

3.3.3 Film morphology characterization

3.3.3.1 Scanning electron microscopy (SEM)

In scanning electron microscopy (SEM) an electron beam is used to investigate the surface morphology and properties of samples. We used a *Zeiss Ultra Plus* at 750 V acceleration voltage. The SE2 detector mainly detects secondary electrons, which give insights about the topography of the sample surface. On the other hand, the In-Lens detector detects secondary electrons, but uses a charged pole piece to suck electrons leaving the sample to the detector. This gives the In-Lens detector a higher sensitivity to

variations in the electronic and material properties of the sample. The working distance was kept at 3.5 mm to ensure high collection efficiencies of secondary electrons aided by the electrostatic lens and allowing efficient detection of SE2 electrons at the same time. For details of SEM measurements the reader is referred to the seminal literature [168,169].

3.3.3.2 Transmission electron microscopy (TEM)

In transmission electron microscopy (TEM) the transmission of a focussed electron beam through a sample is measured. Images were taken with a *JEOL transmission electron microscope* operated at 80 kV. The use of an electron beam as imaging tool allows for very high spatial resolution. It is possible to measure small differences in electron transmission as required to map the composition of organic semiconductor blends, where the constituting materials differ only slightly in chemical composition. In order to apply this technique the thin organic semiconductor film was transferred on a carbon grid as support. For this, the film has been spin-coated onto a PEDOT:PSS coated substrate. By gently sliding the substrate into a water filled beaker, the water-soluble PEDOT:PSS is dissolved and the film floats on the water surface. From there it was picked up with the carbon grid.

3.3.3.3 Atomic force microscopy (AFM)

For mapping the topography of samples an atomic force microscope (*Veeco, Innova scanning probe microscope*) was used. Due to the soft nature of organic semiconductors, measurements were taken in tapping mode to avoid modifications of the surface during acquisition. A cantilever was set into periodic vertical oscillations and approached to the film surface, while the oscillation was monitored by the deflection of a laser beam from the cantilever. The forces from the sample acting on the cantilever, e.g. Van der Waals or electrostatic interactions, change the amplitude of the oscillation. By moving the cantilever up and down to maintain the initial amplitude of oscillation, a height profile of the sample surface was obtained.

3.3.3.4 Confocal laser scanning microscopy

For mapping of the photoluminescence from thin film samples, a laser scanning confocal microscope was used. In order to obtain the best possible resolution, immersion oil was used. Resolutions around 300 nm have been achieved. A laser beam

from a continuous wave laser (*Laser Quantum Opus with stabilized MCP6000 power supply*) with a wavelength of 532 nm was coupled into a standard confocal microscope (*Olympus IX81 FVSF-2*). A 100x objective (*UPLANFL N 100x*) focussed the laser on the sample surface, which was translated in three dimensions. The emitted photoluminescence from the sample was collected through the excitation optics and detected with a photodiode. A long-pass colour filter was used to block the excitation beam. Spatial resolution in the sample plane was achieved with a deflection unit consisting of two mirrors placed at 90 degrees to each other. By moving the mirrors a two dimensional area of the sample was scanned with the focussed laser beam. By correlating the position of the laser beam with the detected photoluminescence intensity a 2D map of the photoluminescence was obtained.

4 Low-voltage Scanning Electron Microscopy Imaging of Doped Organic Semiconductors Films

In this chapter, a simple and fast method to unravel dopant distributions in thin films of conjugated polymers (PCPDTBT, P3HT) is presented. In addition, by performing a systematic study as a function of dopant concentration, the role of dopant molecules on polymer film nanomorphology is investigated. First, we study changes in film topography of organic semiconductor polymers in the pristine form and in the presence of the dopant F_4TCNQ by atomic force microscopy (AFM). Further, low-voltage scanning electron microscopy (SEM) is employed to monitor the surface morphology and material composition of doped films. Regions with increased contrast are detected in doped films. Photoluminescence (PL) mapping in the plane of the film is used to assign these distributions to dopant rich and dopant deficient domains. Our experiments show that dopant distributions can be detected as a difference in SEM contrast, originating from site-sensitive surface charging by the electron beam. In summary, we demonstrate low-voltage SEM as a convenient tool to monitor F_4TCNQ distributions and clustering thresholds in different conjugated polymers.

4.1 Motivation for dopant distribution mapping in polymeric organic semiconductors

A prerequisite for the success of organic electronics in the current information-technology market is performance and reliability. Recent scientific efforts towards this milestone consider the use of dopant molecules to improve the transport characteristics of light emitting diodes and solar cells [170–173]. Doping has been demonstrated to be critical in tuning the injection properties at metal-semiconductor interfaces, leading to full control over device parameters [174–176]. Spatial control of the dopant molecules' position has the potential to improve charge injection by placing dopants near the contacts [175,177]. Positioning of dopants in transport layers improves carrier drift/diffusion [178] and also charge separation at heterojunctions [179]. While in devices based on small molecules spatial control can be easily achieved by sequential evaporation of layers to form stacked devices [170], this aspect remains challenging for solution processable conjugated polymers. However, also for these materials there is substantial interest in achieving control of electronic processes by doping [11,180]. Recently, the physical origin of the doping mechanism has seen a renewed interest, partially because of the demonstration of single-dopant molecule imaging by scanning tunnelling microscopy (STM) [12] and the description of hybrid states at the dopant/semiconductor interface [181,182]. Systematic studies, as a function of the dopant/semiconductor weight ratio, report changes in electrical characteristics, often showing a saturation in mobility and conductivity as the ratio is increased over a certain threshold [11,183].

A critical aspect is the *dopant distribution* within the semiconductor and the effect of dopant molecules on the organic semiconductor *morphology*. The latter issue is expected to be highly relevant, considering the widely reported and discussed effects of meso-morphology on the optoelectronic characteristics of organic semiconductors [184]. On the other hand, the nature of the intermolecular interactions influences the dopant distribution on the nanoscale. In this respect, the experiments of Kahn and co-workers by STM [12] are extremely valuable. In these experiments, single dopant molecules were placed in highly ordered organic semiconductor molecule films of only a few molecular layers. The effect of this placement on the charge distribution around the individual dopant molecules was studied. However, such a method is limited to ultra-thin films exhibiting high crystallinity. Thus, it remains a great challenge for amorphous polymer-

dopant blends to observe dopant distributions on the molecular level. Homogeneous dispersion of dopant molecules in the host material is highly beneficial to maximize the wavefunction overlap for electron or hole donation [185], while clusters might reduce doping efficiencies. A tool to monitor these phenomena in solution processable disordered polymeric semiconductors, where films are often deposited as polymer/dopant blends, is lacking.

We studied the morphology of two exemplary conjugated polymers, PCPDTBT (poly[2,1,3-benzothiadiazole-4,7-diyl[4,4-bis(2-ethylhexyl)-4H-cyclopenta[2,1-b:3,4-b'] dithio-phene-2,6-diyl]]) and P3HT (poly(3-hexylthiophene), doped at different concentrations with the small molecule F_4TCNQ (2,3,5,6-Tetrafluoro-7,7,8,8-tetracyanoquinodimethane). These polymers are known to be benchmark systems for solar cells and field effect transistors, respectively. The materials were obtained from 1-material (PCPDTBT), and Sigma-Aldrich (P3HT, F_4TCNQ). Both polymers had a similar molecular weight of about 20.000 g/mol. Since PCPDTBT and P3HT are well known hole transporting materials they were doped with the strong electron acceptor F_4TCNQ. Addition of the dopant to the polymer films leads to ground state charge transfer and generation of holes in the polymer HOMO (see Paragraph 5.3 for a detailed discussion). In the following, we present SEM imaging as a method to correlate differences in image contrast to dopant rich and dopant deficient regions. This technique allows us to study the effects of dopant molecules on film morphology and find the critical concentrations for dopant clustering or self-segregation.

4.2 Morphological investigation of doped conjugated polymer films with AFM and SEM

In this paragraph we study the surface morphology of doped conjugated polymer films with AFM and SEM. Films with different levels of doping up to 10% were investigated. We chose the low-bandgap polymer PCPDTBT and the well-known polymer P3HT as exemplary compounds. The dopant F_4TCNQ was added to the polymer in solution. All doping ratios are given per weight of the polymer.

First, AFM is used to study the film topography. Figure 4.1(a-d) show AFM images of PCPDTBT films doped at different weight ratios with F_4TCNQ. The topography of the undoped films is reasonably flat with maximum elevations of 12 nm. A fibrous meso-structure is visible in pristine PCPDTBT films (Figure 4.1a). An equally flat topography

with maximum elevations of 8 nm is observed for doped films up to 7.5% doping. However, the fibrous structure, visible in pristine films, is disrupted at 5% and 7.5% dopant concentration (Figure 4.1(b,c)). For the highest dopant concentration (10%, Figure 4.1d), localized elevated topological features are visible. These clusters reach a height of ~40 nm and a diameter of 200 nm. Hence, the introduction of dopant molecules into PCPDTBT films has only a small effect on the topography up to a doping ratio of 7.5% and leads to the formation of clusters for dopant concentrations above 7.5%.

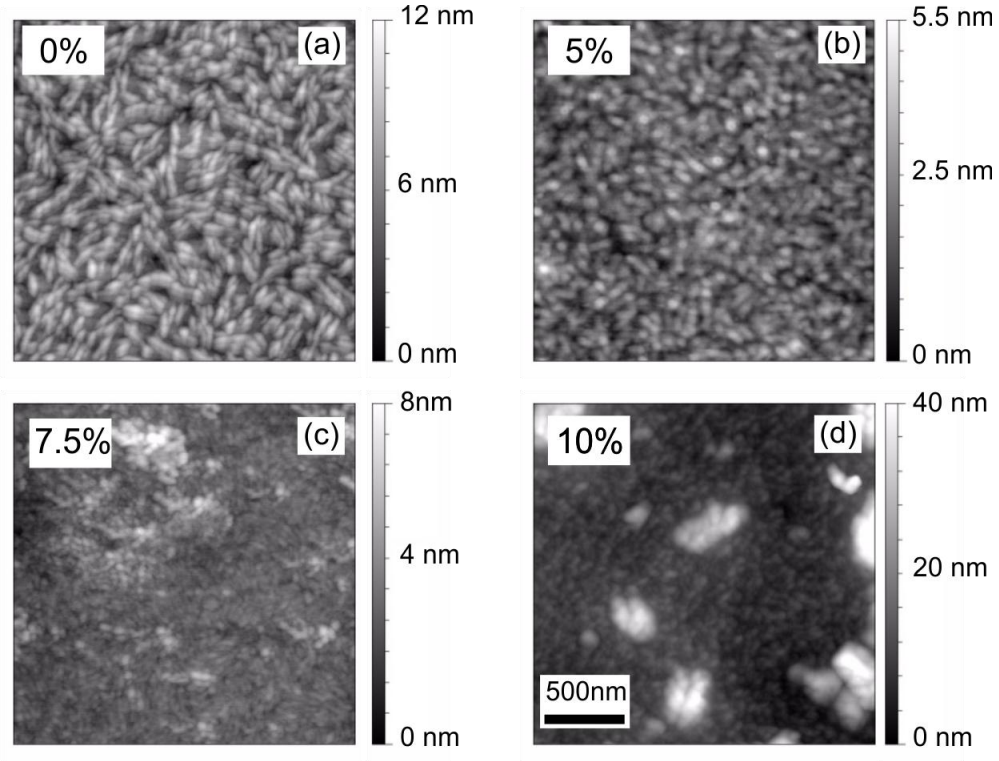

Figure 4.1 AFM topography images of PCPDTBT films doped with F_4TCNQ at (a) 0%, (b) 5%, (c) 7.5% and (d) 10%. The scale bars correlate the colour coding to differences in height. Undoped films show a fibrous surface morphology, which is disrupted for higher doping ratios (b,c). Larger clusters are visible at 10% doping (d).

The corresponding AFM images for P3HT are shown in Figure 4.2. The topography of the undoped film (Figure 4.2a) is very homogeneous, as observed in previous publications [186]. The film is flat with maximum elevations of 10 nm. The typical crystalline and fibrous regions of P3HT films are not observed. We attribute this to the low molecular weight of the investigated P3HT and the omitted post-annealing of the films. However, we note a pronounced change in film topography already from 5%

doping on. For the doped films, the roughness increases and elevations of ~50 nm height are present. The films also show a coarser morphology compared to the undoped films with the formation of larger domains. This effect increases with the formation of clusters at 7.5 and 10%. Thus, the introduction of dopant molecules has a greater effect on P3HT films with respect to PCPDTBT films and leads to the formation of a more disordered film topography. At high doping ratios (10%) the formation of clusters is observed in both polymers.

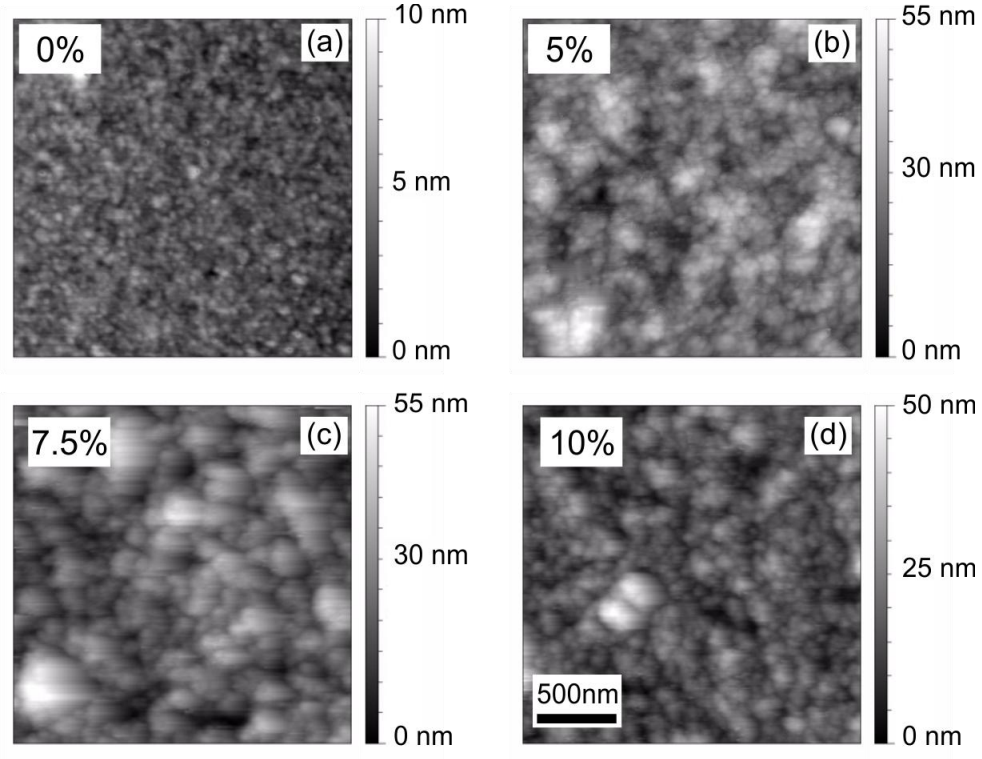

Figure 4.2 AFM topography images of P3HT films doped with F4TCNQ at (a) 0%, (b) 5%, (c) 7.5% and (d) 10%. The scale bars correlate the colour coding to differences in height. Undoped films show a homogenous, flat surface morphology. The film roughness increases for higher doping ratios (b-d).

The AFM experiments give information on changes in film topography due to incorporation of dopant molecules. However, the detailed distribution of dopant molecules in the films cannot be resolved. Additionally, the origin and composition of the aggregates and clusters at higher doping cannot be analysed. For this we need to employ a technique which is sensitive to differences in material properties. Scanning electron microscopy (SEM) uses differences in electron yield to image samples. Since the electron yield depends on the investigated materials' elementary and electronic

properties, SEM can be used to study the material composition of samples. Therefore we use SEM in the following section to investigate the dopant distribution in doped polymer films.

Figure 4.3(a-h) shows low acceleration voltage (0.75 kV) SEM images of PCPDTBT thin films (100±10 nm thickness) doped at different concentrations with F_4TCNQ. The films are deposited on a silicon substrate (without oxide layer) by doctor-blading and loaded in the SEM chamber without any further pre-treatment. The SEM data is shown in two rows: In the top row, the In-lens detector positioned within the electron column of the microscope was used, whereas in the bottom row, images were detected with a detector for secondary electrons (SE2). The SE2 detector renders mainly the surface morphology, while the information provided by the In-lens detector is more sensitive to material properties, such as the elements' atomic number [168].

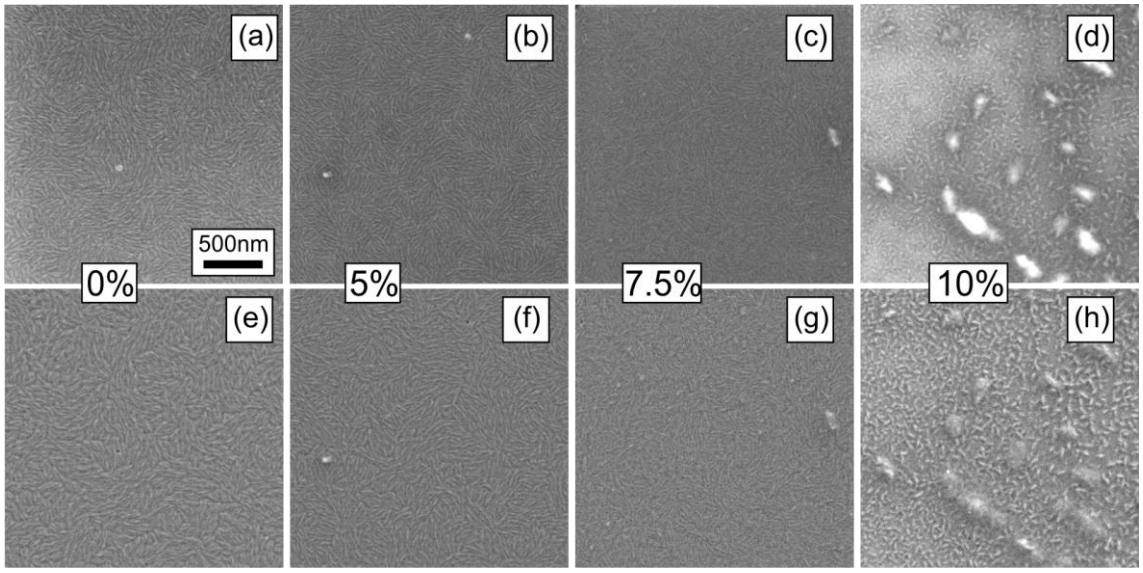

Figure 4.3 Scanning electron microscopy images of PCPDTBT doped at different ratios with F_4TCNQ as stated. Images taken with InLens (a-d) and SE2 (e-h) detectors. Acceleration voltage for all images was 0.75 kV. The undoped films (a,e) show a fibrous morphology which is reduced for higher doping ratios (b-d, f-h). Regions with increased contrast are visible at high doping ratios in the InLens image (d). The scale bar gives the dimensions for all images.

Figure 4.3(a,e) show the pristine polymer film surface morphology, exhibiting a fibrous texture with dimensions on the order of a few tens of nanometres. No further ordering on a larger length scale is observed in Fourier transformations of the images. This observation correlates with the pristine film topography obtained from AFM images

(Figure 4.1a). From previous work, PCPDTBT is known to be a semi-crystalline polymer [187]. Under slow deposition conditions, as chosen here, the polymer chains are expected to order into crystalline domains, detected by the SE2 detector as small fibres. From the much higher length of the fibres with respect to the polymer chain length, it is reasonable to assume that the polymer chains are aligned across the diameter of the fibres and not extended along the whole fibre. Remarkably, the fibrous structure is also visible in the InLens picture. This indicates a difference in electron yield between the fibrous and amorphous regions, not related to topography. Differences in electron yield originate from differences in the electron densities. Therefore, the observation of the fibrous domains in InLens images points to different electron densities in fibrous and amorphous regions. We attribute these differences in electron density to a higher molecular packing in the fibrous regions.

Notably, the pristine surface morphology is disrupted in doped films for doping ratios of 5% and 7.5% (Figure 4.3(b,c,f,g)). The amount of fibres substantially decreases and their size is reduced. At 7.5% doping brighter regions appear which form prominent clusters at 10% doping (Figure 4.3d,h). We note that these clusters agree in size and shape with the structures observed in 10% doped films with AFM (Figure 4.1a). Remarkably, the In-lens image (Figure 4.3d) shows a large contrast between clustered and amorphous regions. This indicates a difference in electron yield between these regions and substantial differences in material composition. It is known, that F_4TCNQ molecules in close vicinity to each other are prone to form crystallite clusters due to their strong intermolecular interactions [10]. As a working hypothesis, we assign the brighter areas therefore to regions with increased dopant density, i.e. giving rise to F_4TCNQ clusters.

Additionally, we investigated doped films of P3HT to compare our results on PCPDTBT with another conjugated polymer. Figure 4.4(a-d) show In-Lens SEM images of P3HT doped at concentrations identical to those used for PCPDTBT. The morphology of the pristine polymer is substantially less structured compared to PCPDTBT, which indicates a lower extent of ordering and less interchain interactions. Accordingly, pristine P3HT films have a more homogeneous morphology compared to PCPDTBT. Further, an increase in image contrast develops already at low doping ratios (5%, 7.5%) and noticeable areas of increased brightness are observed (Figure 4.4(b,c)). As for doped PCPDTBT, we propose that these domains are dopant rich. At 10%

doping, the dopant clusters reach diameters up to 500 nm, as shown in Figure 4.4d. The fact that the image of the 5% doped sample exhibits larger bright areas compared to higher doped films is due to the *relative contrast* of the images. Already during image acquisition, the contrast range of each picture is adjusted to the brightest and darkest region of the image ("auto-contrast"). Accordingly, the absolute brightness of the pictures cannot be directly compared and the presumably larger area of bright regions in the 5% film, with respect to the 10% one, is due to a difference in image contrast scale.

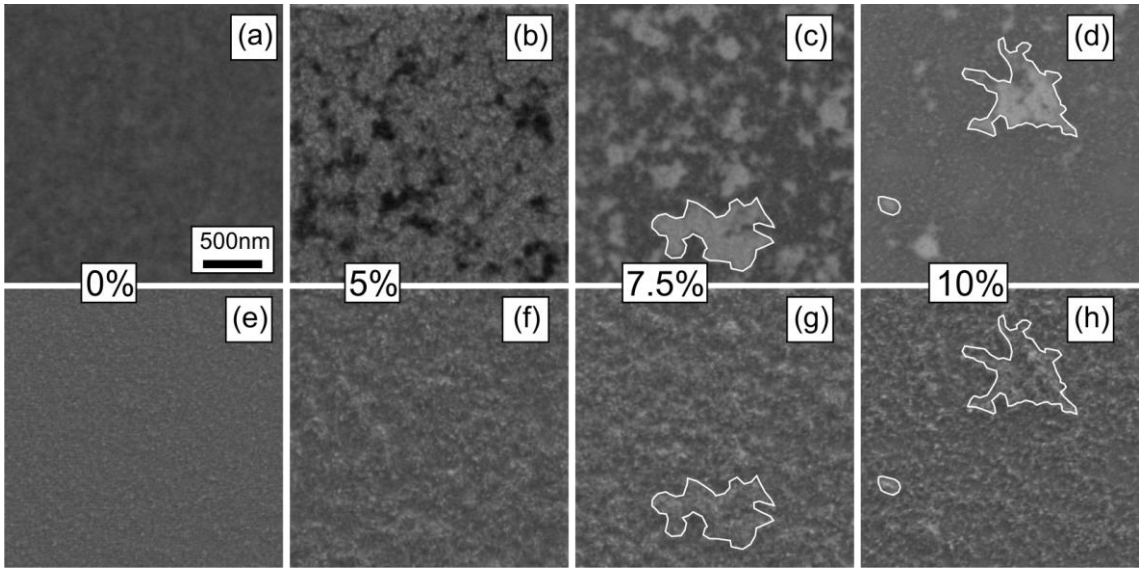

Figure 4.4 Scanning electron microscopy images of P3HT doped at different ratios with F_4TCNQ as stated. Images taken with InLens (a-d) and SE2 (e-h) detectors. Acceleration voltage for all images was 0.75 kV. Undoped films (a,e) show a homogenous morphology. Regions of increased contrast are visible in doped films (b-d) with the contrast increasing with doping. At higher doping ratios (g,h) bright features in InLens pictures relate to features in SE2 topography images (white outlines).The SE2 pictures show a concomitant increase in film roughness. Scale bar gives dimensions for all images.

The lower row in Figure 4.4(e-h) presents images taken with an SE2 detector sensitive to topography. While the undoped film (Figure 4.4a) shows very little surface structure, already at 5% doping there is a noticeable increase in surface roughness. This correlates with the observed increase in height distribution in AFM images (Figure 4.2b). At higher doping ratios it is possible to relate regions with increased height in SE2 images to regions that appear bright in the InLens pictures (marked regions in Figure 4.4(e-h)). This effect is in parallel with the cluster formation in highly doped PCPDTDT films. One could generally expect that a similar increase in SEM image contrast is observed in

any polymer-acceptor system and not just in polymer-dopant blends. However, no comparable increase in SEM contrast is detected in exemplary polymer:fullerene blends (Appendix A).

In conclusion, the introduction of F_4TCNQ dopant molecules into PCPDTBT films affects the pristine polymer morphology only slightly and leads to phase segregation only at high doping ratios (10%). On the other hand, for P3HT films, we observe deviations from the pristine film morphology and phase-segregation already at lower doping ratios (5%). Brighter and darker regions were observed in SEM images of doped polymer films, pointing to differences in material properties between these domains. We proposed that the observed bright regions are dopant rich domains. To assert this assumption, we investigate the films with photoluminescence (PL) mapping in the next paragraph.

4.3 Correlation of emission quenching patterns in PL maps with dopant distributions in SEM images

Another microscopy technique which can give unique insights on the morphology of organic semiconductors is confocal laser scanning microscopy [188–190]. Confocal microscopy is particularly suited to probe dopant distributions in our samples, since dopant molecules induce additional charge carriers in nearby polymers. Therefore, the PL of these polymers is quenched by exciton-polaron interactions [191]. In our experiment, a laser exciting the polymer is scanned over the sample plane and the emitted PL of the polymer is collected point by point, resulting in a 2D PL intensity map. Figure 4.5 shows the PL imaging of PCPDTBT films undoped (a) and at increasing concentrations of F_4TCNQ (b-d). The full pictures show images which have been post-processed after acquisition with an imaging processing software for optimal contrast and intensity, while the insets show the raw data. The post-processing was necessary because of the substantial decrease in PL intensity with increasing doping (Figure 4.5, insets). The PL maps of undoped PCPDTBT films (Figure 4.5a) show a homogenous emission without any patterns. Confocal microscopy has a resolution comparable to the diffraction limit of the excitation light (~300 nm at the excitation wavelength of 532 nm). It is therefore not surprising that the fibres observed in SEM and AFM images for the pristine PCPDTBT sample are not distinguishable. With increasing doping the overall PL intensity in the PCPDTBT images decreases

homogeneously in the whole field of view (Figure 4.5(b-d)). This indicates a homogeneous distribution of dopants in PCPDTBT films with domains much smaller than 50 nm, which cannot be resolved in the confocal laser scanning microscope. Accordingly, the homogeneous quenching in doped PCPDTBT films indicates a homogeneous distribution of dopant molecules in these films.

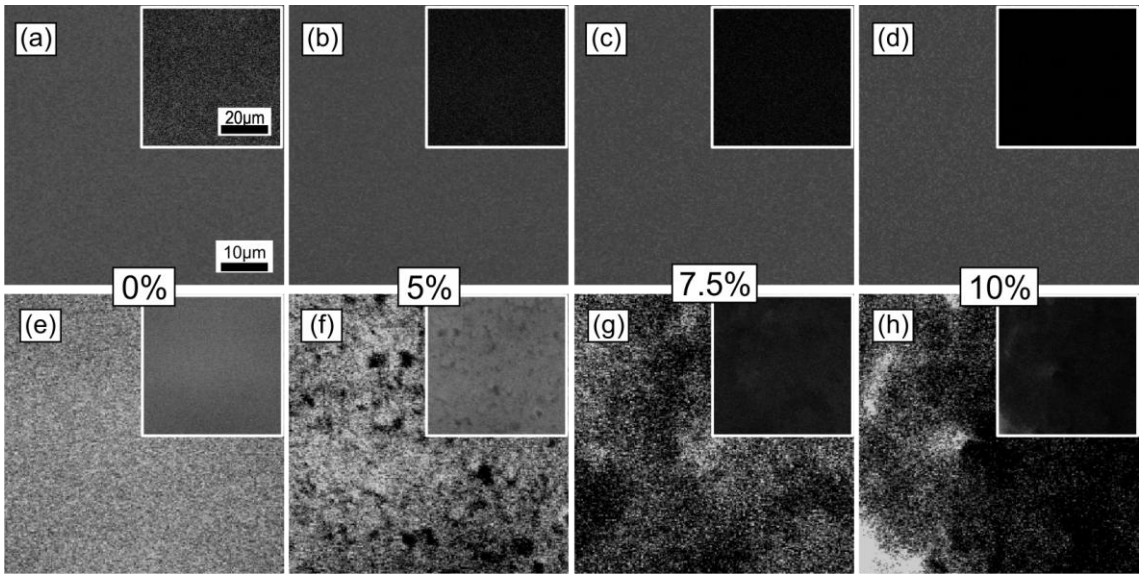

Figure 4.5 Photoluminescence maps for PCPDTBT (a-d) and P3HT (e-h) thin films doped with F_4TCNQ at different ratios as stated. Images were post-processed for optimal contrast, while the insets show the raw data. Excitation wavelength was 532 nm (150 µW). Scale bars give dimensions for all images and insets, respectively.

This observation is corroborated by comparing the PL maps with the SEM images of Figure 4.3. No bright regions with increased contrast were observed in SEM images of doped films up to 7.5% doping, which correlates with the homogeneous quenching in PL maps for these samples. Therefore, our assignment of bright regions in SEM to dopant rich clusters is supported by PL mapping. Interestingly, clusters, observed with SEM for the 10% samples, are not observed with the confocal laser scanning microscope. We attribute this to the almost complete PL quenching for these samples (Figure 4.5d, inset). Hence, distinguishing dopant induced differences in intensity is not possible. Summarizing the results for PCPDTBT, the photo-generated excitons, having a short diffusion length (~20 nm [71]), are quenched with a high probability in the whole film, indicating a *homogeneous* dopant distribution in the film up to 7.5% doping.

For the case of P3HT films, undoped samples give rise to homogeneous emission without any patterns (Figure 4.5e). On the other hand, doped P3HT films

(Figure 4.5(e-h)) show modulations in PL intensity already from 5% doping on. The non-emissive, dark areas increase in size with increasing doping, up to a length scale of one micron at 10% doping. PL quenching mainly occurs in dopant rich regions, as such, we can assign darker areas to areas with a high dopant load. Large areas that appear brighter in Figure 4.6(g,h) are subjected to less exciton-polaron quenching. This leads to the conclusion, that for P3HT the dopant molecules tend to cluster and not homogeneously intermix with the polymer molecules from 5% doping on. Shape and size of the dark areas, i.e. areas of high quenching, are similar to the bright areas detected in SEM images. This further supports our interpretation of the bright regions in SEM images to be dopant rich.

It has been shown in previous publications [10,192], that due to the small dielectric constant of these materials the electrostatic interaction between the ionized dopant and the polymer molecules can be substantial. This may create local electric fields which perturb the assembly of pristine polymer chains. Meanwhile, F_4TCNQ molecules have the tendency to aggregate into crystallites. In our experiments, the minimum amount of dopant that can be introduced in polymer film without altering the film morphology in an appreciable way is higher for PCPDTBT (up to 10%) than for P3HT (below 5%). One possible explanation is the donor-acceptor structure of PCPDTBT which provides intrinsic on-chain dipoles [193,194], capable of screening the interaction between the ionized dopants.

In conclusion, photoluminescence mapping of doped polymer films confirms our assignment of bright regions in SEM images to dopant rich domains. We present low-voltage SEM as a new technique to study the in-plane distribution of dopant molecules in polymeric organic semiconductor thin films with high resolution. The dopant distribution in two seminal polymers, PCPDTBT and P3HT, was investigated. Doped P3HT films tend to phase segregate already at 5% and the dopant rich regions reach diameters up to one micron for 10% doping. On the other hand, films of PCPDTBT show a homogeneous distribution of dopant molecules up to 7.5% doping. So far, our results answered the question how dopant distributions can be mapped in amorphous organic semiconductor films. However, the physical origin of the increased contrast between dopant and polymer rich domains in SEM images is not yet clear. This question will be addressed in the next two paragraphs.

4.4 Monte-Carlo simulation of SEM electron yield from doped polymer films

Until now, we have not addressed the physical origin of the increased contrast in SEM images of doped films taken with the InLens detector (Figure 4.3, Figure 4.4). The observed effect might originate from differences in the materials' elementary composition or differences in the electron density. Monte-Carlo simulations were performed with the *Casino 2.0* software to address this question. With the simulation software the electron yield for a given electron energy and material, as well as the electron yield from different depths within the sample are simulated. A difference in atomic number between the investigated materials would lead to differences in the electron yield, since the electron scattering process involves the interaction between the accelerated electrons and the investigated elements' atoms [168,169]. The electron yield depends accordingly on the mean atomic number of the materials. Figure 4.6 shows the electron yield distribution as a function of the detected electron energy for the investigated materials. A film thickness of 100 nm was used in the simulations. The low-energy secondary electrons are shown as one featureless peak, since the simulation software is not able to resolve their detailed energy distribution.

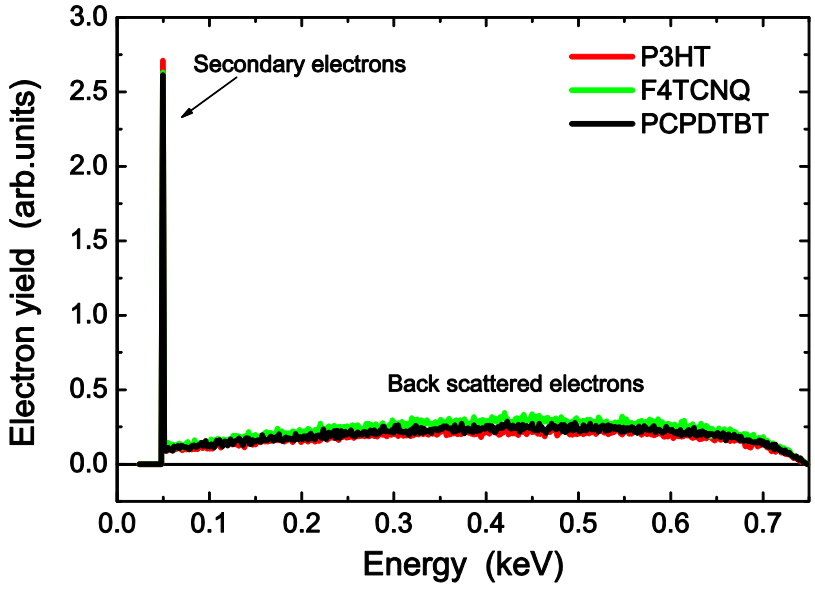

Figure 4.6 Monte-Carlo simulation of the electron yield versus energy for P3HT,PCPDTBT and F_4TCNQ. Acceleration voltage was 0.75 kV, film height 100 nm. All materials give similar yields for secondary and back scattered electrons. The simulation does not allow resolution of the secondary electron peak, which is shown as a delta peak.

All investigated materials show very similar functions of the electron yield with only minor differences in absolute values. The number of secondary electrons is slightly increased for P3HT while the backscattered electron yield is slightly higher for F_4TCNQ. Notably, the yield of backscattered electrons compared to secondary electrons is substantially lower. We rationalize the marginal differences in secondary electron yields from the negligible difference in the mean atomic number of the organic molecules' nuclei. We conclude that the differences in secondary electron yield are too low to be the underlying reason for the increased contrast in SEM. Additionally, the low mean atomic numbers of the materials indicate that the contribution of backscattered electrons in the image formation, either using the InLens or SE2 detector, is minor compared to inelastically scattered secondary electrons. From the considerations in this paragraph, a *material* or *chemical* contrast can therefore be excluded.

Another explanation for the observed contrast could be the differences in topography, as shown in the AFM images. For an investigation of these effects, the electron yield versus film depth was simulated. The plot in Figure 4.7 shows the electron yield against the depth measured from the film surface.

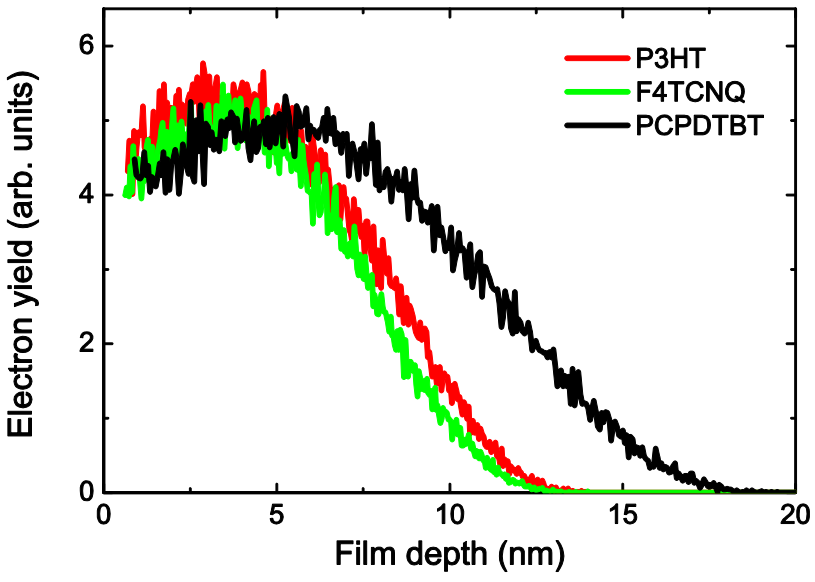

Figure 4.7 Monte-Carlo simulation of electron yield versus film depth for P3HT, PCPDTBT and F_4TCNQ. Acceleration voltage was 0.75 kV, film thickness 100 nm. P3HT and F_4TCNQ give very similar distributions while the PCPDTBT electron yield extends slightly deeper into the film.

The simulations of the electron yield give a similar shape and maximum yield for all materials. For PCPDTBT some extended gain from deeper regions of the film (about 4 nm) is observed compared to the other materials. However, due to the small overall penetration depth (ca. 15 nm) of the electron beam in the organic materials at the applied acceleration voltage of 0.75 kV, this observation is ruled out as the reason for the contrast increase. Additionally, the penetration depth is much smaller than the average film thickness of the samples (~ 100 nm). In conclusion, the simulations underline that differences in the materials' elementary properties do not explain the increased contrast observed in SEM InLens images.

4.5 Explanation of contrast increase in SEM images based on site selective charging of doped films

From the Monte-Carlo simulations in the previous Paragraph 4.4, we excluded a material contrast as the underlying mechanism for the increased contrast in SEM images taken with the InLens detector (Figure 4.3, Figure 4.4). Another explanation for the observed increase in these SEM images might be an interaction of the electron beam with the sample. Therefore, the following paragraph will discuss the charging of the sample during electron beam exposure.

Remarkably, we have observed that the increased contrast in SEM images evolves during image acquisition and is related to a certain exposure time of the samples to the electron beam. As exemplary samples we show the contrast evolution of undoped (a) and 5% doped (b) P3HT films in Figure 4.8. During SEM imaging of the *pure* P3HT film, it gradually becomes darker with exposure time (Figure 4.8a) without developing bright regions. This is indicative of a positive charge build-up in the film, leading to a lower electron yield emerging from the sample surface. On the other hand, bright patterns evolve with exposure time in *doped* P3HT films. At intermediate scanning speeds (Figure 4.8b) an increase in image contrast is observed each time the field of view is scanned, until the final contrast is reached.

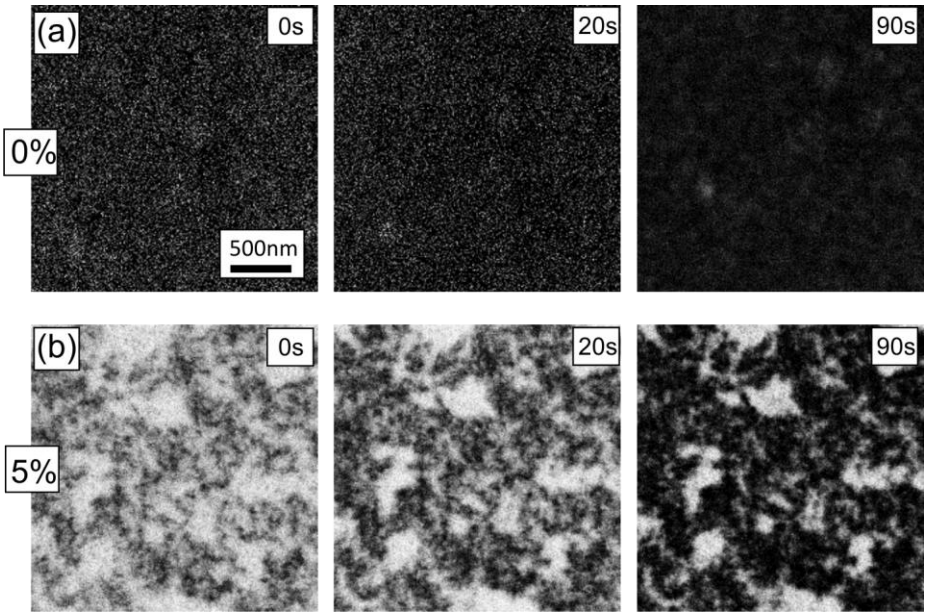

Figure 4.8 SEM images for (a) undoped and (b) 5% doped P3HT films taken with the InLens detector showing the contrast evolution with exposure time. Acceleration voltage for all images was 0.75 kV. Undoped films show a gradual homogenous darkening, while regions with increased contrast evolve in doped films.

The gradual darkening of a pure polymer film in SEM indicates that dark regions in the fully exposed SEM images of doped films are more similar to the pristine polymer, i.e. dopant deficient. F_4TCNQ is known to be a strong p-dopant for organics due to its large electron affinity and is therefore expected to be negatively charged in close vicinity of a polymer chain. Thus, we assign the increased contrast of dopant rich domains in SEM images (Figure 4.3, Figure 4.4) to electron accumulation in the dopant molecules and enhanced electron scattering by Coulomb repulsion of the incoming electrons during several scans. We also consider a more probable, beam induced, negative charging of non-ionized F_4TCNQ molecules in clusters, with respect to the polymer. These effects result in a significantly increased number of electrons backscattered and collected by the detector from dopant rich regions, giving rise to the contrast enhancement in the In-lens image.

It is possible to calculate the necessary electron dose for full development of the contrast by measuring the time until a full exposure of the film is reached. We obtain a value for the electron exposure per area of $1.6 \times 10^9/\mu m^2$. It is an interesting question how this value compares to the number of dopant molecules. The area density of F_4TCNQ molecules is calculated using the mass density of P3HT (1.1 g/cm³) [195] and F_4TCNQ (1.4 g/cm³) [196] together with the film thickness of 100 nm. One obtains values

for the dopant density of $1.2x10^5/\mu m^2$ for a doping ratio of 5%. We note that the dopant area density is lower than the number of electrons needed for full exposure of the film. Dopant molecules in clusters are less likely to dope a polymer chain, so that a lower number of these dopant molecules are negatively charged before exposure to the electron beam. We assume that the electron beam has a higher charging efficiency on the pristine F_4TCNQ molecules in clusters than charged dopant molecules dispersed in the polymer film. This leads to the conclusion that not all F_4TCNQ molecules will be equally affected by the electron beam. Identical experiments on doped PCPDTBT films show a temporal contrast evolution for high doping ratios (10%) when dopant clusters are observed.

In conclusion, we assign the increased contrast in SEM images of doped polymer films to a site selective charging of the dopant rich domains.

4.6 Conclusion

We studied the distribution of the small molecule dopant F_4TCNQ in the conjugated polymers P3HT and PCPDTBT. Low-voltage SEM was employed to monitor the surface morphology of polymeric semiconductor thin films and to characterize the distribution of dopants in the film at the nanometer scale. It has been shown that the polymer/dopant blends undergo phase separation at certain dopant concentrations, resulting in a significant change in film morphology. The critical concentration values varied for the different investigated polymers. The combination of AFM, SEM and confocal laser scanning fluorescence microscopy confirm that the clusters appearing at higher dopant concentrations are dopant rich regions. We identified site-selective charging of the sample by the electron beam as the underlying mechanism of the increased SEM contrast. Above the threshold concentration for aggregation, the number density and size of the dopant rich clusters increased. For the first time, our results presented SEM as a fast technique for mapping dopant distributions and morphology in doped conjugated polymer systems. The possibility to study dopant distribution in amorphous films with SEM is an important result for the fast morphological study of organic optoelectronic devices with doped layers.

5 Reduced charge transfer exciton recombination in doped organic semiconductor heterojunctions

In this chapter the effect of molecular doping on the recombination of electron-hole pairs (CT excitons) localized at conjugated polymer:fullerene interfaces is studied. We demonstrate that doping at low concentrations with p-type dopant molecules reduces the interfacial recombination via CT excitons and results in a favoured formation of separated charge carriers. The employed dopant molecules (F_4TCNQ) exhibit a strong electron affinity and are therefore strong electron acceptors. Addition of these p-type dopants to the polymer in solution facilitates ground state electron transfer from polymer HOMO to dopant LUMO. Accordingly, the background hole density in the polymer increases. This leads to a filling of the density of states' low-energy tail in the polymer HOMO. We use transient photoluminescence (PL) to reveal a reduced initial recombination of charge transfer (CT) excitons as a function of increasing dopant concentration. In addition, probing the generation of separated carriers (polarons) with mid-infrared (MIR) photo-induced transient absorption (PIA) demonstrates an increase in polaron density for doping ratios up to 4% weight. The experimental data is fitted with a rate equation model. The simulations indicate that doping reduces the probability for CT exciton formation and, by this, enhances polaron generation. Consistent with the spectroscopic results, we find an increased short circuit current in solar cells with a doped active layer, which leads to an overall increase in solar cell performance. We interpret our results based on a reduced formation of emissive charge transfer excitons in doped blends, induced by state filling of immobile tail states in the polymer HOMO.

5.1 Motivation to study the effect of changes in electronic structure on charge separation

The doping of conjugated polymers has been recently explored to modify the electrical characteristics of solution processible semiconductors [4,14,197,198]. This work has shown that background hole density and conductivity can be increased several orders of magnitude in amorphous organic polymer films. Different amounts of chemical doping have resulted in increased charge carrier densities, reaching levels sufficient for metallic conductivity [199]. Similarly interesting, but less investigated is the influence of doping on optical excitations [200], as these play a crucial role in the functioning of devices such as solar cells and light emitting diodes [201]. In pristine polymers several investigations have clarified that strongly-bound Frenkel excitons, with binding energies of ~0.5 eV [47], are the primary photo-excitations in this class of materials [202,203]. As a consequence, effective charge separation in organic semiconductors preferentially occurs at type II heterojunctions with a favourable energy offset for exciton dissociation [204]. In general, the process, leading to fully separated electrons and holes, is thought to be influenced by an intermediate state, where carriers are localized on two adjacent molecules [94,95,205]. These localized electron-hole pairs are still bound by a weakened Coulomb interaction of ~0.2 eV [98]. Such states have been termed CT excitons [95,206] or exciplexes [96,108] and have recently aroused considerable experimental and theoretical interest [75,101,207]. It remains a fundamental question whether emissive CT excitons are necessarily populated for each charge separation event, or if their appearance is entangled with the electronic characteristics of the materials constituting the heterojunction and the density of states (DOS) experienced by the photo-excitations. In other words, can recombination via CT excitons be reduced in favour of charge separation by influencing the electronic properties of the materials? Doping is known to influence these electrical characteristics, because of an increased ground-state carrier density and filling of localized states [192]. Therefore we chose doping as a suitable tool to study the effect of changes in the electronic structure of the heterojunction on charge separation.

5.2 Preparation of doped PCPDTBT:PCBM blend films

We have focussed our experiments on blends between [6,6]-phenyl C_{61}-butyric acid methyl ester (PCBM) and the conjugated polymer (Poly[2,1,3-benzothiadiazole-4,7-diyl[4,4-bis(2-ethylhexyl)-4H-cyclopenta[2,1-b:3,4-b']dithiophene-2,6-diyl]])

(PCPDTBT) [120]. PCPDTBT was provided from the group of Prof. Scherf /Universität Wuppertal) with a molecular weight of 22.000 g/mol. PCBM was purchased from Nano-C. F4TCNQ was obtained from Sigma-Aldrich. Sketches of the molecular structures and the energy levels of the investigated materials are displayed in Figure 5.1.

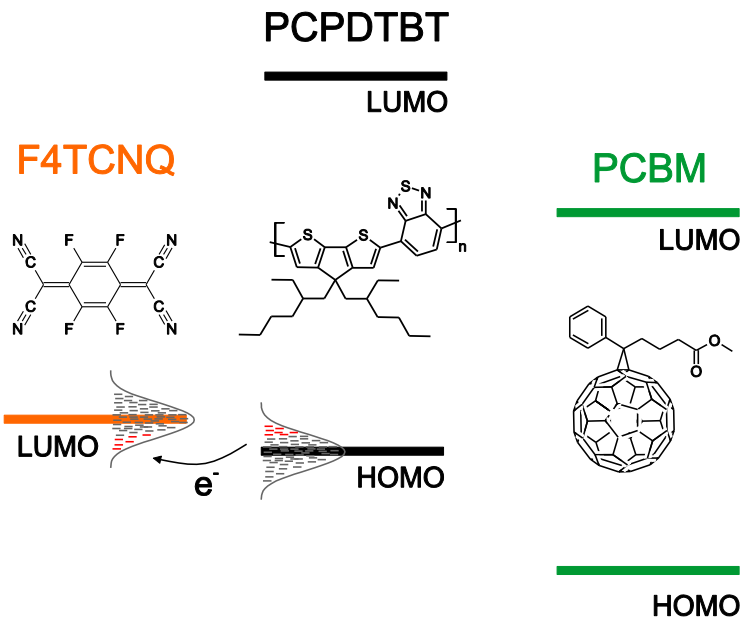

Figure 5.1 Energy level scheme of the investigated materials. The molecular structures of the materials are shown as insets. The Gaussian broadened polymer HOMO and dopant LUMO levels, present in disordered films, are drawn. The doping mechanism occurs by a direct electron transfer from the polymer HOMO to the dopant LUMO, as shown. The states marked red in the polymer HOMO indicate holes created by the doping mechanism, while the marked states in the F_4TCNQ LUMO relate to transferred electrons.

To achieve effective hole doping of PCPDTBT, we used the small molecule 2,3,5,6-Tetrafluoro-7,7,8,8-tetracyanoquinodimethane (F_4TCNQ), which was added to the polymer solution before mixing with PCBM. F_4TCNQ is known to be an efficient dopant for conjugated polymers, resulting in p-type doping [10]. This effect is due to the favourable alignment of polymer HOMO and F_4TCNQ LUMO (Figure 5.1), allowing for direct electron transfer from polymer to dopant. The transfer of electrons generates positively charges holes in the polymer HOMO. These will fill the immobile tail states of the HOMO density of states, since these states are lowest in energy. For the preparation of solutions, chlorobenzene was used as solvent for all samples. First, pure PCPDTBT and F_4TCNQ solutions were prepared. To obtain doped polymer solutions with a defined doping ratio, the respective amount of F_4TCNQ solution was added to

the pure polymer solution. The dopant-polymer mixture was then added to PCBM powder to obtain 1:1 (polymer:fullerene) weight ratio blends. Thin films were spin-coated on quartz or CaF_2 substrates in N_2 atmosphere. The PCPDTBT:PCBM ratio was kept constant for all samples, whereas different weight percentages of F_4TCNQ with respect to the polymer were explored. Transmission electron microscopy (TEM) images of the samples were taken to investigate changes in the blend morphology upon addition of the dopant (Figure 5.2). These images allow the investigation of the film morphology on the length scale of exciton migration (~20 nm [71]), which is a critical length scale for the charge separation process investigated in this chapter. The visible dark spots are impurities on the film surface used to focus the image, as the homogeneous structure of the film makes focussing on the film surface very difficult. The undoped blend, shown in Figure 5.2a, exhibits a fine, intermixed structure as reported previously [53]. This indicates an intimate mixing of polymer and fullerene domains.

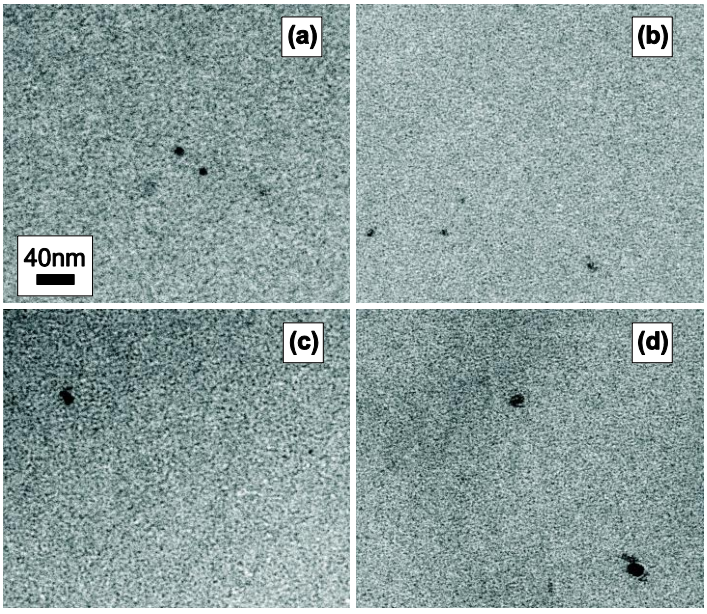

Figure 5.2 Images of PCPDTBT:PCBM blends doped at different ratios with F_4TCNQ taken with transmission electron microscopy The doping ratios are (a) undoped (b) 2% (c) 4% (d) 5% doping per weight of the polymer. Samples were floated from glass substrates and transferred onto carbon grids. Electron beam voltage was 80 kV.

Similar homogeneous blend morphologies are observed for doped films independent of dopant concentration. No changes in film morphology are observed for increasing dopant concentrations up to the maximum employed dopant ratio of 5%. The incorporation of dopant molecules apparently does not alter the structural properties of

the PCPDTBT:PCBM blends, i.e. no clustering of molecules is observable on the length scale of exciton migration. This correlates well with the SEM pictures reported in Chapter 4 in Figure 4.3. From this we can conclude that the observed spectroscopic effects described in the following paragraphs are related to changes in the electronic properties of the material system and not due to differences in morphology.

5.3 Signature of polarons in absorption spectra of doped PCPDTBT:PCBM films

Optical absorption spectroscopy offers the possibility to study the effect of doping on the electronic structure of the system. Due to the alignment of the PCPDTBT HOMO and the F_4TCNQ LUMO, direct electron transfer from polymer to dopant in the ground state leads to an increased background hole density in the polymer without optical excitation. The additionally created charges (polarons) will exhibit characteristic transitions in the near-infrared and mid-infrared region, as discussed in Paragraph 2.4.2. The absorption measurements on thin films of doped and undoped PCPDTBT:PCBM blends are shown in Figure 5.3.

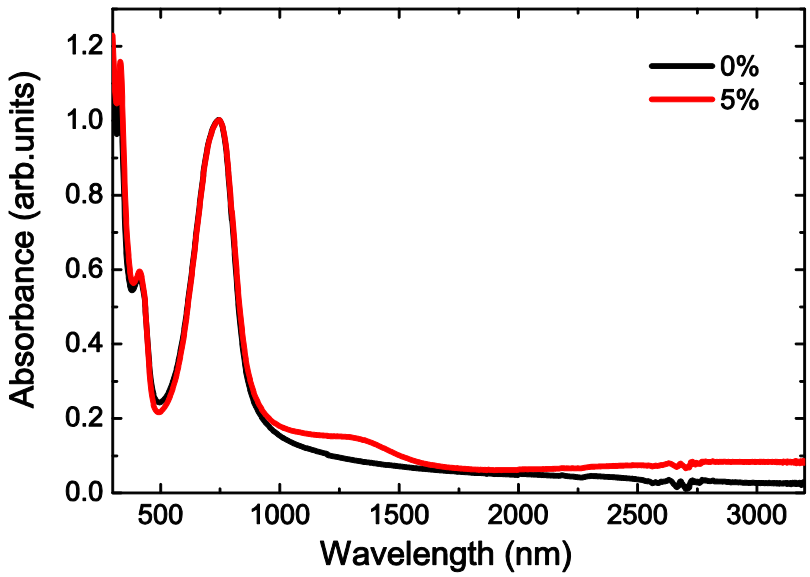

Figure 5.3 Absorption spectra for PCPDTBT:PCBM thin films (1:1 blends) undoped and doped at 5% with F_4TCNQ. Spectra are normalized at the main transition peak of PCPDTBT (750 nm). Ground state transitions occur below 1000 nm, while for doped samples additional polaron transitions are observed above 1000 nm.

For the undoped blends one can distinguish the main transition of PCPDTBT around 750 nm and a second transition around 400 nm which is significantly lower in oscillator strength. This second transition appears as a shoulder on a strong absorption feature rising towards 300 nm which is the onset of the PCBM absorption. Above 1000 nm the absorption of the main PCPDTBT transition slowly decreases and no further spectral features are visible. The small peaks around 2750 nm are due to impurities in the CaF_2 substrate. The doped sample shows similar transitions compared to the pure blend up to 1000 nm and there are also no substantial changes in peak ratio between the individual transitions. However, above 1000 nm new features are visible, i.e. a first peak around 1300 nm and a second, spectrally broader one, centred around 2800 nm. Due to the range limitation of the spectrometer wavelengths above 3300nm could not be accessed, so that the mid-infrared peak was not fully detected. The additional transitions in the doped samples are characteristic for the P_1 (mid-IR) and P_2 (near-IR) transitions of polarons in PCPDTBT, as explained in Paragraph 2.4.2 and shown in reference [53]. This observation indicates the generation of polaron states in PCPDTBT by molecular doping. A quantitative assessment of the charge carrier density from absorption measurements was difficult due to uncertainties in the absorption cross-sections. However, these measurements show in a qualitative way, that doping of PCPDTBT with F_4TCNQ leads to the formation of polarons in the conjugated polymer.

5.4 Reduced CT exciton photoluminescence intensity with increasing doping ratio

A possible technique to study the properties of primary excitations is steady-state photoluminescence (PL) spectroscopy. Figure 5.4 shows the PL spectra of PCBM (a), PCPDTBT (b) and a blend of these two materials in a 1:1 weight ratio (c). Thin films of the pure materials (a,b) show the typical PL features ascribed to the singlet exciton transitions [120] with a strong 0-0 transition followed by vibrational transitions at lower energies. In contrast, the blend emission is characterized by a single broad unstructured emission peak at 1.17 eV. No residual PL from Frenkel excitons of either PCBM or PCPDTBT, which is expected to appear in the energy range above 1.4 eV (Figure 5.4a,b), is detected.

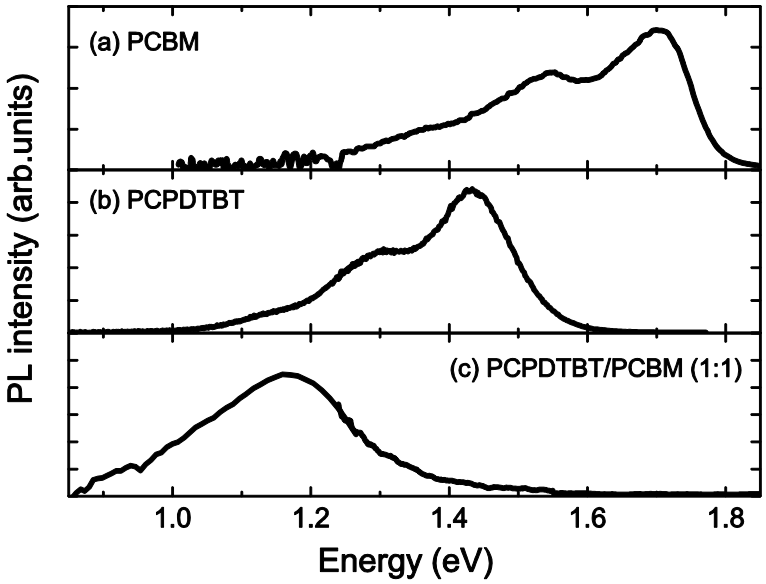

Figure 5.4 Thin film photoluminescence spectra of (a) pure PCBM (b) pure PCPDTBT (c) PCPDTBT:PCBM blend (1:1 weight ratio). Excitation wavelength was 3.1 eV. The blend film shows a red-shifted emission band not visible in either of the pure materials spectra.

In agreement with prior studies on the PL of such a blend, the emission centred at 1.17 eV is assigned to a CT exciton; a bound electron-hole pair at the interface [120]. Such an excitation considers the hole localized on the HOMO of the polymer and the electron on the LUMO of the fullerene. To study the effect of doping on these transitions, Figure 5.5 displays the PL intensity of the CT exciton emission for different doping ratios with F_4TCNQ, which is a measure for the radiative recombination of CT excitons.

The experiment shows a reduced PL intensity in the presence of an increasing amount of F_4TCNQ dopant. The data demonstrate a monotonic quenching of the CT PL as a function of dopant concentration. Interestingly one cannot distinguish any shift in peak position. Accordingly, the addition of the dopant does not lead to a shift in the energy of the emissive CT exciton, e.g. variations in the CT exciton energy levels. Our results give a first indication, that doping affects the charge generation process, since CT excitons play an important role therein. For example, a correlation between reduced CT exciton emission intensity and increased solar cell performance has been shown [101].

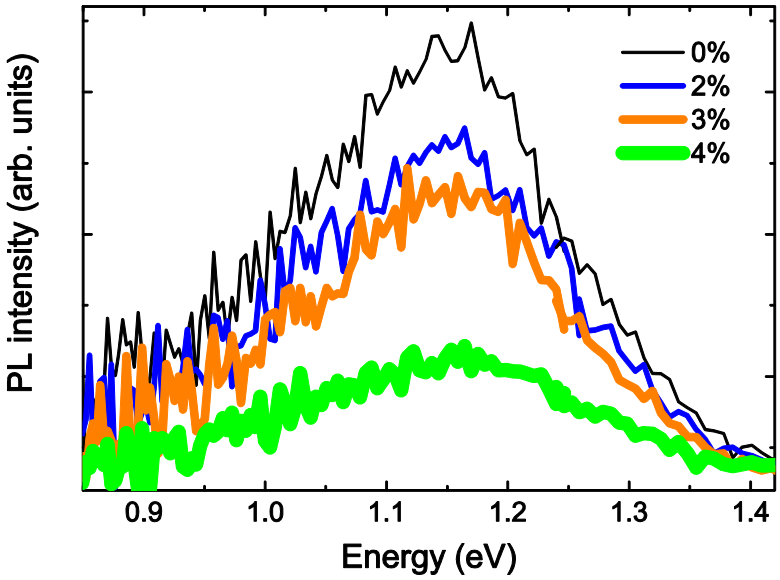

Figure 5.5 Photoluminescence spectra of PCPDTBT:PCBM blends (1:1 weight ratio) doped at different amounts with F_4TCNQ focussing on the emission range of CT excitons. A monotonous decrease in photoluminescence intensity with increasing doping is observed.

Although the observation of CT emission quenching is interesting, it is not clear from steady state PL experiments alone, which doping-related mechanism influences the recombination characteristics of CT excitons. The observed loss in CT exciton emission can be either due to a reduced initial *formation* of CT excitons or a reduced *lifetime* of the emissive CT excitons. To gain further insights on the underlying mechanism, time-resolved PL experiments were performed.

5.5 Ultra-fast initial quenching of CT exciton emission in time-resolved PL

Time resolved PL was measured exciting the samples with 200 fs short laser pulses, generated with a tuneable femtosecond Ti:sapphire amplifier at 1.65eV. The emitted photoluminescence was detected with an IR sensitive streak camera and interference bandpass filters were used to selectively probe the CT emission in the near-IR. The dynamics of the CT emission at 1.17 eV were measured to gain insights on the quenching process as a function of doping ratio. The samples were kept in vacuum ($<10^{-6}$mbar) at T = 295 K during all measurements. Figure 5.6 shows the normalized decays on a semi-logarithmic scale. For the undoped sample (black line) an initial fast

decay is followed by a longer living component, giving rise to a bi-exponential decay with τ_1=20 ps and τ_2 =360 ps. From the steady state spectra of the pure PCPDTBT films (Figure 5.4b) it is discernible that the spectral range of CT exciton and PCPDTBT singlet exciton emission overlap. Therefore, the fast decay component, almost within the setup resolution, can be assigned to residual emission from singlet excitons in PCPDTBT. Due to the short lifetime of the singlet exciton signal this emission is not visible in the steady state emission spectra of the blends.

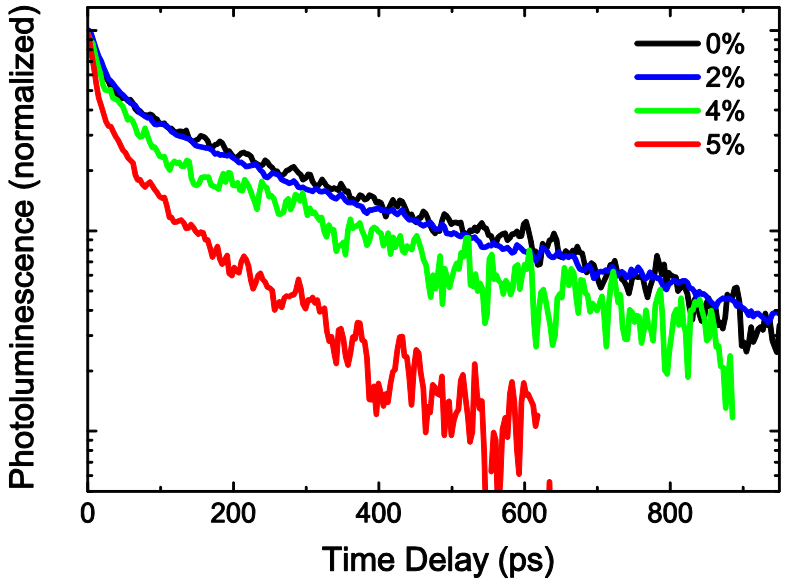

Figure 5.6 Normalized transient photoluminescence of PCPDTBT:PCBM blends (1:1) doped at different ratios with F_4TCNQ measured at 1.17 eV. Excitation at 1.65 eV. A bi-exponential decay is observed, with the fast part due to residual emission from Frenkel excitons and the longer decay representing the CT emission. No change in lifetimes is detected for doping ratios below 5%.

For increasing dopant concentrations there is no change in the long decay component of the decay (blue/green lines) for doping ratios below 5%. This indicates that at low doping ratios the decay mechanism of the CT excitons does not change. No other decay channels, e.g. recombination at dopant molecules or dopant induced charge carriers, are opened up, besides the ones already existing in the undoped blend. Only at higher dopant concentrations, above a threshold of 5%, the dynamics exhibit a significantly faster decay (5%: τ_2 =150 ps). This effect arises because of the significant background hole density at these doping ratios. Interaction with these charge carriers leads to additional recombination mechanisms, like exciton-polaron quenching, as will be

discussed in detail in Paragraph 5.6. However, significant differences among all samples can be noticed in the *initial amplitude* of the signal at time zero $I_{PL}(t=0)$, as demonstrated in Figure 5.7.

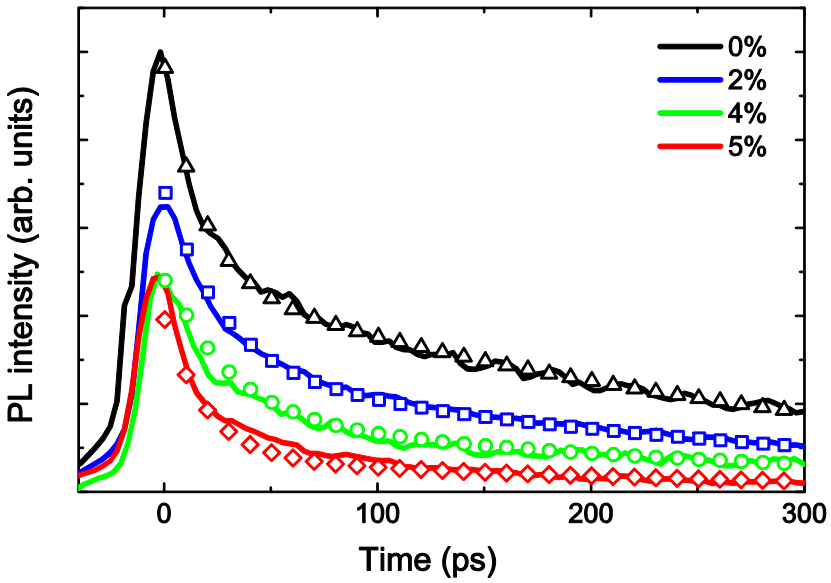

Figure 5.7 Transient photoluminescence of PCPDTBT:PCBM blends (1:1) doped at different ratios with F_4TCNQ measured at 1.17 eV. Excitation at 1.65 eV. A decrease in photoluminescence intensity at time zero occurs with increasing doping. Symbols represent fits based on the rate equation model presented in Paragraph 5.8.

There is a strong monotonic decrease in PL amplitude from the undoped blend to the 2% doped (-35% peak intensity) and the 4% doped sample (-51% peak intensity). However, the relation between doping ratio and peak intensity loss is not linear, which indicates that the underlying effect is not explained from a simple quenching of CT excitons by the added dopant molecules. This interpretation is supported by the unchanged CT exciton lifetime, which would be reduced upon dopant induced CT exciton quenching. The steady-state (Figure 5.5) and time resolved PL data (Figure 5.7) can be explained considering two hypotheses: (i) the increased carrier density induced by the dopant in the polymer domains influences the rate of recombination, changing the non-radiative rate of the CT exciton luminescence; or (ii) the carrier density has an influence on the charge separation channel, which lowers the probability for the population of the bound *emitting* CT exciton and results in separated electrons and holes (polarons), already on a time scale comparable to the resolution of the PL transients

(~20 ps). In the following paragraph the second possibility will be addressed by transient absorption measurements, probing the polaron yield in the blend system.

5.6 Increased polaron signal with increasing doping ratio in transient absorption measurements of blend films

In this paragraph we use transient absorption measurements to test the hypotheses raised at the end of Paragraph 5.5. Changes in the recombination kinetics as expected from hypothesis (i) would require a change in the lifetime of PL, only observed above 4%. Therefore we have explored hypothesis (ii) by monitoring the fast formation of polarons by femtosecond photo-induced absorption (PIA) spectroscopy [208]. Transient PIA experiments were conducted with 100 fs pump and probe pulses generated with a Ti:sapphire laser after optical parametric amplification [209,210]. In such an experiment electron-hole pairs are photo-generated by a short laser pulse (pump). The formation and recombination of polarons is monitored by a second pulse (probe) delayed in time and with a suitable photon energy, resonant with the polaron absorption. The polaronic nature of charge carries in organic semiconductors gives rise to optical transitions in the IR region of the spectrum [211]. For PCPDTBT:PCBM blends two prominent polaron transitions have been observed in steady-state photo-induced absorption (PIA) at 0.4 and 0.9 eV in reference [53]. We have opted to probe the polaron absorption in the mid-IR at 0.4 eV, thus avoiding the overlap with excitonic features, e.g. triplets in the near-IR, which may disturb the genuine signal of polarons [53]. Overlap of optical beams and beam-walking effects were carefully adjusted using markers and a beam-profiler camera. Excitation intensities were kept below 5 $\mu J/cm^2$ (~1.5 10^{18} excitons/cm^3), thus minimizing exciton annihilation effects [202]. Samples were measured in vacuum (10^{-6} mbar) at T = 295 K.

Figure 5.8 shows PIA transients probing the photo-induced polaron population for doped and undoped films. The signal amplitude, expressed as differential transmission in the probe $\Delta T/T$, is proportional to the photo-generated polaron density [P](t) according to

$$\frac{\Delta T}{T}(0.41eV, t) = \sigma_P(0.41eV) \cdot d \cdot [P](t)\,, \qquad (5\text{-}1)$$

The polaron cross-section [σ_P(0.41 eV) = 1.28 10^{-16} cm^2] was taken from published chemical doping measurements on PCPDTBT [194] using the very strong electron acceptor $SbCl_5$. The film thickness *d* was determined from measurements with a profilometer.

For the undoped sample the polaron signal rises within the temporal resolution of the setup and decays only slightly over the whole investigated time range with a lifetime $\tau \sim 1.4$ ns. This result is a typical signature of long-lived polarons in organic semiconductor heterojunctions. Also for the doped samples we observe a rise in the polaron signal within the time resolution of the setup. However, the data exhibits a difference in the time zero amplitudes, $\Delta T/T(t=0)$, compared to undoped samples. Remarkably, at time zero the 2 and 4% doped blends have larger signal amplitudes with respect to the 0% by a factor of 1.4 and 1.7, respectively.

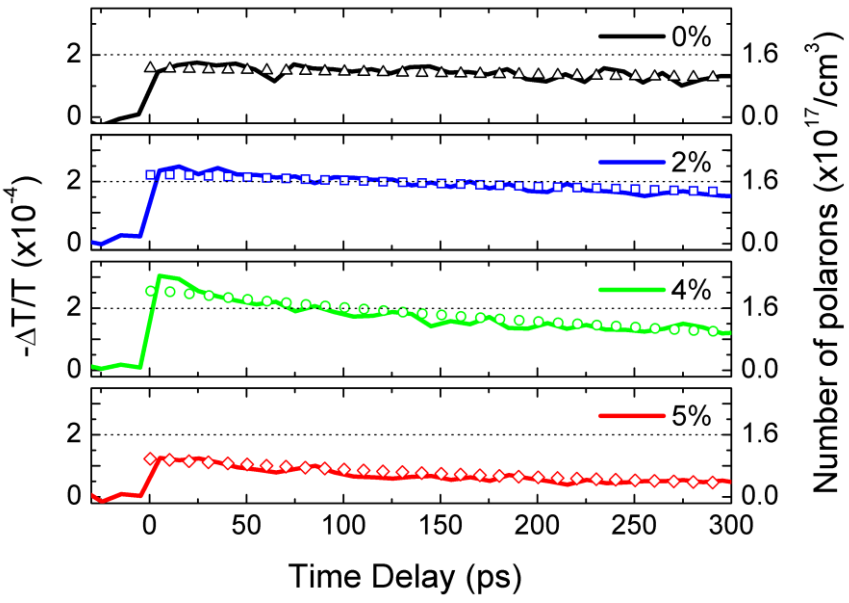

Figure 5.8 Transient absorption of PCPDTBT:PCBM (1:1) blends doped at different ratios with F_4TCNQ. Pump (3.1 eV) and probe (0.4 eV) pulses had a cross-correlation of ~150 fs. An increase in polaron population at time zero is observed up to 4% doping. With higher doping a decrease in amplitude and faster decay occurs. Symbols represent fits based on the rate equation model presented in Paragraph 5.8.

This observation indicates that, within our time resolution (~150 fs), there is a larger density of polarons upon photo-excitation of blends which were doped with 2 and 4% F_4TCNQ. For higher doping concentrations (5%), the amplitude drops below the one for the undoped sample already at time zero. On a longer time scale (Figure 5.9) the

dynamics for the undoped and 2% doped film are comparable with a quasi mono-exponential decay time of >1 ns. However, we stress that the polaron density of the 2% doped samples lies above the undoped reference for the whole measured time range. For 4% doping we observe an even higher initial rise with the polaron signal dropping to the value of the undoped reference within 300 ps. We conclude that up to 2% doping a larger population of charge carriers is photo-generated, with only small differences in the long time scale recombination dynamics. We note that the increase in signal amplitude for the 2 and 4% sample is in qualitative agreement with the observed loss in CT exciton population calculated from transient photoluminescence experiments in Paragraph 5.5. This point will be addressed in more detail in the rate equation model presented in Paragraph 5.8. We start to observe faster (<1 ns) recombination processes at 4%, which dominate at 5%. We attribute these to the increased background charge density due to the high doping ratios. Therefore we suggest Auger recombination between singlet excitons and doping induced charge carriers as a recombination channel opening up with increasing doping ratio.

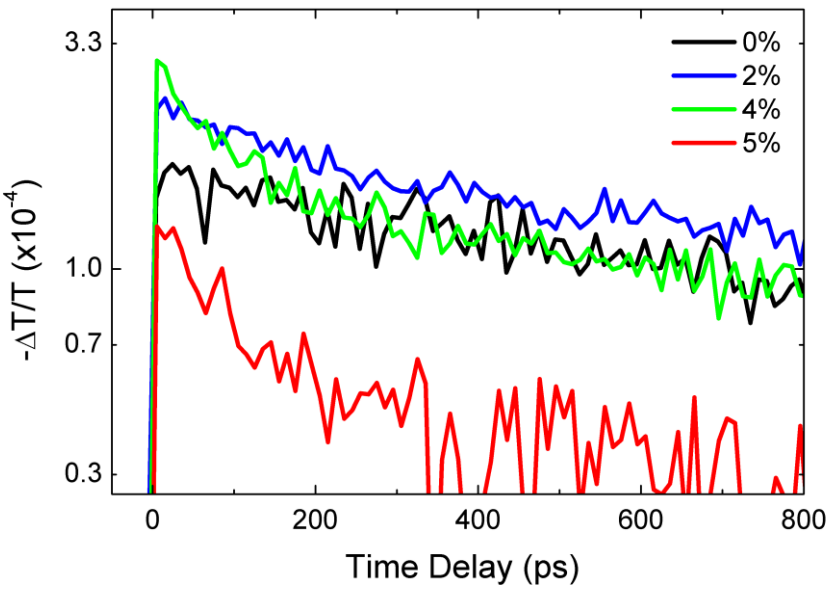

Figure 5.9 Transient absorption of the polaron population in PCPDTBT:PCBM (1:1) blends doped at different ratios with F_4TCNQ shown on logarithmic scale. Pump (3.1 eV) and probe (0.4 eV) pulses had a cross-correlation of ~150 fs. Samples exhibit similar lifetimes up to 4% doping. Shorter lifetimes are observed at higher doping ratios.

Comparing the PL and PIA of samples with the same doping concentration we note that the two experiments reveal different decay dynamics. This is a strong indication that

recombination of charges populating the CT state and of separated polaron states follows two distinct mechanisms apparently not interrelated. The experiments described in Figure 5.7 and Figure 5.8 suggest that the introduction of a higher hole density by doping is influencing the fate of photo-excitations at early times during the formation of emissive CT excitons. Consistent with this picture is the decrease in the PL and the larger PIA $\Delta T/T$ from polarons at time zero. The observations exclude that the CT emission intensity is quenched because of a non-radiative recombination channel, at least up to 4% doping, and point to the fact that doping influences whether the initial photo-excitations will form an emissive CT exciton or will result quasi-instantaneously in separated polarons. To address this interpretation, a rate equation model is set up in Paragraph 5.8 to fit the experimental results and study the rate constants for CT exciton and polaron formation.

5.7 Effect of doping on the polaron signal in transient absorption of PCPDTBT films

In order to assign the observed increase in polaron yield upon doping to effects occurring at the interface between polymer and fullerene, doping induced changes on the charge generation in the pure polymer have to be excluded. Therefore the transient absorption of polarons in pure PCPDTBT films doped at different ratios with F_4TCNQ is investigated (Figure 5.10). We assume that in blends the dopants are equally distributed in both phases. Thus, the dopant concentration in pure PCPDTBT films corresponds to twice the values of blends. The results for the polaron yield in undoped polymer films (black line) show a fast initial rise of the polaron signal within the resolution of the setup and a faster decay (τ=3.7 ps) compared to the blend films. This faster recombination is a typical result for polaron signals in pure organic polymer films without an acceptor phase for efficient long-range charge separation. The polaron signal for 1% doped polymer films (red line) shows an identical rise and decay without differences in amplitude or lifetime compared to the undoped polymer. At higher doping ratios (2%) the signal amplitude is slightly reduced, which we attribute to Auger recombination effects, as mentioned in Paragraph 5.6.

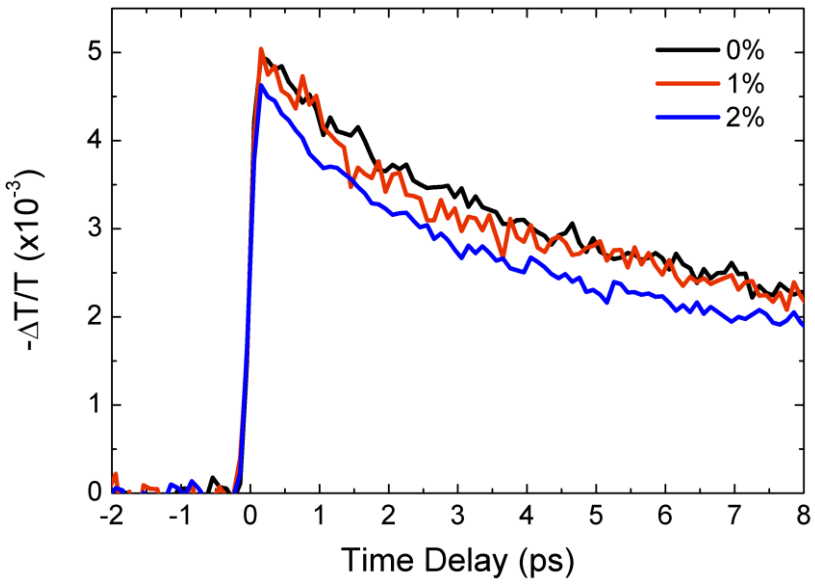

Figure 5.10 Transient absorption of the polaron population in PCPDTBT films doped at different ratios with F_4TCNQ. Pump (3.1 eV) and probe (0.4 eV) pulses had a cross-correlation of ~150 fs. No significant changes in amplitude and lifetime are observed up to 2% doping.

An increase in polaron signal as observed for doped blend films is not visible for pure PCPDTBT. This result indicates that the observed *increase* in polaron density for doped blend films is not due to processes related to the pure polymer phase, since in doped polymer films one observes *no change* or, for higher doping ratios, even a *decrease* in polaron signal.

5.8 Reduced CT exciton formation rate indicated by fitting of experimental results with rate equation model

To discuss our observations in a more quantitative way, we modelled the PL and PIA transients with a system of coupled rate equations. The model, based on the scheme of Figure 5.11, considers that the initially photo-generated Frenkel excitons can form CT excitons or polarons with two different probabilities given by the time constants $\tau_{CT\text{-}f}$ and $\tau_{P\text{-}f}$. Frenkel and CT excitons can recombine giving rise to the first ($\tau_{FR\text{-}r}$) and second ($\tau_{CT\text{-}r}$) component of the PL decay in Figure 5.7, while polarons are detected in the PIA experiment. The set of rate equations used for the simulations is given in Equations **(**5-2**)** to **(**5-4**)**. In these equations [FR], [CT] and [P] represent the population densities for Frenkel excitons, radiative CT excitons and polarons, respectively. The

different time constants are τ_{FR-r}, τ_{CT-f}, τ_{P-f}, τ_{CT-r} and τ_{P-r} which correspond to the recombination time of Frenkel excitons in PCPDTBT, the transfer time to a CT exciton, the charge transfer time to separated polarons, the recombination time of the CT exciton and the recombination time of the polarons.

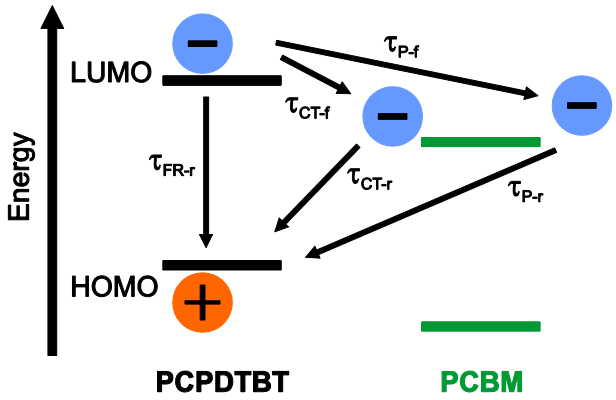

Figure 5.11 Energy scheme for the HOMO and LUMO levels of PCPDTBT and PCBM together with the transitions used in the rate equation model.

The model is intentionally kept as simple as possible, neglecting further details of the charge separation process, since the focus of the simulation is on the role of CT excitons in charge separation.

$$\frac{\partial[\mathrm{FR}](t)}{\partial \mathrm{t}} = -\frac{[\mathrm{FR}](t)}{\tau_{\mathrm{FR-r}}} - \frac{[\mathrm{FR}](t)}{\tau_{\mathrm{CT-f}}} - \frac{[\mathrm{FR}](t)}{\tau_{\mathrm{P-f}}} \qquad (5\text{-}2)$$

$$\frac{\partial[\mathrm{CT}](\mathrm{t})}{\partial \mathrm{t}} = \frac{[\mathrm{FR}](t)}{\tau_{\mathrm{CT-f}}} - \frac{[\mathrm{CT}](\mathrm{t})}{\tau_{\mathrm{CT-r}}} \qquad (5\text{-}3)$$

$$\frac{\partial[\mathrm{P}](t)}{\partial \mathrm{t}} = \frac{[\mathrm{Fr}](\mathrm{t})}{\tau_{\mathrm{P-f}}} - \frac{[\mathrm{P}](t)}{\tau_{\mathrm{P-r}}} \qquad (5\text{-}4)$$

We note that a model considering the generation of polarons from dissociation of CT excitons was not capable of fitting our experimental results. Since undoped PCPDTBT:PCBM blends exhibit a photo-induced electron transfer on a time scale of 200 fs [78], we have considered this value for τ_{P-f} and τ_{CT-f} in the undoped sample. The recombination time of CT excitons (τ_{CT-r}) was fixed at 300 ps for all the samples up to 4% doping, as well as the recombination time of Frenkel excitons in PCPDTBT at 125 ps. The values for these parameters were determined from transient

photoluminescence experiments. For 5% doped samples the recombination times were varied to obtain the best fitting to the experimental data.

The simulated transients, reported as symbols in Figure 5.7 and Figure 5.8, are in good agreement with the experiments. Differences in the signal amplitudes of transient PL and transient PIA, which are the most important observations of our study, are quantitatively described by variations in the initial formation rate of recombining CT excitons. This rate (expressed as inverse lifetimes) is as high as 1/0.2 ps for undoped samples, but reduces to1/0.5 ps at 2% doping and 1/0.95 ps at 4-5% (Table 5.1). In our model, CT exciton formation and polaron formation are competing processes. By reducing the formation rate of recombining CT excitons while keeping the formation rate for polarons constant, the probability of polaron formation is becoming more probable. The reduced formation rate of recombining CT excitons is our main finding and demonstrates the underlying mechanism behind the increased polaron yield, observed in doped samples.

Doping [%]	$\tau_{FR\text{-}r}$ [ps]	$\tau_{CT\text{-}f}$ [ps]	$\tau_{P\text{-}f}$ [ps]	$\tau_{CT\text{-}r}$ [ps]	$\tau_{P\text{-}r}$ [ps]
0	125	0.2	0.2	300	1400
2	125	0.5	0.2	300	1000
4	125	0.95	0.2	300	400
5	0.15	0.95	0.2	250	300

Table 5.1 Parameters used in rate equation model to fit the experimental PL and PIA data for doped PCPDTBT:PCBM blends

The PIA decays for the 4 and 5% sample were modelled with shorter recombination lifetimes of Frenkel excitons and polarons. This confirms that additional recombination processes such as exciton-polaron quenching, i.e. Auger processes, are occurring. Based on the mechanism proposed in this model we state that Frenkel excitons in the presence of doped polymer chains are less prone to form recombining CT excitons. This leads to a more favourable formation of polarons up to 4% doping. For the 5% sample faster Frenkel exciton and polaron recombination channels are activated on a time scale of 150 fs and 300 ps, respectively.

5.9 Doping induced efficiency enhancement in solar cell performance

The investigated blends have attracted substantial interest as active layers in photovoltaic applications recently [120,121,131]. In order to study the effect of doping on the photovoltaic performance, solar cells with doped PCPDTBT:PCBM layers were fabricated. It has been shown recently that the addition of additives like 1,8-diiodooctane can improve the solar cell performance [130]. We chose not to use additives in order to keep the active layer properties similar to the spectroscopic samples. However, to obtain significant solar cell performance, the PCPDTBT:PCBM ratio had to be increased to 1:2. We assign this to the formation of improved charge percolation pathways at higher PCBM content. Figure 5.12 shows the current density–voltage (I-V) curves for PCPDTBT:PCBM blends with F_4TCNQ doped at different ratios.

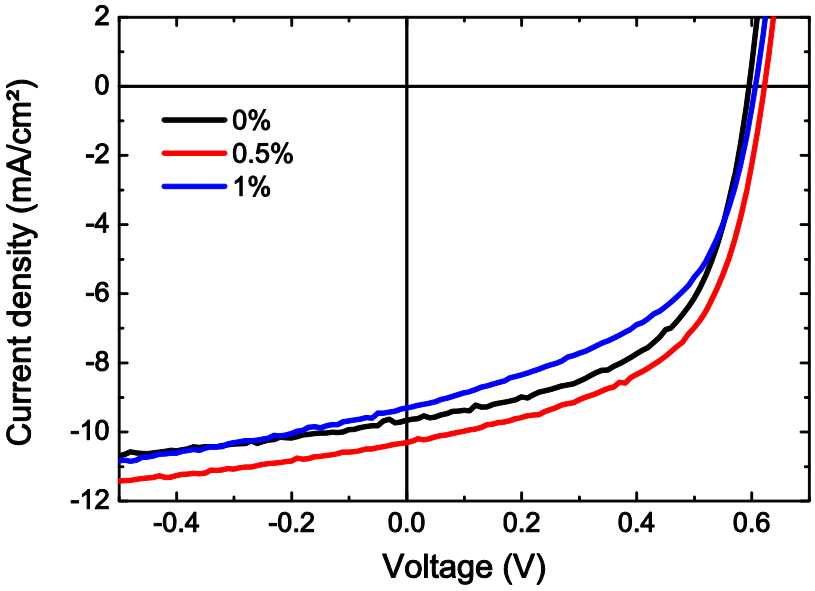

Figure 5.12 I-V curves for PCPDTBT:PCBM blends (1:2) doped with F_4TCNQ at different ratios, recorded with an AM1.5 solar simulator. An increase in short-circuit current is observed for 0.5% doping. No significant changes in open circuit voltage or fill factor are measured. For higher doping ratios the short circuit current and solar cell performance decrease.

We find an increase in short circuit current J_{SC} from 9.66 mA/cm² in the undoped cells to 10.31 mA/cm² for 0.5% doping. Also the open circuit voltage V_{OC} rises from 0.59 V to 0.62 V. No significant changes in fill factor (FF) are observed up to 0.5% doping.

Accordingly, the higher J_{SC} and V_{OC} lead to an improvement in power conversion efficiency from 3.3% to 3.6%. These observations are consistent with the increased polaron yield upon doping, as seen from spectroscopic measurements in Paragraph 5.6. For higher doping ratios (1%), the cell performance falls below the undoped reference. This effect is mainly due to a lower J_{SC} and FF. We assign the reduced performance at higher doping ratios to exciton-polaron recombination processes due to the dopant induced background charge density. Interestingly, the doping ratios used in cells had to be lower than in the spectroscopic studies, which can be rationalized by the charge carrier extraction in solar cells. During transport to the electrodes on a microsecond scale a larger volume is sampled, which makes interactions with doping induced localized charge carriers more likely. Therefore recombination losses through these trap states are more pronounced in cell performance than in optical spectroscopy, which was only probing the first nanosecond after charge generation.

Another aspect of doping with respect to solar cell performance lies in the effects on electrical properties. IV curves for doped and undoped solar cells measured without illumination are shown in Figure 5.13.

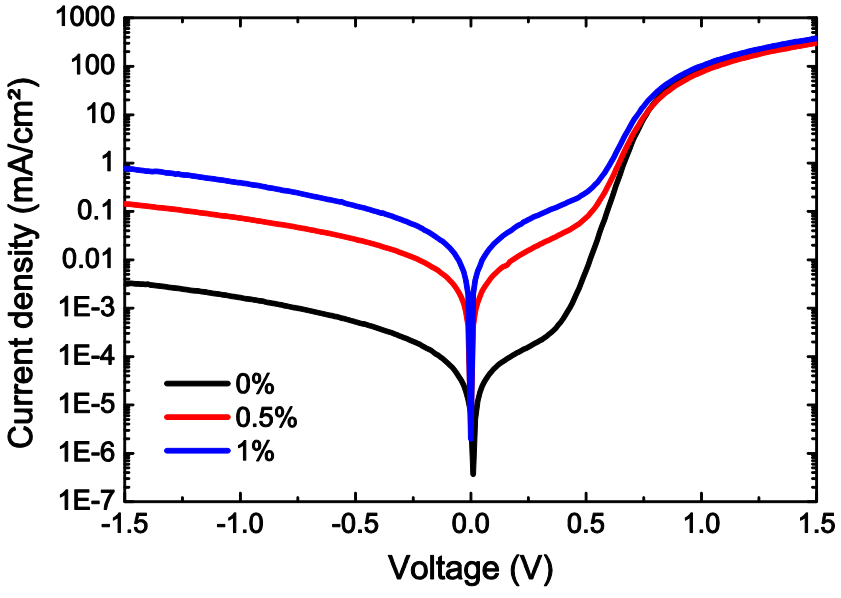

Figure 5.13 I-V curves for PCPDTBT:PCBM blends (1:2) doped at different ratios with F_4TCNQ recorded in the dark. An increase in hole conductivity with increasing doping is observed up to 1% doping.

One observes an increase in current density upon doping for holes and also electrons. A positive effect of doping on conductivity has been shown for pure polymers before [11] and, as our results indicate, can also be observed in polymer:fullerene blends. Therefore, the increase in cell performance is also partially due to improvements in charge carrier extraction and transport. For further information on the effects of doping on electrical properties in polymer:fullerene blends the reader is referred to a detailed study published recently together with our collaborators [172].

5.10 Assignment of reduced CT exciton recombination loss in doped films to phase space filling

Considering the density of states (DOS) of conjugated polymers, which is broadened by disorder in amorphous films, doping is known to fill the states at low energy in the tail of the DOS [10]. To confirm that the charge carriers fill the states of PCPDTBT, we looked at the high energy side of the PL spectrum, since the lowest energy part of the DOS will be blocked for holes constituting Frenkel excitons. By this, the energy gap will be shifted to higher energies and any emission should be blue-shifted. Because of the undetectable PL from PCPDTBT in blends we show in Figure 5.14 the spectra of pure PCPDTBT films doped by different amounts of F_4TCNQ.

The PL peak position, representing the recombination of Frenkel excitons, is shifted toward higher energies by 24 meV and 40 meV for the 2 and 5% doped sample, respectively. This indicates phase space-filling of low-energy, immobile states in the polymer HOMO and consequently blocking of these states (Figure 5.14, inset). We interpret these states in PCPDTBT to be likely responsible for being sites where CT excitons are formed and recombine. A possible interpretation of our observations is that doped polymer domains do not support the formation of CT excitons resulting in a more favourable formation of polarons. The increased separation of polarons might be further attributed to a higher average mobility of holes in the polymer HOMO, since the low-energy, immobile states are blocked by doping. Accordingly, photo-generated holes will occupy energy levels with a higher DOS, providing more available states for hopping transport. Because of the disordered nature of conjugated polymers, doping acts in an inhomogeneous way leaving some domains unaffected. Those are likely to exhibit the observed residual CT exciton emission.

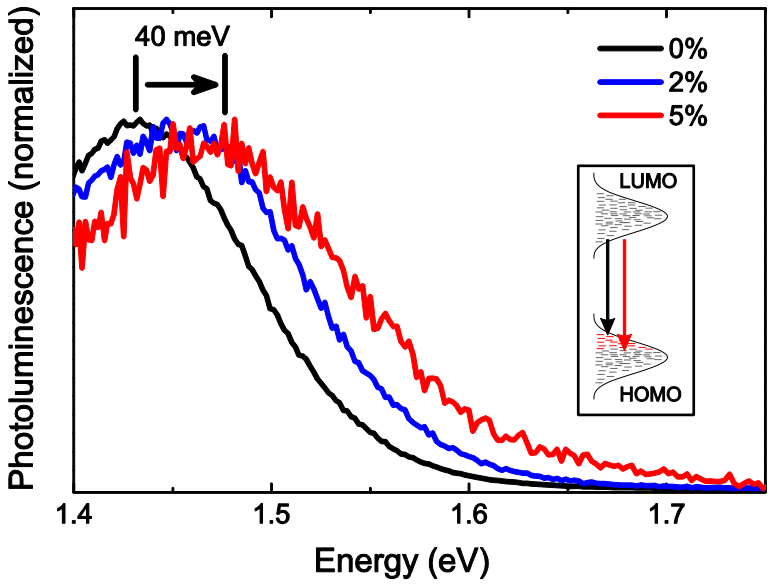

Figure 5.14 Photoluminescence spectra of PCPDTBT, doped at different amounts with F_4TCNQ, normalized at the emission peak. Excitation at 3.1 eV. The arrow indicates the peak shift of 40 meV upon doping 5% per polymer weight. The inset gives a schematic representation of the HOMO and LUMO levels of PCPDTBT. The states marked in red indicate blocked states by p-doping. The vertical black arrow indicates emission transitions for the undoped case, while the red arrow refers to the doped case.

It has recently been discussed in how far "hot" CT excitons play a role in charge separation [75]. CT excitons are termed "hot" when they have not yet thermally relaxed after excitation, but reside in excited electronic or vibrational levels above the CT exciton ground level. From the presented experiments the role of hot CT excitons cannot be finally answered, since these excitons are not directly observable in our experiments. However, since we do not observe a change in the lifetime of the CT excitons upon doping, any hot CT processes have to take place before relaxation to the recombining CT excitons detected in our transient PL. A change in lifetime would indicate the opening of another decay channel, e.g. separation into free charges from the relaxed CT exciton. Still, we observe an increase in polaron yield. This indicates that by filling the low-mobile tail states in the polymer HOMO by doping, a higher number hot CT excitons might be formed. These are more prone to dissociate into free charges than to relax to emissive CT excitons. In the outlook in Chapter 7 we discuss possible future experiments to study these hot CT excitons.

5.11 Conclusion

We enhanced the charge carrier generation in PCPDTBT:PCBM blends by using chemical doping to change the electronic properties of the system. We employed transient PL to investigate the effect of doping on the radiative recombination of electron-hole pairs localized at conjugated polymer–fullerene interfaces (CT excitons). Additionally, we used transient PIA measurements to probe the polaron formation and recombination. We demonstrated that a low concentration of p-type dopant molecules (< 4% weight) reduces the interfacial recombination via CT excitons and results in a favoured formation of separated charge carriers. This was observed by an ultrafast quenching of the CT exciton PL and an increase in photo-induced polaron density by up to 70%. Results for doped prototype solar cells demonstrated an increase in open-circuit current, in line with the spectroscopically observed higher polaron yield. The results are consistent with a reduced formation of emissive CT excitons, induced by state filling of the low-energy, immobile tail states in the polymer HOMO density of states. This work shows that doping-induced state-filling influences the charge separation process and offers a new interesting method to improve charge generation in organic photovoltaics.

6 Effect of oxygen doping induced degradation on exciton dynamics and charge separation in P3HT:PCBM blends

In this chapter, we describe the influence of oxygen doping induced degradation on the fundamental photo-physical processes in P3HT:PCBM blends. Samples are systematically aged by exposure to AM 1.5 illumination in the presence of dry air. The amount of degradation is quantified by the relative absorption loss of P3HT and is used to label the different investigated samples in the range from 0 to 20% degradation. Steady-state PL spectra show an increasing loss in the number of excitons within P3HT domains as a function of degradation. This loss already occurs within the first 15 ps after photo-excitation, as revealed by transient photo-induced absorption (PIA) spectroscopy of the exciton population. With the same technique we detect a more pronounced, degradation-induced, decrease in polaron population compared to excitons. This polaron loss occurs on a picoseconds time scale. Notably, the steady-state PIA of degraded samples exhibits a signal ascribed to triplet excitons, which is absent for undegraded samples. We attribute this to an oxygen doping induced disruption of the pristine blend morphology. The investigation of polaron and exciton population dynamics on a timescale from femtoseconds to one nanosecond, unravel two primary loss mechanisms on the performance of degraded P3HT:PCBM solar cells: The first process is an initial ultrafast decrease in the polaron generation, unrelated to exciton diffusion to the polymer:fullerene interface. The second, less pronounced, effect is a loss in the exciton population within the photo-excited P3HT domains. By quantifying the loss mechanisms with a coupled rate equation model, we provide a complete overview of the degradation effects on the photo-physics in P3HT:PCBM blends. In addition, we report solar cells fabricated from degraded blends and compare our spectroscopic findings with power conversion efficiency measurements.

6.1 Motivation to study oxygen doping induced degradation processes

Organic solar cells continue to attract large interest because of their potential for simple processing, light weight applications and low production costs [25]. During recent years the power conversion efficiencies of both, single-junction and tandem-cell devices, have improved significantly [127,212]. Recent reports show photovoltaic efficiencies above 8% from a combination of low bandgap donor-acceptor copolymers and a fullerene derivative [122,127,213]. A topic, which is just as important for commercialization, but has not been investigated in detail, is the long-term device stability. One major issue concerns the diffusion of oxygen into the active layer under ambient conditions[214–217]. The concomitant reactions of oxygen with the organic semiconductor[218,219] leads to a loss in device performance[220–222] and is termed degradation. Indeed, estimations on the costs of production and cells lifetime indicate that organic photovoltaics can become competitive with other technologies, if module lifetimes between 5 and 10 years are reached [25,223]. So far, studies on the long term stability and the degradation of solar cells have been mainly focussed on the complete devices[221,222,224–227]. While those are of primary importance, it is not always possible to distinguish between the degradation of the active layer, the interface with the electrodes, or the contacts [228,229]. In devices with regular structure the corrosion of the low workfunction electrodes usually limits the lifetime [227], while for cells of inverted structure the degradation under illumination in dry air affects mainly the active layer. The degradation effects consist of a reversible part, which is assigned to oxygen induced chemical doping, and an irreversible part which is due to p-doping and photo-oxidation of the polymer [230]. In our work we investigate the irreversible effects of degradation on the photovoltaic processes in the active layer, each of which might be adversely influenced.

There are several physical processes contributing to photocurrent generation in a typical polymer:fullerene solar cell. First, bound electron-hole pairs are created upon light absorption. This process primarily takes place in the conjugated polymer, due to the high absorption cross-section of optical transitions in these materials. On the other hand, in common fullerene derivatives these transitions are typically forbidden and, thus, weak[153,157,231]. The electron-hole pairs form excitons that diffuse through the material, with the vast majority reaching the heterojunction, before recombining [80,208]. Electron transfer takes place, provided that an optimal bulk heterojunction morphology is

present [22,232,233]. This either leads to the separation of charge carriers or to the formation of interfacial CT excitons, which can recombine radiatively [90,101,103,111]. Separated positive and negative charge carriers (polarons) then move towards the electrodes within the polymer and fullerene domains, respectively. The photocurrent is the result of polaron drift and extraction at the electrodes. So far, the contribution of each of these processes in limiting the performance of degraded devices has not been clarified yet. In other words, it is not clear whether excitons, polarons or the CT excitons are mainly affected by degradation and to which extent. The degradation of the polymer:fullerene active layer, occurring upon extended illumination in atmosphere, can in principle impact each of the physical processes described above. For example, exciton recombination via dark states could be accelerated. This would negatively influence the total amount of polaron pairs, which are supposed to be generated at the heterojunction. Moreover, polarons might be trapped at degradation sites and their recombination rate could increase. This effect is explained by the loss in the average carrier mobility, which is known to accelerate recombination [144,234].

6.2 Controlled oxygen doping of polymer-fullerene blends

P3HT with a regio-regularity higher than 90% was provided by Merck. PCBM(60) was purchased from Solenne and used as received. For all the blends (1:0.8 weight ratio), solutions of the polymer and fullerene were prepared in spectroscopic grade o-xylene. Thin films of the blends were obtained by doctor-blading on pre-cleaned glass substrates in inert atmosphere. Prior to degradation, the films were annealed at 140 °C in the glovebox for 2 min. Subsequently, the samples were exposed to oxygen in dry synthetic air and illuminated with the full spectrum of a sun simulator (AM1.5 solar spectrum) until the desired amount of degradation was achieved. The duration, until the final degradation level was reached, was in the order of a few hours. Before performing spectroscopy on the degraded samples, they were brought back into the glove box and encapsulated. For this a glass plate was put on top of the film and the edges were sealed with gas-tight epoxy resin (Torrseal®). In order to remove any reversibly bound oxygen from the films, the samples were annealed in the glovebox at 130 °C for 10 min prior to encapsulation. The encapsulation under inert conditions prevents any further exposure to oxygen that might lead to changes in the samples' properties. This allowed us to use the same set of samples for all the presented experiments.

Figure 6.1 shows the absorption spectra of four P3HT:PCBM blends with different exposure time to oxygen (dry air) and AM1.5 solar simulator illumination at room temperature. All spectra show the typical absorption features of annealed P3HT:PCBM blends in the visible and ultraviolet (UV) [138]. The absorption band from 400 nm to 700 nm is due to P3HT. In particular, the absorption shoulder around 600 nm represents the crystalline phase of P3HT, indicating the presence of highly ordered P3HT domains in the blend. PCBM shows a strong absorption in the UV below 350 nm and has only a weak absorption tail extending into the visible [153]. While the P3HT absorption band is monotonically decreasing with exposure time, the absorption of PCBM, which is more pronounced in the UV below 350 nm, is less affected.

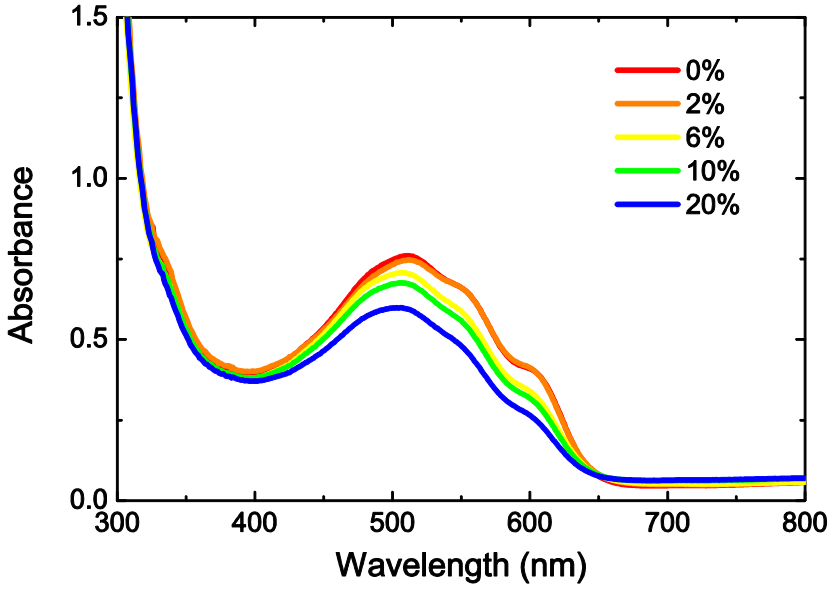

Figure 6.1 Absorption spectra of P3HT:PCBM blends subjected to different ageing periods under oxygen (dry synthetic air) and AM1.5 solar illumination. The spectra show a homogeneous loss in the absorption range of P3HT (400 nm – 650 nm) while the PCBM absorption is less affected (<400 nm). The relative loss in absorption (in %) at 500 nm is used to label the degradation of the samples, as stated in the legend.

This observation suggests that PCBM is less severely influenced by degradation and less prone to suffer from oxygen doping, compared to P3HT. Remarkably, the decrease in the absorption spectrum of P3HT is wavelength independent, i.e. all spectra have similar shapes, and only a very weak feature on the red onset of the absorption is noticed after relative subtraction of the spectra. This feature can be considered as an indication for the formation of a charge transfer complex between P3HT and oxygen [219]

or some degradation product [235]. According to the results of Reese *et al.* [236], the short ageing periods used in our study exclude changes to the initial morphology after preparation of the blends. The relative loss of the absorption (in %) at 500 nm is used in the following to classify the samples, where 0% corresponds to the undegraded sample.

6.3 Observation of degradation-induced exciton population loss in steady state photoluminescence

We use photoluminescence (PL) spectroscopy as a suitable tool to study the effect of degradation on the photo-generated singlet Frenkel excitons in the polymer-fullerene blend. Figure 6.2 shows the PL spectra of blends at the same degradation stages as shown in the previous paragraph. The spectrum is dominated by the characteristic P3HT emission [137] and the PL intensity decreases monotonically with degradation. The inset in Figure 6.2 shows normalized PL spectra.

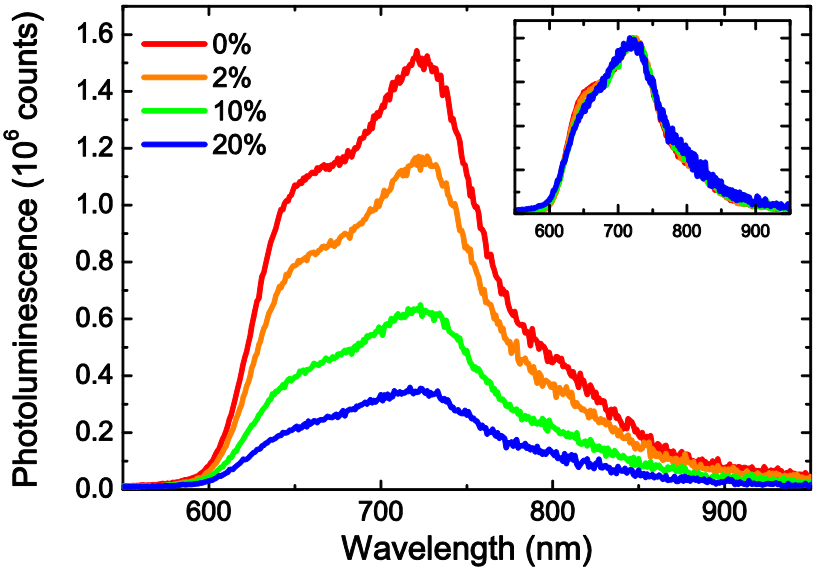

Figure 6.2 Photoluminescence spectra of P3HT:PCBM blends at different degradation stages. Excitation wavelength was 500 nm. The inset shows the normalized photoluminescence spectra. A monotonous quenching of the emission with increasing degradation is observed. The shape of the spectra changes only slightly in the region of the crystalline P3HT domains, as shown in the inset.

Interestingly, the shoulder around 650 nm which is representative for crystalline domains in P3HT is more strongly quenched than other regions of the spectrum. This

might indicate a break-up of the crystallinity, resulting from oxygen diffusion into these domains. On the other hand the presence of oxygen is known to quench PL. Therefore, a further explanation of the PL quenching might be a stronger accumulation of oxygen molecules in the crystalline, compared to the amorphous domains, leading to a stronger PL quenching in the crystalline domains. However, this is only a minor effect. Further insights on the PL quenching mechanism can be gained from the quantitative loss in emission intensity. In Figure 6.3 we report the ratio between the integrated P3HT PL of the undegraded blend, PL(0%), and the degraded samples, PL(x%), where x indicates the relative level of ageing according to Figure 6.1. The values are plotted versus the relative change in absorption which is a measure for the oxygen doping of the sample [237]. The integrated PL is evaluated after rescaling for the amount of photons absorbed at the excitation wavelength of 500 nm.

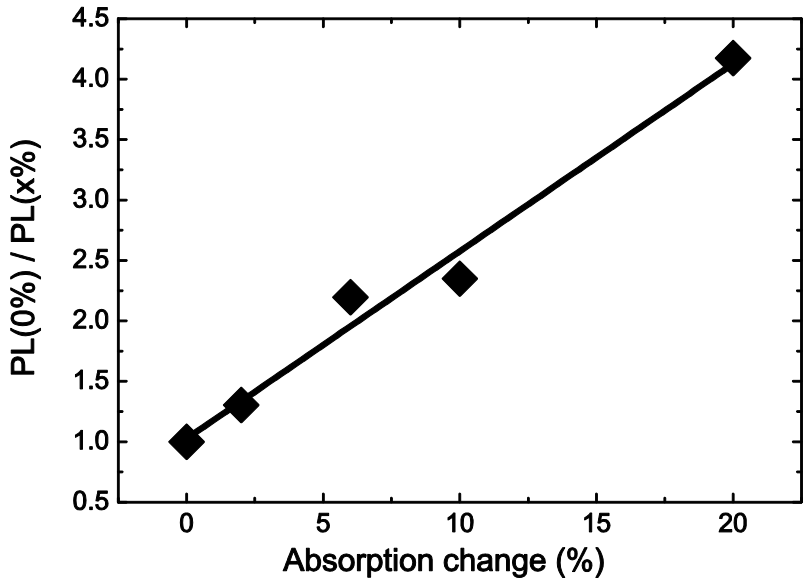

Figure 6.3 Ratio between the integrated PL of the undegraded sample [PL(0%)] and degraded samples [PL(x%)], plotted against the degradation ratio as determined from absorption measurements. The drawn line represents a linear fit to the data. The linear relation indicates a Stern-Volmer type of quenching.

We evaluate the data on the basis of a Stern-Vollmer relationship. The data indicate a linear relation, typical of a Stern-Volmer type of quenching [65]. The Stern-Vollmer relationship describes the quenching of an excited molecule in the presence of a quencher species according to the formula:

$$\frac{I_0}{I} = 1 + k \cdot [Q] \qquad (6\text{-}1)$$

In this equation I_0 stands for the PL intensity without quenchers, while I describe the intensity in the presence of quenchers with concentration $[Q]$. k is the Stern-Vollmer constant.

The Stern-Volmer behaviour indicates that excitons, diffusing in polymer domains, encounter quenching sites, whose number increases linearly with the amount of oxygen doping. It has been found in previous publications that the amount of degradation increases with exposure time to oxygen and illumination [214,237,238]. This suggests that blend films exposed to illumination in air for longer time intervals have a higher concentration of quenching sites, generated by the photo-oxidation process. We assign those sites to be dark, since we were unable to detect significant differences in the shape of the PL spectra in the visible and near infrared up to 1400 nm. Summarizing the information extracted from PL experiments, photo-generated excitons in P3HT can decay non-radiatively as a consequence of interaction with dark species produced in the degradation process. Some excitons might also be quenched by charge carriers, which are either a result of the ground state CT complex [219] formed with O_2 or originating from degradation radical reactions [239] as shown in previous publications. For excitons in P3HT these processes represent loss channels competing with diffusion to the heterojunction interface and charge separation.

6.4 Reduced initial polaron and exciton populations with faster recombination dynamics

The PL data of Figure 6.2 provide valuable information on the quenching of P3HT excitons by degradation, but do not offer a probe for the charge generation. This process takes place at the interface (heterojunction) with PCBM and gives rise to the formation of polarons, responsible for the photocurrent. An experimental technique, which gives unique insights into the population dynamics of excitons and polarons, is photo-induced absorption (PIA) spectroscopy. We first comment on the different signals obtained in PIA experiments in steady-state conditions and then focus on the dynamics on a picosecond time scale.

Figure 6.4 shows the steady-state PIA of samples at different degradation stages. In PIA experiments the relative change in transmission ΔT/T through the blend film, induced by photo-excited states, is measured. The states are induced by a cw-laser tuned to 532 nm. Positive signals (note the –ΔT/T in our scale) indicate an increase in the transmitted probe light and can originate from ground state bleaching (GSB) or stimulated emission (SE). Negative signals are due to a decrease in the transmitted light and originate from absorption of excitons towards higher excited states or from absorption of polarons.

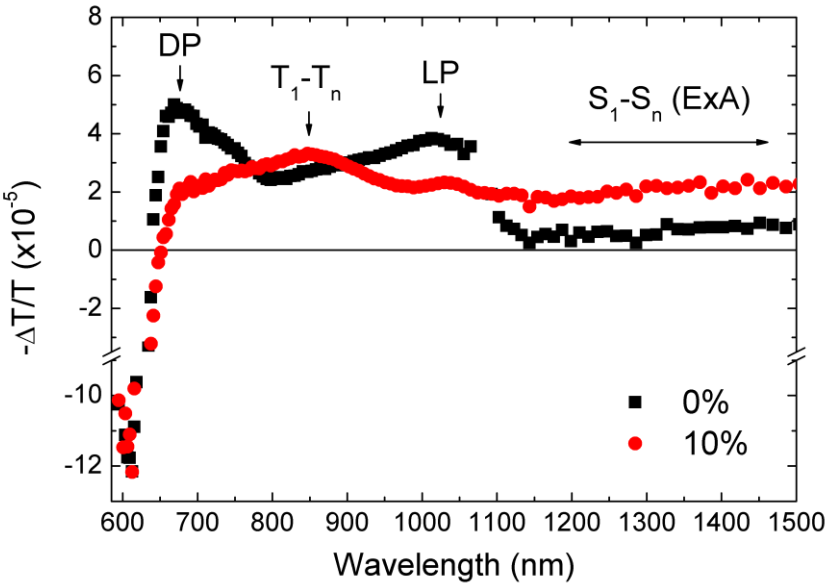

Figure 6.4 Steady-state PIA of P3HT:PCBM blends at 0 and 10% degradation measured with excitation at 532 nm. Spectra normalized to the ground state bleach (GSB) at 600 nm to obtain comparable excitation densities. Note the break in the ΔT/T axis. Undegraded blends show GSB below 650 nm and polaron signals between 650 nm and 1050 nm. In degraded samples the polaron signal intensities are reduced and a new band at 850 nm rises, which was assigned to triplets previously. Image adapted from Deschler *et al.* [240], measurement by Dr. A. De Sio at Carl von Ossietzky Universität, Oldenburg.

The steady-state PIA spectrum of P3HT:PCBM is dominated by the optical transition of species in P3HT, which have been previously studied and interpreted [211]. The band at 670 nm has been assigned to a signature of delocalized polarons (DP), meaning polarons delocalized over two or more polymeric chains, while the weak signal above 1100 nm is due to transitions from the first excitonic state (S_1) to higher exciton states (S_n) [26,211]. We term these last transitions "exciton absorption" (ExA). The ExA absorption is expected to be weak in a steady-state experiment, because of the short

lived nature of excitons in a polymer fullerene blend. This signal represents a measure for the exciton population in the blends. Previous publications have shown that ExA transitions extend up to 1600nm [159]. Peaks at 850 nm are due to triplet exciton absorption ($T_1 \rightarrow T_n$) and features around 1000 nm originate from localized polarons (LP) with intrachain character [241].

We note that there is a decrease in the amplitude of the DP signal upon ageing, indicating that degradation has an influence on the population of polarons, which are fundamental for photovoltaic action. While the 0% sample (black curve) has only two prominent bands at 670 nm (DP) and ~1000 nm (LP), both due to polarons, the 10% sample exhibits a signal at 850 nm, which we assign to triplet exciton absorption (TrA). This excited state transition is usually not observed in regioregular P3HT in blends with PCBM, since the relatively high yield of polaron formation in the excited state competes with intersystem crossing and population of the triplet state [208]. However, PIA measurements on regio-random P3HT, where polymer chains are more disordered and polaron generation is less probable [103,159], indicate the presence of a band at 850 nm with spin-1 characteristics, i.e. a triplet [211,242]. The formation of a triplet band in degraded blends therefore indicates more disordered films with an increased number of sites where intersystem crossing can occur. We attribute this to oxygen diffusion into the blend films and concomitant breaking of the pristine blend morphology. We note little changes in the ExA spectral range among the different samples. However, due to the short lived nature of singlet excitons in P3HT:PCBM those are almost undetectable in steady-state experiments as the one shown in Figure 6.4. We address this point in a more quantitative manner below, by analysing the ExA signal in transient absorption. Furthermore, the measurements of ExA transitions on a picosecond time scale, within the lifetime of the excitons, allow for a detection of the short-lived exciton states.

In order to probe the exciton population dynamics (ExA), we performed femtosecond transient absorption spectroscopy by exciting the sample with 200 fs short pulses centred at 550 nm and recording the change in transmission of time delayed pulses at 1500 nm. This probe wavelength allows us to observe the decay of ExA, in a spectral region without the interfering contribution of P3HT polarons [159]. However, we have removed a small, long-living constant background, likely caused by a weak polaron signal from PCBM, since its anion is expected to absorb in this region[243]. All measurements were corrected for differences in absorption at the excitation wavelength of 550 nm.

Figure 6.5a shows the ΔT/T transients probing the ExA at 1500 nm for blends of different degradation level (0%, 10%, 20%). For all samples the signal sets in within the setup's time resolution of ~250 fs, but shows different amplitudes at zero time delay for degraded samples (10%, green curve / 20%, blue curve) compared to the undegraded blend (0%, red curve). This indicates that in degraded samples part of the initial hot excitons are lost within the first 250 fs. Looking at the ExA decay in the first picoseconds after exciton thermalization (Figure 6.5a), we note that degradation leads to faster recombination and shorter lifetimes. In the first picoseconds after excitation typically the exciton diffusion process is observed. Faster dynamics on this time scale suggest that exciton quenching during the diffusion process contributes to the loss in the overall exciton population as well.

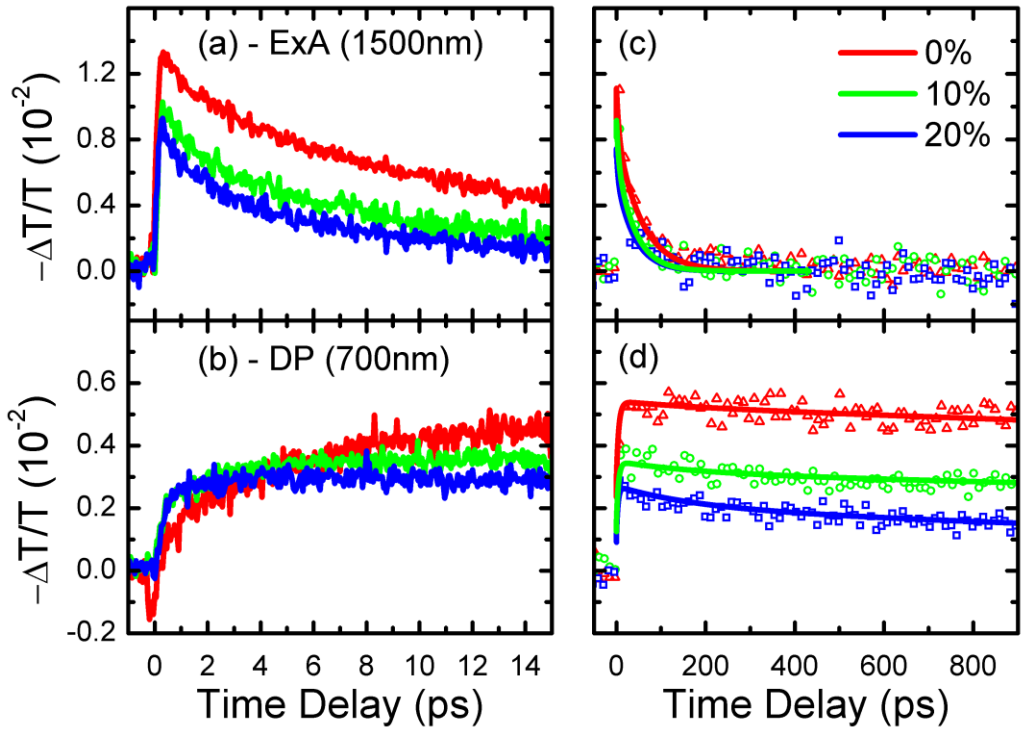

Figure 6.5 Transient absorption decays for P3HT:PCBM blends with the probe centred in the absorption bands of excited singlet state (ExA, 1500 nm) and delocalized polaron (DP, 700 nm), respectively. In (a,b) transient rise and decays are shown on a short time scale (0-15 ps). In (c,d) transient decays are shown on a long time scale (0-900 ps) for ExA and DP, respectively. Symbols in (c,d) are data points whereas the solid lines represent fits according to the rate equation model described in the text. Excitation performed at 550 nm with fluences <10μJ/cm2. The transients have been rescaled for the amount of photons absorbed, i.e. 1-10^(-OD) at the exciting wavelength.

It is interesting to compare these decays with the dynamics of the delocalized polarons (DP), which are supposed to be representative for the carriers contributing to photocurrent in the solar cell [159]. In Figure 6.5b we report the transient dynamics of DPs probed at 700 nm. The undegraded sample at zero time delay shows an ultrafast negative feature (positive on a +ΔT/T scale) slightly longer than the duration of the pump pulses. It evolves into a positive signal with a rather long rise time, reaching a maximum at about 40 ps. In the degraded samples (Figure 6.5b, green/blue curve) the rise in DP is faster and the initial negative feature is absent. Further, the overall amount of DP is smaller compared to the undegraded samples as the signals saturate at $-\frac{\Delta T}{T} =$ $0.52 \cdot 10^{-2}$, $0.35 \cdot 10^{-2}$ and $0.29 \cdot 10^{-2}$ for the 0, 10 and 20%, respectively. So far the rise of the DP signal has been interpreted as the generation of free polarons from excitons diffusing to the heterojunction or from charge transfer excitons [139,244]. However, as seen from the transients of the undegraded blend in Figure 6.5(a,b), the *rise* in DP correlates with the *decay* of excitons (ExA). In contrast to previous assignments we propose, that the generation of DPs is not subjected to a rise, but that the ΔT/T signal in this spectral region is rather superimposed by a short lived stimulated emission (SE) feature [80]. The SE dynamics resemble the ones of ExA (Figure 6.5a), since they originate from the same species, i.e. excitons in the P3HT domains. Small differences in the dynamics are observed, since SE originates only from excitons diffusing and recombining in the P3HT domains. On the other hand, ExA considers all excitons photo-generated in P3HT, i.e. those recombining, getting trapped or separating to form polarons at the heterojunction. Further, the loss of excitons at time zero seen in the ExA transients (Figure 6.5a) is reflected in the loss of the negative SE signal for the 10 and 20% degraded samples in Figure 6.5b. For the 20% sample the rise of the DP signal is instantaneous and therefore uncorrelated to a diffusion of excitons towards the interface within several picoseconds. If the rise in DP were due to the splitting of excitons after diffusion to the polymer:fullerene interface, the faster decay of ExA would mean a faster, thus more efficient, generation of polarons. Such an effect is not observed, since the DP amplitude decreases. In conclusion we assign the negative feature and rise detected in the DP signal of undegraded blends to SE from diffusing excitons. This interpretation is in agreement with recent experimental studies by infrared femtosecond PIA spectroscopy, where polarons can be selectively probed in the absence of superimposed stimulated emission contributions and appear without any rise on a

picoseconds time scale [80,95]. Further insights can be gained from the relative loss of exciton (ExA) and polaron (DP) population in degraded samples. The relative loss is obtained by comparing the maximum ΔT/T, taken at zero time delay, for degraded and undegraded samples. For the 10% degraded sample, we find a loss in exciton population of 24% compared to the undegraded sample, while the polaron population is reduced by 33%. For the 20% sample, the initial loss in excitons is 31%, whereas the loss in DPs amounts to 45%. The loss in DP compared to the loss in exciton population is therefore more pronounced in all degraded samples. This indicates a more pronounced degradation effect at the polymer:fullerene interface where charge generation occurs. Further, a substantial amount of polarons is generated immediately after excitation and not as a consequence of exciton diffusion to the interface.

To investigate the effect of oxygen doping on recombination dynamics on a longer time scale, we investigated the transient absorption of ExA and DP up to 1 ns (Figure 6.5(c,d)). The ExA signal for pristine and degraded blends (Figure 6.5c) decays to zero within the first 200 ps, indicating short-lived excitons. This correlates with the efficient splitting of initially excited excitons into separated charges at the heterojunction. A shorter exciton lifetime is observed for increasing degradation, as already indicated from the experiments probing the first tens of picoseconds (Figure 6.5a). On the other hand, the DP transient of the undegraded sample, (Figure 6.5d, red curve), does not exhibit a decay on a time scale of 1 ns in accordance with previous studies on undegraded P3HT:PCBM blends [80,159]. These studies show the long-lived nature of DPs, which need to be extracted from the active layer and contribute to the photocurrent for efficient solar cell performance. In contrast to the undegraded blend, the DP signal of the 10 and 20% degraded samples exhibits an initial decay on the hundreds of picoseconds time scale. This indicates that the products resulting from photo-oxidation influence the polaron dynamics on a nanosecond time scale and evidently lead to accelerated recombination. The reduced polaron lifetime in degraded samples hinders charge extraction and is detrimental for efficient solar cell performance. In the next paragraph the underlying processes will be quantified, employing a rate equation model. Summarizing, degraded blends show reduced exciton as well polaron populations compared to undegraded samples within the setup time resolution of 250 fs. We stress that relative losses in exciton and polaron populations are not identical upon ageing of

the blend. The loss in polarons is more severe with faster polaron recombination rates for increasing degradation.

6.5 Quantification of loss processes with rate equation model

In order to obtain a quantitative estimation of the trapping rates induced by degradation products, we have modelled the transient absorption curves with a system of coupled rate equations. Figure 6.6 gives a schematic overview of the transitions described in the rate equation model. First, we have considered the initial amount of hot excitons [HEx], induced by the pump laser pulse. Excitons are termed "hot" when they have not yet thermally relaxed after excitation, but reside in excited electronic or vibrational levels above the exciton ground state. The [HEx] are branching into four different populations. These are the recombining excitons [Exr], the diffusing excitons [Exd], free polarons [Polf] and trapped excitons [Ext] according to the rate equation

$$\frac{\mathrm{d}\,[\mathrm{HEx}]}{\mathrm{dt}} = -\frac{[\mathrm{HEx}]}{\tau_{\mathrm{HEx-Polf}}} - \frac{[\mathrm{HEx}]}{\tau_{\mathrm{HEx-Exd}}} - \frac{[\mathrm{HEx}]}{\tau_{\mathrm{HEx-Exr}}} - \frac{[\mathrm{HEx}]}{\tau_{\mathrm{HEx-Ext}}} \qquad \textbf{(}6\text{-}2\textbf{)}$$

The initial ultrafast partition or branching of HEx is a necessary step to describe the decrease in the signal of ExA and DP at zero time delay. This approach is consistent with the experimental reports that excitons diffusing to the heterojunction are not the exclusive source of polarons in P3HT:PCBM blends. It has been shown that polarons can form quasi-instantaneously [80,95] from hot excitons. Equation **(**6-2**)** takes into consideration that a portion of the initial [HEx] is generated in P3HT close enough to the heterojunction interface to diffuse and reach PCBM, those constitute the diffusing excitons, [Exd]. Some other [HEx] within the P3HT domains and far from the interface are just recombining, [Exr], or are trapped to dark states because of degradation products, [Ext]. The first term on the right hand side of eq. **(**6-2**)** takes into account the direct formation of polarons from the [Hex] as evidenced from the experiments in reference [80]. The time constants, or inverse probabilities, for the generation of free polarons ($\tau_{\mathrm{HEx-Polf}}$), diffusing excitons ($\tau_{\mathrm{HEx-Exd}}$), recombining and trapped excitons ($\tau_{\mathrm{HEx-Exr}}$) and ($\tau_{\mathrm{HEx-Ext}}$), respectively, determine the initial branching ratios in Equation **(**6-2**)**.

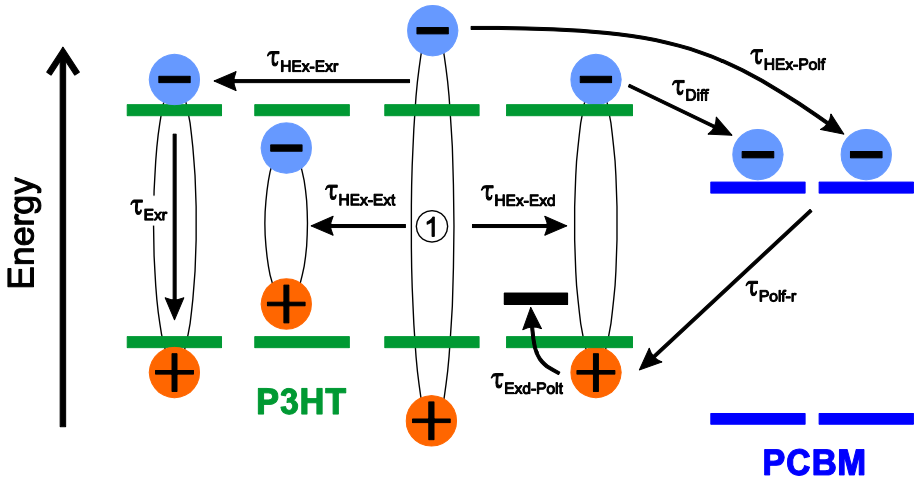

Figure 6.6 Energy scheme for the HOMO and LUMO levels of P3HT and PCBM together with the main transitions used in the rate equation model. The initial population of hot excitons [Hex] is marked (1).

We have described the transient signal of ExA considering two contributions originating from diffusing excitons

$$\frac{d[Exd]}{dt} = \frac{[HEx]}{\tau_{HEx-Exd}} - \frac{[Exd]}{\tau_{Diff}} - \frac{[Exd]}{\tau_{Exd-Polt}} \qquad (6\text{-}3)$$

and recombining excitons

$$\frac{d[Exr]}{dt} = \frac{[HEx]}{\tau_{HEx-Exr}} - \frac{[Exr]}{\tau_{Exr}}. \qquad (6\text{-}4)$$

Both populations are fed by [HEx], with the respective branching probabilities set by $\tau_{HEx-Exd}$ and $\tau_{HEx-Exr}$. The excitons in Equation **(**6-3**)** are influenced by diffusion to the heterojunction, τ_{Diff}, or formation of trapped polarons, $\tau_{Exd-Polt}$. On the other hand, the excitons in Equation **(**6-4**)** recombine with the lifetime τ_{Exr}.

To model the transient DP absorption signal, we used two contributions originating from free and trapped polarons, [Polf] and [Polt], which are described by

$$\frac{d[Polf]}{dt} = \frac{[HEx]}{\tau_{HEx-Polf}} + \frac{[Exd]}{\tau_{Diff}} - \frac{[Polf]}{\tau_{Polf-r}} \qquad (6\text{-}5)$$

$$\frac{d[Polt]}{dt} = \frac{[Exd]}{\tau_{Exd-Polt}} - \frac{[Polt]}{\tau_{Polt-r}} \qquad (6\text{-}6)$$

The lifetimes $\tau_{\mathrm{Polf-r}}$ and $\tau_{\mathrm{Polt-r}}$ describe the recombination time for free and trapped polarons, respectively. The modelling with two polaron populations was necessary to consider the bi-exponential decay of Figure 6.5d for the degraded samples.

From fitting the transient absorption of ExA and DP in the undegraded sample, we obtained $\tau_{\mathrm{HEx-Exd}} = 300\ fs$ and $\tau_{\mathrm{HEx-Exr}} = 100\ fs$ in Equation **(**6-2**)**. These rates are consistent with the typical thermalization times of excitons in conjugated polymers [63]. The values were then kept constant for the fitting of the degraded samples, since the rate constants of these processes are not affected by degradation. Hence, degradation-induced phenomena on [HEx] are described by variation of the rates of polaron formation $\tau_{\mathrm{HEx-Polf}}$ and trapping of hot excitons $\tau_{\mathrm{HEx-Ext}}$. In Equation **(**6-3**)** and **(**6-5**)** we set $\tau_{\mathrm{Diff}} = 6\ \mathrm{ps}$ and the rate of trapped polaron recombination $\tau_{\mathrm{Polt-r}} = 175\ \mathrm{ps}$. These values are kept constant, since the dynamics of these processes are assumed not to vary for different degradation extents. We took $\tau_{\mathrm{Exr}} = 50\ \mathrm{ps}$, as obtained from time resolved PL experiments. The six transient absorption decay curves for ExA and DP at 0, 10 and 20% degradation were then fitted adjusting the remaining four decay times. The simulated curves are shown as lines in Figure 6.5(c,d). The fittings accurately describe the transient curves for all samples both in amplitude and dynamics. First, we discuss the rates which were varied to reproduce the initial decrease in the amplitude of ExA and DP signals at time zero (Table 6.1). We notice that $1/\tau_{\mathrm{Hex-Ext}}$, which is the rate at which hot excitons turn into trapped excitons, is an important fitting parameter in our model. At 0% this rate can be taken as small as $(10\ \mathrm{ps})^{-1}$, since the other more probable processes in Equation **(**6-2**)** dominate. However, for increasing degradation levels it has to be set to substantially higher values up to $(100\ \mathrm{fs})^{-1}$.

Degradation ratio	$\tau_{\mathrm{Hex-Ext}}$ [fs]	$\tau_{\mathrm{Exd-Polt}}$ [ps]	$\tau_{\mathrm{Hex-Polf}}$ [fs]	$\tau_{\mathrm{Polf-r}}$ [ns]
0%	$10{\cdot}10^3$	100	300	10
10%	200	30	500	8
20%	100	10	600	3

Table 6.1 Time constants for the different photophysical processes described in Equations (6-2) to (6-6) of the rate equation model.

The initial decrease in DP signal is taken into account considering changes in $\tau_{\mathrm{HEx-Polf}}$ which has a lower probability $(1/600\ \mathrm{fs})^{-1}$ upon degradation, with respect to the 0%

sample $(1/300\ \mathrm{fs})^{-1}$. For the different decays, the faster dynamics of ExA on a picosecond time scale upon degradation are described by decreasing $\tau_{Exd-Polt}$. This rate is also used to generate the correct amount of trapped polarons to fit the DP curves. Our model is capable of reproducing the long decay time of DP, which is dominated by two lifetimes. Here, we have decreased the recombination time of free polarons, τ_{Polf-r}, from 10 ns in the 0% to 8 ns and 3 ns for the 10 and 20% samples, respectively, to fit the long decay, while the first decay component is fixed at 175 ps. It describes the recombination of trapped polarons. In summary, the coupled rate equation model allows us to fit the experimental data and quantify the rates of the degradation-induced loss processes.

From the spectroscopic results (Paragraph 6.4) and the coupled rate equation model (Paragraph 6.5), we can assign the main degradation-induced loss processes. In Figure 6.7 we give an overview of the different trapping and recombination mechanisms according to Table 6.1.

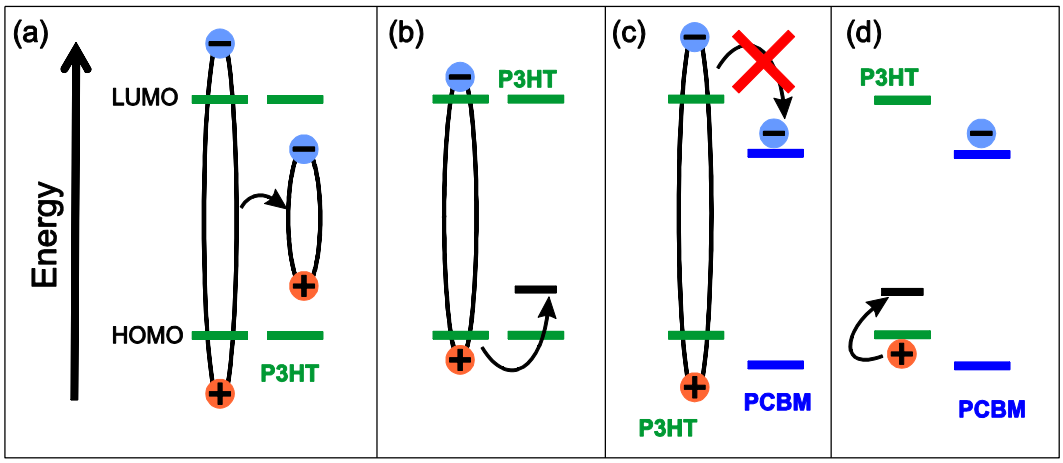

Figure 6.7 Energy schemes illustrating the main degradation processes occurring in aged P3HT:PCBM blends. (a) Hot exciton trapping in P3HT (b) Exciton splitting by degradation products to form trapped polarons in P3HT (c) Hindered charge transfer at the interface between P3HT and PCBM (d) Increased recombination of free polarons in P3HT. The processes illustrated here correspond to the lifetimes presented in Table 6.1.

We conclude that the ultrafast initial loss in ExA and DP is due to an increased probability to trap hot excitons and a decreased probability to form free polarons (Figure 6.7(a,c)). These two trends are summarized in the second and fourth columns of Table 6.1 and determine the major initial losses. The faster decays observed in Figure 6.5a for the ExA upon degradation are assigned to the generation of trapped polarons by

the diffusing excitons (Figure 6.7b). Finally, we attribute the faster decay in the DP signal of degraded samples to an increased population of trapped polarons and faster polaron recombination, which enters the nanosecond regime (Figure 6.7d). The initial ultrafast processes account for the major initial loss in exciton and polaron population, which are the critical species for the functioning of a solar cell. The long time scale of DP recombination is significantly compromised for extensive degradation treatments, as in the 20% sample. Here, the long lived polarons, which are contributing to the photocurrent, show a bi-exponential decay with lifetimes of 8 and 3 ns. We suggest that these shorter lifetimes are detrimental for efficient charge extraction. To examine this prediction we have fabricated and measured solar cells from P3HT:PCBM blends following the same ageing procedure as in the spectroscopic studies.

6.6 Effect of degradation on device performance

In order to quantify the effect of degradation on the device performance, the current-voltage characteristics of P3HT:PCBM cells with inverted structure are measured for different degradation ratios (Figure 6.8). Via absorption measurements the extent of degradation was determined. To allow for measurements of absorption spectra on complete device structures, the solar cell top electrode is designed as a grid finger structure on top of a highly conductive PEDOT:PSS layer.This way, it is possible to transmit light through the whole device and the absorption spectrum can be collected. Figure 6.8 shows the current voltage characteristics of three photovoltaic cells, degraded 0, 2 and 5%. An absorption loss of the active layer by 5% results in the reduction of device power conversion efficiency from η=3.2% to about η=0.3%. Longer ageing periods, corresponding to a 10% degraded sample, resulted in the total absence of photovoltaic response in the cells. This observed loss in cell performance is mainly due to a decrease in the short circuit current, from 9.9 mA/cm^2 to 1.6 mA/cm^2. The loss in fill factor is less dramatic from FF = 0.59 to FF = 0.38. Interestingly, the open circuit voltage is not affected by degradation up to 5%. The 85% loss in J_{SC} for a device with just 5% absorption loss is therefore a combination of several factors: about 24% are due to the reduction of charge carrier formation (polarons) during the first 250 fs after the laser pulse, as determined from transient absorption measurements on a 5% degraded sample. We conclude that the remaining 61% of loss in extracted charge carriers are due to the loss in absorption (5%) and enhanced charge carrier recombination on the µs time

scale, not accessible in the present experiments. An additional possible loss channel is trapping in PCBM, which is not detectable in our experiments.

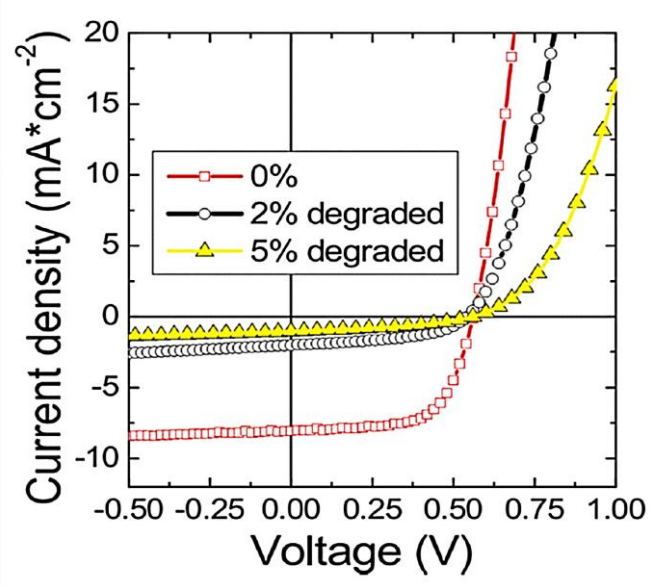

Figure 6.8 Current density vs. bias voltage measurements for P3HT:PCBM devices with inverted cell geometry under illumination with a solar simulator before (red squares) and after (yellow triangles and black circles) degradation under oxygen (dry synthetic air) and AM1.5 illumination. The extent of degradation corresponds to an absorption loss of the active layer by 2% (black circles) and 5% (yellow triangles). Image adapted from Deschler *et al.* [240], device fabricated and measured by T. Sauermann at Konarka Technologies.

6.7 Stronger effect of oxygen doping on polaron compared to exciton populations

This paragraph discusses the results of the spectroscopic and solar cell performance experiments on degraded blends. The analysis of our photo-physical data addresses the processes responsible for the degradation of performance in P3HT:PCBM solar cells. In particular, the data presented in Figure 6.5, together with the rate equation model in Paragraph 6.5, identify a faster trapping of initial hot excitons and a less probable formation of free polarons during exciton relaxation. Experimentally, the major losses are observed within the setup temporal resolution of about 250 fs, while excitons have not yet completely relaxed and are still "hot". This indicates a higher probability for hot excitons to be trapped by a degradation product. This observation can be rationalized, considering that hot excitons are more delocalized and in a coherent state. In this configuration they can sample a larger number of conjugated segments in the first few hundred femtoseconds and are more prone to encounter degradation products [245]. The

more significant loss in polarons, which results in the decrease of the maximum amplitude of the DP absorption signal, is a combined consequence of hot exciton trapping and a lower probability of free polaron formation. In undegraded systems, separated polarons are formed on an ultrafast time scale (<100 fs), involving P3HT chromophores close to the heterojunction interface. It is interesting that degradation of the polymer domains, which is demonstrated by our absorption and PL experiments (Figure 6.1 / Figure 6.2), is influencing the ultrafast charge generation process occurring primarily for chromophores close to the interface. We suggest that the degradation products, likely originating from photo-oxidation of the polymer, might be more concentrated at the heterojunction. In this region the P3HT chains are at the border of a semi-crystalline domain and oxygen can diffuse more easily into these areas compared to the crystalline core parts. The shorter lifetimes of ExA observed upon degradation have been modelled considering the formation of trapped polarons from diffusing excitons. While we did not observe clear indications for the build-up of a triplet population in the transient experiments, our steady state PIA indicates the presence of this species on a longer time scale. To explain these observations, we recall that regio-random P3HT shows signatures of triplets in PIA, while having the same chemical structure of P3HT [211]. An important difference between the regio-regular P3HT used here and the regio-random type is the conjugation length and the intrachain planarity, two effects which are known to affect the triplet yield [246]. On the basis of these arguments, we can discuss the increased triplet yield in degraded blends, considering that degradation products might disrupt the conjugation of the polymer or create carbonyl groups. As a result, intersystem crossing to the triplet manifold is enhanced [66]. The comparison between the losses in DP population and the J_{SC} of solar cells underlines that a large part of the photovoltaic performance drop is ascribed to an increase in the long time scale recombination of polarons (>10 ns). This might also involve charge trapping in PCBM. In this direction, the recent work by Reese *et al.* reports the presence of PCBM degradation products acting as effective traps for the transferred electrons [182].

6.8 Conclusion

We performed a photo-physical study on the fundamental processes concerning photovoltaic operation in P3HT:PCBM blends subjected to different extents of oxygen

doping. Illumination of oxygen doped samples leads to photo-oxidation, also termed degradation. The blend films were labelled according to the relative degradation-induced absorption losses. PL spectroscopy indicated a linearly increasing density of exciton quenching sites with degradation. Evaluation of exciton and polaron populations from transient PIA measurements allowed quantification of the degradation-induced losses. The fitting of the experimental results with a rate equation model allowed quantification of the individual loss channels. Our analysis indicated that exciton trapping takes place on a rate comparable to electron transfer to PCBM. Additionally, ageing has major consequences on the polaron population. The polaron generation is reduced with degradation and has to compete with the fast hot exciton trapping processes. Further, degradation reduces the lifetime of separated charge carriers which inhibits charge extraction from the active layer. Additionally our results suggested that the crystalline phase of P3HT domains is disrupted by migrating oxygen molecules. This leads to less efficient polaron formation and an increased triplet yield. Accordingly, prototype solar cells show a critical performance loss upon degradation. The experimental results assigned the lower cell efficiency to absorption losses, exciton trapping and reduced polaron formation. Our results have important implications on the understanding of degradation related phenomena in organic solar cells and on the modelling of device losses in aged photovoltaic devices.

7 Summary and Outlook

This thesis investigated the effects of small molecule doping on the charge separation process in conjugated polymer:fullerene heterojunctions. Depending on the type of dopant employed, improved or reduced charge generation was observed. The interaction of the dopant with the host material and the resulting changes in electronic and chemical properties determined the eventual result. The insights gained from these results offer new promising directions to improve solar cell performance.

In the first part of this thesis, we investigated the distribution of dopant molecules (F_4TCNQ) in conjugated polymers. We demonstrated, to our knowledge for the first time, that dopant distributions in thin polymer films can be mapped with low-voltage SEM. For different polymers, significant differences are observed in the doped film morphology. Aggregation and clustering of dopant molecules occurs above defined threshold doping ratios. We assign the differences in threshold values to differences in interaction between dopant and conjugated polymer.
With the presented general technique, the dopant distribution in various dopant-polymer systems can be studied. These future experiments will give further insights on dopant-polymer interaction and dopant-induced changes in polymer morphology. Further, SEM mapping of dopants might also be possible for the more ordered, small molecule organic semiconductors. Additionally, the increase in SEM contrast for organic semiconductor films, containing electron accepting dopants (p-doping), should also be observable using electron donating dopants (n-doping). Therefore, another interesting future experiment is the mapping of n-type dopants,e.g. cobaltocene.

Further, we have shown that p-doping of a low-bandgap polymer:fullerene blend with a small molecule electron acceptor (F_4TCNQ) results in reduced recombination through CT excitons. This effect causes an concomitantly improved photo-induced charge generation. We explain the observed effects by phase-space filling and blocking of low-energy, immobile trap states in the polymer HOMO. Prototype organic solar cells, using doped blends as the active layer, show an increase in short circuit current and cell efficiency. This highlights doping as a new method to improve solar cell performance.

However the photovoltaic system has not been optimized, since we wanted to keep it similar to the spectroscopic samples. In a first step, different compositions of the blend could be investigated, optimizing the dopant ratio and blend composition. Changes in blend composition affect the interfacial area, which is a critical parameter for the CT exciton formation. Previous publications have shown a significant dependence of CT exciton formation on the composition and morphology of the blend [53,103,247]. Therefore, a systematic study of the relation between blend morphology and the effect of doping has the potential for interesting findings. On the other hand, further conjugated polymers and different fullerene derivatives could be investigated in combination with F_4TCNQ. In principle, the general doping concept is expandable to many conjugated polymers, given that the HOMO level of the polymer matches the LUMO of the dopant molecule [11]. Further, other dopant molecules instead of F_4TCNQ could be investigated. However, the currently available selection of dopant molecules with suitable chemical and electronic properties is still quite limited. Many dopant molecules show an extremely high electron affinity (e.g. $SbCl_5$), which not only dopes the polymer, but also attacks the chemical bonds and destroys the polymer molecular structure. Therefore, these dopants are not suitable for long-term, stable doping. Tailored development of dopant molecules for the combination with specific organic semiconductors can further improve the positive effects of chemical p-doping on charge separation. Critical aspects in this respect are the electron affinity of the dopant molecules and the interaction of molecules with the polymer. Dopant clustering, as observed for P3HT in our studies, has to be avoided for efficient doping of the polymer.

Besides extending the doping strategy, also a further investigation on the fundamental properties of CT excitons can add to the understanding of the charge separation process. For this purpose, systems with a triplet state below the CT state are interesting, since the recombination of CT excitons via this channel is facilitated. Therefore, the time resolved phosphorescence from the triplet can give insights into the lifetime and diffusion behaviour of CT excitons. Another open question is the energetic structure of the CT exciton ensemble, since up to now mainly theoretical studies on the energetic levels of CT excitons at the interface between polymer and fullerene are published [108,109]. A possible experiment on these states involves the temporally and spectrally resolved photoluminescence of CT excitons. Such experiments can give insights on the energy structure and relaxation processes within the CT exciton

manifold as well as changes in CT exciton recombination lifetime with spectral position.

On the other hand, an adverse effect on charge separation was found upon oxygen doping of P3HT:PCBM blends. Oxygen exposure of the blends under illumination leads to photo-oxidation, also termed degradation. The aim of our work was to study the effect of degradation on the exciton and polaron populations in P3HT:PCBM blends. We observed reduced absorption and increased exciton quenching in the polymer domains after. Time resolved investigation of the charge generation process shows a lower initial yield of excitons and polarons, together with a reduced lifetime for both species.

One possible future direction is the use of regenerative anti-oxidants to neutralize oxygen molecules and prevent the interaction of oxygen with the conjugated polymer. This will evidently attenuate degradation effects. It is important to avoid interference of the anti-oxidants with the morphology of the polymer-fullerene blends, since the performance of organic solar cells depends critically on it [29,53,129,248,249]. On the other hand, the observation of a more severe effect of oxygen molecules at the interface between polymer and fullerene could be addressed with a more favourable morphology or geometry of solar cells. Preventing oxygen from reaching these critical heterojunction regions in the solar cell will reduce degradation effects. In this direction, the more applied route of encapsulating organic solar cells to prevent oxygen from diffusing into the device can be followed. However, in order to keep the special flexible properties of organic solar cells, also a flexible encapsulation has to be found.

Appendix A

One could generally expect that a similar SEM image contrast is observed in any polymer-acceptor system and not just in polymer-dopant blends. To exclude this assumption, we investigated a blend (1:1 weight) of PCPDTBT and the fullerene derivative PCBM with SEM. PCBM has a significantly lower electron affinity compared to F_4TCNQ and will therefore not act as a ground state dopant for the polymer. However, compared to PCPDTBT, PCBM has electron accepting properties and is used as electron acceptor in heterojunctions. SEM images of the polymer-fullerene film in Figure A.1 show an intermixed blend without fibres, indicating a dense mixture of the two materials. We note that the contrast between PCBM rich and PCPDTBT rich domains is almost negligible. This is in agreement with previous observations [53]. No comparable increase in SEM contrast as for polymer-dopant blends is detected. Thus, the increased contrast in doped polymers is not generally observed in polymer-electron acceptor blends. Therefore, we assign the increased contrast in SEM images of 10% doped PCPDTBT films to the special dopant properties of F_4TCNQ.

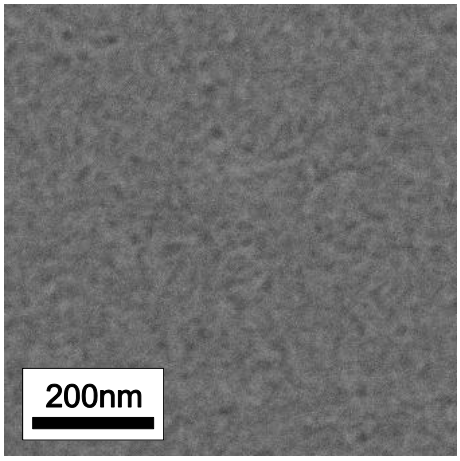

Figure A.1 Scanning electron microscopy image of a PCPDTBT:PCBM (1:1) blend. Acceleration voltage was 1 kV. The film shows an intermixed, homogeneous morphology without regions of increased contrast.

References

1. BP Statistical Review of World Energy June 2012. at <bp.com/statisticalreview>
2. McNeill, R., Siudak, R., Wardlaw, J. & Weiss, D. Electronic Conduction in Polymers. I. The Chemical Structure of Polypyrrole. *Aust. J. Chem.* **16**, 1056–1075 (1963).
3. Bolto, B. & Weiss, D. Electronic Conduction in Polymers. II. The Electrochemical Reduction of Polypyrrole at Controlled Potential. *Aust. J. Chem.* **16**, 1076–1089 (1963).
4. Shirakawa, H., Louis, E. J., MacDiarmid, A. G., Chiang, C. K. & Heeger, A. J. Synthesis of electrically conducting organic polymers: halogen derivatives of polyacetylene, (CH)x. *J. Chem. Soc., Chem. Commun*. 578–580 (1977).doi:10.1039/C39770000578
5. Cambridge Display Technology. at <http://www.cdtltd.co.uk/>
6. OSRAM - OLEDs. at <http://www.osram.de/osram_de/trends-und-wissen/oled--home/index.jsp>
7. Heliatek erzielt mit 10,7% Effizienz neuen Weltrekord für seine organische Tandemzelle. *Heliatek* at <http://www.heliatek.com/newscenter/latest_news/heliatek-erzielt-mit-107-effizienz-neuen-weltrekord-fur-seine-organische-tandemzelle/>
8. Green, M. A., Emery, K., Hishikawa, Y., Warta, W. & Dunlop, E. D. Solar cell efficiency tables (version 39). *Progress in Photovoltaics: Research and Applications* **20**, 12–20 (2012).
9. Saga, T. Advances in crystalline silicon solar cell technology for industrial mass production. *NPG Asia Materials* **2**, 96–102 (2010).
10. Zhang, Y., De Boer, B. & Blom, P. W. M. Controllable Molecular Doping and Charge Transport in Solution-Processed Polymer Semiconducting Layers. *Advanced Functional Materials* **19**, 1901–1905 (2009).
11. Yim, K.-H. *et al.* Controlling Electrical Properties of Conjugated Polymers via a Solution-Based p-Type Doping. *Advanced Materials* **20**, 3319–3324 (2008).
12. Ha, S. D. & Kahn, A. Isolated molecular dopants in pentacene observed by scanning tunneling microscopy. *Physical Review B* **80**, 195410 (2009).
13. Gao, W. & Kahn, A. Controlled p-doping of zinc phthalocyanine by coevaporation with tetrafluorotetracyanoquinodimethane: A direct and inverse photoemission study. *Applied Physics Letters* **79**, 4040–4042 (2001).
14. Bolto, B., McNeill, R. & Weiss, D. Electronic Conduction in Polymers. III. Electronic Properties of Polypyrrole. *Aust. J. Chem.* **16**, 1090–1103 (1963).
15. Ito, T., Shirakawa, H. & Ikeda, S. Simultaneous polymerization and formation of polyacetylene film on the surface of concentrated soluble Ziegler-type catalyst solution. *Journal of Polymer Science: Polymer Chemistry Edition* **12**, 11–20 (1974).
16. Chiang, C. K. *et al.* Electrical Conductivity in Doped Polyacetylene. *Phys. Rev. Lett.* **40**, 1472–1472 (1978).
17. Grenthe, I. *Nobel Lectures in Chemistry: 1996-2000*. (World Scientific Publishing Co Pte Ltd, 2003).
18. Burroughes, J. H. *et al.* Light-emitting diodes based on conjugated polymers. *, Published online: 11 October 1990; | doi:10.1038/347539a0* **347**, 539–541 (1990).
19. Friend, R. H. *et al.* Electroluminescence in conjugated polymers. *Nature* **397**, 121–128 (1999).

20. Kraft, A., Grimsdale, A. C. & Holmes, A. B. Electroluminescent Conjugated Polymers—Seeing Polymers in a New Light. *Angewandte Chemie International Edition* **37**, 402–428 (1998).

21. Halls, J. J. M. *et al.* Efficient photodiodes from interpenetrating polymer networks. , *Published online: 10 August 1995; | doi:10.1038/376498a0* **376**, 498–500 (1995).

22. Yu, G., Gao, J., Hummelen, J. C., Wudl, F. & Heeger, A. J. POLYMER PHOTOVOLTAIC CELLS - ENHANCED EFFICIENCIES VIA A NETWORK OF INTERNAL DONOR-ACCEPTOR HETEROJUNCTIONS. *Science* **270**, 1789–1791 (1995).

23. Brabec, C. J., Sariciftci, N. S. & Hummelen, J. C. Plastic Solar Cells. *Advanced Functional Materials* **11**, 15–26 (2001).

24. Coakley, K. M. & McGehee, M. D. Conjugated Polymer Photovoltaic Cells. *Chem. Mater.* **16**, 4533–4542 (2004).

25. Dennler, G., Scharber, M. C. & Brabec, C. J. Polymer-Fullerene Bulk-Heterojunction Solar Cells. *Advanced Materials* **21**, 1323–1338 (2009).

26. Sirringhaus, H. *et al.* Two-dimensional charge transport in self-organized, high-mobility conjugated polymers. *Nature* **401**, 685–688 (1999).

27. Sirringhaus, H. Integrated Optoelectronic Devices Based on Conjugated Polymers. *Science* **280**, 1741–1744 (1998).

28. Sirringhaus, H. Device physics of solution-processed organic field-effect transistors. *Advanced Materials* **17**, 2411–2425 (2005).

29. Singh, T. B. & Sariciftci, N. S. Progress in Plastic Electronics Devices. *Annual Review of Materials Research* **36**, 199–230 (2006).

30. Kranzelbinder, G. & Leising, G. Organic solid-state lasers. *Reports on Progress in Physics* **63**, 729–762 (2000).

31. Kallinger, C. *et al.* A Flexible Conjugated Polymer Laser. *Advanced Materials* **10**, 920–923 (1998).

32. Pope, M., Swenberg, C. E. & Pope, M. *Electronic processes in organic crystals and polymers*. (Oxford University Press, 1999).

33. Haken, H. & Wolf, H. C. *Molekülphysik und Quantenchemie: Einführung in die experimentellen und theoretischen Grundlagen*. (Springer, 2006).

34. Schwoerer, M. & Wolf, H. C. *Organic molecular solids*. (Wiley-VCH, 2007).

35. May, V. & Kühn, O. *Charge and Energy Transfer Dynamics in Molecular Systems*. (John Wiley & Sons, 2004).

36. Bruice, P. Y. *Organic Chemistry, Fourth Edition*. (Prentice Hall, 2003).

37. Peierls, R. E. *Quantum Theory of Solids*. (Oxford University Press, USA, 2001).

38. *Nobel Lectures : Chemistry 1963-1970: 1963-1970 Vol 4*. (World Scientific Publishing, 1999).

39. Hückel, E. Quantentheoretische Beiträge zum Benzolproblem. *Zeitschrift für Physik A Hadrons and Nuclei* **70**, 204–286 (1931).

40. Hückel, E. Quantentheoretische Beiträge zum Problem der aromatischen und ungesättigten Verbindungen. III. *Zeitschrift für Physik A Hadrons and Nuclei* **76**, 628–648 (1932).

41. Hückel, E. Die freien Radikale der organischen Chemie. *Zeitschrift für Physik A Hadrons and Nuclei* **83**, 632–668 (1933).

42. Su, W. P., Schrieffer, J. R. & Heeger, A. J. Solitons in Polyacetylene. *Phys. Rev. Lett.* **42**, 1698–1701 (1979).

43. Dykstra, T. E., Kovalevskij, V., Yang, X. & Scholes, G. D. Excited state dynamics of a conformationally disordered conjugated polymer: A comparison of solutions and film. *Chemical Physics* **318**, 21–32 (2005).

44. Yang, X., Dykstra, T. E. & Scholes, G. D. Photon-echo studies of collective absorption and dynamic localization of excitation in conjugated polymers and oligomers. *Phys. Rev. B* **71**, 045203 (2005).

45. Scholes, G. D., Larsen, D. S., Fleming, G. R., Rumbles, G. & Burn, P. L. Origin of line broadening in the electronic absorption spectra of conjugated polymers: Three-pulse-echo studies of MEH-PPV in toluene. *Phys. Rev. B* **61**, 13670–13678 (2000).

46. Alvarado, S. F., Seidler, P. F., Lidzey, D. G. & Bradley, D. D. C. Direct Determination of the Exciton Binding Energy of Conjugated Polymers Using a Scanning Tunneling Microscope. *Phys. Rev. Lett.* **81**, 1082–1085 (1998).

47. Barth, S. & Bassler, H. Intrinsic photoconduction in PPV-type conjugated polymers. *Physical Review Letters* **79**, 4445–4448 (1997).

48. Bässler, H. *et al.* Excitons in π-conjugated polymers. *Synthetic Metals* **135–136**, 377–382 (2003).

49. Sariciftci, N. S. *Primary Photoexcitations In Conjugated Polymers: Molecular Exciton Versus Semiconductor Band Model*. (Wspc, 1997).

50. Scholes, G. D. & Rumbles, G. Excitons in nanoscale systems. *Nature Materials* **5**, 683–696 (2006).

51. Köhler, A. & Bässler, H. Triplet states in organic semiconductors. *Materials Science and Engineering: R: Reports* **66**, 71–109 (2009).

52. Rohner, P. G. Calculation of the Exchange Energy for Excitons in the Two-Body Model. *Phys. Rev. B* **3**, 433–439 (1971).

53. Di Nuzzo, D. *et al.* Improved Film Morphology Reduces Charge Carrier Recombination into the Triplet Excited State in a Small Bandgap Polymer-Fullerene Photovoltaic Cell. *Advanced Materials* **22**, 4321–4324 (2010).

54. Brédas, J.-L., Beljonne, D., Coropceanu, V. & Cornil, J. Charge-Transfer and Energy-Transfer Processes in π-Conjugated Oligomers and Polymers: A Molecular Picture. *Chemical Reviews* **104**, 4971–5004 (2004).

55. Holstein, T. Studies of Polaron Motion: Part I. The Molecular-Crystal Model. *Annals of Physics* **281**, 706–724 (2000).

56. Landau, L. Über die Bewegung der Elektronen in Kristallgitter. *Physik Z. Sowjetunion* **3**, 644–645 (1933).

57. Lane, Wei & Vardeny Studies of Charged Excitations in pi -Conjugated Oligomers and Polymers by Optical Modulation. *Phys. Rev. Lett.* **77**, 1544–1547 (1996).

58. Lane, P. A., Wei, X. & Vardeny, Z. V. Spin and spectral signatures of polaron pairs in pi-conjugated polymers. *Physical Review B* **56**, 4626–4637 (1997).

59. Janssen, R. A. J., Sariciftci, N. S. & Heeger, A. J. Photoinduced absorption of conjugated polymer/C60 solutions: Evidence of triplet-state photoexcitations and triplet-energy transfer in poly(3-alkylthiophene). *The Journal of Chemical Physics* **100**, 8641 (1994).

60. Wohlgenannt, M., Jiang, X. M., Vardeny, Z. V. & Janssen, R. A. J. Conjugation-Length Dependence of Spin-Dependent Exciton Formation Rates in Π-Conjugated Oligomers and Polymers. *Phys. Rev. Lett.* **88**, 197401 (2002).

61. Franck, J. & Dymond, E. G. Elementary processes of photochemical reactions. *Trans. Faraday Soc.* **21**, 536–542 (1926).

62. Condon, E. A Theory of Intensity Distribution in Band Systems. *Phys. Rev.* **28**, 1182–1201 (1926).

63. Kersting, R. *et al.* Femtosecond energy relaxation in π-conjugated polymers. *Phys. Rev. Lett.* **70**, 3820–3823 (1993).

64. Frolov, S. V., Bao, Z., Wohlgenannt, M. & Vardeny, Z. V. Ultrafast Spectroscopy of Even-Parity States in π-Conjugated Polymers. *Phys. Rev. Lett.* **85**, 2196–2199 (2000).

65. Lakowicz, J. R. *Principles of Fluorescence Spectroscopy*. (Springer, 2010).

66. Turro, N. J. *Modern molecular photochemistry*. (Benjamin/Cummings Pub. Co., 1978).

67. Kasha, M. Characterization of electronic transitions in complex molecules. *Discuss. Faraday Soc.* **9**, 14–19 (1950).

68. Kasha, M. Energy Transfer Mechanisms and the Molecular Exciton Model for Molecular Aggregates. *Radiation Research* **20**, 55–70 (1963).

69. Köhler, A. & Beljonne, D. The Singlet–Triplet Exchange Energy in Conjugated Polymers. *Advanced Functional Materials* **14**, 11–18 (2004).

70. Müller, J. G. *et al.* Linewidth-Limited Energy Transfer in Single Conjugated Polymer Molecules. *Phys. Rev. Lett.* **91**, 267403 (2003).

71. Shaw, P. E., Ruseckas, A. & Samuel, I. D. W. Exciton Diffusion Measurements in Poly(3-hexylthiophene). *Advanced Materials* **20**, 3516–3520 (2008).

72. Förster, T. Zwischenmolekulare Energiewanderung und Fluoreszenz. *Annalen der Physik* **437**, 55–75 (1948).

73. Förster, T. Experimentelle und theoretische Untersuchung des zwischemmolekularen Übergangs von Elektronenanregungsenergie. *Zeitschrift Naturforschung Teil A* **4**, 321 (1949).

74. Dexter, D. L. A Theory of Sensitized Luminescence in Solids. *The Journal of Chemical Physics* **21**, 836–850 (1953).

75. Deibel, C., Strobel, T. & Dyakonov, V. Role of the Charge Transfer State in Organic Donor-Acceptor Solar Cells. *Advanced Materials* **22**, 4097–4111 (2010).

76. Marcus, R. A. Electron transfer reactions in chemistry. Theory and experiment. *Rev. Mod. Phys.* **65**, 599–610 (1993).

77. Marcus, R. A. On the Theory of Oxidation-Reduction Reactions Involving Electron Transfer. I. *The Journal of Chemical Physics* **24**, 966–978 (1956).

78. Hwang, I.-W. *et al.* Ultrafast Electron Transfer and Decay Dynamics in a Small Band Gap Bulk Heterojunction Material. *Advanced Materials* **19**, 2307–2312 (2007).

79. Muller, J. G. *et al.* Ultrafast dynamics of charge carrier photogeneration and geminate recombination in conjugated polymer : fullerene solar cells. *Physical Review B* **72**, (2005).

80. Piris, J. *et al.* Photogeneration and Ultrafast Dynamics of Excitons and Charges in P3HT/PCBM Blends. *The Journal of Physical Chemistry C* **113**, 14500–14506 (2009).

81. Miller, A. & Abrahams, E. Impurity Conduction at Low Concentrations. *Physical Review* **120**, 745 (1960).

82. Onsager, L. Deviations from Ohm's Law in Weak Electrolytes. *Journal of Chemical Physics* **2**, 599–615 (1934).

83. Onsager, L. Initial recombination of ions. *Physical Review* **54**, 554–557 (1938).

84. Braun, C. L. Electric field assisted dissociation of charge transfer states as a mechanism of photocarrier production. *The Journal of Chemical Physics* **80**, 4157 (1984).

85. Goliber, T. E. & Perlstein, J. H. Analysis of photogeneration in a doped polymer system in terms of a kinetic model for electric-field-assisted dissociation of charge-transfer states. *The Journal of Chemical Physics* **80**, 4162–4167 (1984).

86. Bässler, H. Charge Transport in Disordered Organic Photoconductors a Monte Carlo Simulation Study. *physica status solidi (b)* **175**, 15–56 (1993).

87. Albrecht, U. & Bässler, H. Langevin-Type Charge Carrier Recombination in a Disordered Hopping System. *physica status solidi (b)* **191**, 455–459 (1995).

88. Albrecht, U. & Bässler, H. Efficiency of charge recombination in organic light emitting diodes. *Chemical Physics* **199**, 207–214 (1995).

89. Barth, S., Bässler, H., Scherf, U. & Müllen, K. Photoconduction in thin films of a ladder-type poly-para-phenylene. *Chemical Physics Letters* **288**, 147–154 (1998).

90. Clarke, T. M. & Durrant, J. R. Charge Photogeneration in Organic Solar Cells. *Chemical Reviews* **110**, 6736–6767 (2010).

91. Beljonne, D. *et al.* Electronic Processes at Organic−Organic Interfaces: Insight from Modeling and Implications for Opto-electronic Devices†. *Chem. Mater.* **23**, 591–609 (2011).

92. Goris, L. *et al.* Observation of the subgap optical absorption in polymer-fullerene blend solar cells. *Applied Physics Letters* **88**, 052113–052113–3 (2006).

93. Goris, L. *et al.* Absorption phenomena in organic thin films for solar cell applications investigated by photothermal deflection spectroscopy. *Journal of Materials Science* **40**, 1413–1418 (2005).

94. Drori, T. *et al.* Below-gap excitation of pi-conjugated polymer-Fullerene blends: implications for bulk organic heterojunction solar cells. *Phys Rev Lett* **101**, 037401 (2008).

95. Drori, T., Holt, J. & Vardeny, Z. V. Optical studies of the charge transfer complex in polythiophene/fullerene blends for organic photovoltaic applications. *Physical Review B* **82**, 8 (2010).

96. Morteani, A. C., Sreearunothai, P., Herz, L. M., Friend, R. H. & Silva, C. Exciton regeneration at polymeric semiconductor heterojunctions. *Physical Review Letters* **92**, (2004).

97. Morteani, A. C., Friend, R. H. & Silva, C. Exciton trapping at heterojunctions in polymer blends. *The Journal of Chemical Physics* **122**, 244906–244906–7 (2005).

98. Hallermann, M., Haneder, S. & Da Como, E. Charge-transfer states in conjugated polymer/fullerene blends: Below-gap weakly bound excitons for polymer photovoltaics. *Applied Physics Letters* **93**, 053307 (2008).

99. Veldman, D., Meskers, S. C. J. & Janssen, R. A. J. The Energy of Charge-Transfer States in Electron Donor-Acceptor Blends: Insight into the Energy Losses in Organic Solar Cells. *Advanced Functional Materials* **19**, 1939–1948 (2009).

100. Vandewal, K., Tvingstedt, K., Gadisa, A., Inganäs, O. & Manca, J. V. On the origin of the open-circuit voltage of polymer–fullerene solar cells. *Nature Materials* **8**, 904–909 (2009).

101. Hallermann, M. *et al.* Correlation between charge transfer exciton recombination and photocurrent in polymer/fullerene solar cells. *Applied Physics Letters* **97**, 023301 (2010).

102. Vandewal, K., Tvingstedt, K., Gadisa, A., Inganas, O. & Manca, J. V. Relating the open-circuit voltage to interface molecular properties of donor:acceptor bulk heterojunction solar cells. *Physical Review B* **81**, (2010).

103. Hallermann, M. *et al.* Charge Transfer Excitons in Polymer/Fullerene Blends: The Role of Morphology and Polymer Chain Conformation. *Advanced Functional Materials* **19**, 3662–3668 (2009).

104. Bixon, M., Jortner, J. & Verhoeven, J. W. Lifetimes for Radiative Charge Recombination in Donor-Acceptor Molecules. *J. Am. Chem. Soc.* **116**, 7349–7355 (1994).

105. Gould, I. R. *et al.* Radiative and nonradiative electron transfer in contact radical-ion pairs. *Chemical Physics* **176**, 439–456 (1993).

106. Jarzab, D. *et al.* Low-Temperature Behaviour of Charge Transfer Excitons in Narrow-Bandgap Polymer-Based Bulk Heterojunctions. *Advanced Energy Materials* **1**, 604–609 (2011).

107. Loi, M. A. *et al.* Charge Transfer Excitons in Bulk Heterojunctions of a Polyfluorene Copolymer and a Fullerene Derivative. *Advanced Functional Materials* **17**, 2111–2116 (2007).

108. Huang, Y. *et al.* Electronic structures of interfacial states formed at polymeric semiconductor heterojunctions. *Nature Materials* **7**, 483–489 (2008).

109. Gould, I. R., Young, R. H., Mueller, L. J., Albrecht, A. C. & Farid, S. Electronic Structures of Exciplexes and Excited Charge-Transfer Complexes. *J. Am. Chem. Soc.* **116**, 8188–8199 (1994).

110. Gould, I. R., Young, R. H., Mueller, L. J., Albrecht, A. C. & Farid, S. Electronic Coupling Matrix Elements in Acceptor-Donor Excited States and the Effect of Charge-Transfer Character on Their Radiative Rate Constants. *J. Am. Chem. Soc.* **116**, 3147–3148 (1994).

111. Veldman, D. *et al.* Compositional and Electric Field Dependence of the Dissociation of Charge Transfer Excitons in Alternating Polyfluorene Copolymer/Fullerene Blends. *Journal of the American Chemical Society* **130**, 7721–7735 (2008).

112. Hartenstein, B. & Bässler, H. Transport energy for hopping in a Gaussian density of states distribution. *Journal of Non-Crystalline Solids* **190**, 112–116 (1995).

113. Hertel, D. & Bässler, H. Photoconduction in Amorphous Organic Solids. *ChemPhysChem* **9**, 666–688 (2008).

114. Arkhipov, V. I., Emelianova, E. V. & Adriaenssens, G. J. Effective transport energy versus the energy of most probable jumps in disordered hopping systems. *Physical Review B* **64**, 125125 (2001).

115. Fishchuk, I. I., Arkhipov, V. I., Kadashchuk, A., Heremans, P. & Bassler, H. Analytic model of hopping mobility at large charge carrier concentrations in disordered organic semiconductors: Polarons versus bare charge carriers. *Physical Review B* **76**, (2007).

116. Hertel, D., Bässler, H., Scherf, U. & Hörhold, H. H. Charge carrier transport in conjugated polymers. *The Journal of Chemical Physics* **110**, 9214–9222 (1999).

117. Hertel, D., Scherf, U. & Bässler, H. Charge Carrier Mobility in a Ladder-Type Conjugated Polymer. *Advanced Materials* **10**, 1119–1122 (1998).

118. Shockley, W. & Queisser, H. J. Detailed Balance Limit of Efficiency of p-n Junction Solar Cells. *Journal of Applied Physics* **32**, 510 (1961).

119. Park, S. H. *et al.* Bulk heterojunction solar cells with internal quantum efficiency approaching 100%. *Nature Photonics* **3**, 297–302 (2009).

120. Morana, M. *et al.* Nanomorphology and Charge Generation in Bulk Heterojunctions Based on Low-Bandgap Dithiophene Polymers with Different Bridging Atoms. *Advanced Functional Materials* **20**, 1180–1188 (2010).

121. Mühlbacher, D. *et al.* High Photovoltaic Performance of a Low-Bandgap Polymer. *Advanced Materials* **18**, 2884–2889 (2006).

122. He, Z. *et al.* Enhanced power-conversion efficiency in polymer solar cells using an inverted device structure. *Nature Photonics* **6**, 591–595 (2012).

123. Brabec, C., Scherf, U. & Dyakonov, V. *Organic Photovoltaics: Materials, Device Physics, and Manufacturing Technologies*. (Wiley-VCH Verlag GmbH & Co. KGaA, 2008).

124. Brabec, C. J. & Durrant, J. R. Solution-Processed Organic Solar Cells. *MRS Bulletin* **33**, 670–675 (2008).

125. Jenekhe, S. A. A class of narrow-band-gap semiconducting polymers. , *Published online: 24 July 1986; | doi:10.1038/322345a0* **322**, 345–347 (1986).

126. Zhang, Q. T. & Tour, J. M. Low Optical Bandgap Polythiophenes by an Alternating Donor/Acceptor Repeat Unit Strategy. *J. Am. Chem. Soc.* **119**, 5065–5066 (1997).

127. Kim, J. Y. *et al.* Efficient Tandem Polymer Solar Cells Fabricated by All-Solution Processing. *Science* **317**, 222–225 (2007).

128. Scharber, M. C. *et al.* Design Rules for Donors in Bulk-Heterojunction Solar Cells—Towards 10 % Energy-Conversion Efficiency. *Advanced Materials* **18**, 789–794 (2006).

129. Peet, J. *et al.* Efficiency enhancement in low-bandgap polymer solar cells by processing with alkane dithiols. *Nature Materials* **6**, 497–500 (2007).

130. Lee, J. K. *et al.* Processing Additives for Improved Efficiency from Bulk Heterojunction Solar Cells. *Journal of the American Chemical Society* **130**, 3619–3623 (2008).

131. Etzold, F. *et al.* The Effect of Solvent Additives on Morphology and Excited-State Dynamics in PCPDTBT:PCBM Photovoltaic Blends. *J. Am. Chem. Soc.* **134**, 10569–10583 (2012).

132. Roncali, J. Conjugated poly (thiophenes): synthesis, functionalization, and applications. *Chemical Reviews* **92**, 711–738 (1992).

133. McCullough, R. D. The chemistry of conducting polythiophenes. *Advanced Materials* **10**, 93–+ (1998).

134. Mccullough, R. D. & Lowe, R. D. Enhanced Electrical-Conductivity in Regioselectively Synthesized Poly(3-Alkylthiophenes). *Journal of the Chemical Society-Chemical Communications* 70–72 (1992).doi:Article

135. Kline, R. J. & McGehee, M. D. Morphology and Charge Transport in Conjugated Polymers. *Polymer Reviews* **46**, 27–45 (2006).

136. Miyakoshi, R., Yokoyama, A. & Yokozawa, T. Synthesis of Poly(3-hexylthiophene) with a Narrower Polydispersity. *Macromolecular Rapid Communications* **25**, 1663–1666 (2004).

137. Clark, J., Silva, C., Friend, R. H. & Spano, F. C. Role of intermolecular coupling in the photophysics of disordered organic semiconductors: aggregate emission in regioregular polythiophene. *Phys Rev Lett* **98**, 206406 (2007).

138. Kim, Y. *et al.* A strong regioregularity effect in self-organizing conjugated polymer films and high-efficiency polythiophene:fullerene solar cells. *Nature Materials* **5**, 197–203 (2006).

139. Hwang, I.-W., Moses, D. & Heeger, A. J. Photoinduced Carrier Generation in P3HT/PCBM Bulk Heterojunction Materials. *Journal of Physical Chemistry C* **112**, 4350–4354 (2008).

140. Dresselhaus, M. S. & Dresslhaus, G. Fullerenes and Fullerene Derived Solids as Electronic Materials. *Annual Review of Materials Science* **25**, 487–523 (1995).

141. Kadish, K. M. & Ruoff, R. S. *Fullerenes: Chemistry, Physics, and Technology*. (John Wiley & Sons, 2000).

142. Taylor, R. & Walton, D. R. M. The chemistry of fullerenes. *, Published online: 24 June 1993; | doi:10.1038/363685a0* **363**, 685–693 (1993).

143. Sariciftci, N. S. *et al.* Semiconducting polymer-buckminsterfullerene heterojunctions: Diodes, photodiodes, and photovoltaic cells. *Applied Physics Letters* **62**, 585 (1993).

144. Blom, P. W. M., Mihailetchi, V. D., Koster, L. J. A. & Markov, D. E. Device Physics of Polymer:Fullerene Bulk Heterojunction Solar Cells. *Advanced Materials* **19**, 1551–1566 (2007).

145. Hoppe, H. *et al.* Nanoscale morphology of conjugated polymer/fullerene-based bulk-heterojunction solar cells. *Advanced Functional Materials* **14**, 1005–1011 (2004).

146. Wöbkenberg, P. H. *et al.* High mobility n-channel organic field-effect transistors based on soluble C60 and C70 fullerene derivatives. *Synthetic Metals* **158**, 468–472 (2008).

147. Von Hauff, E., Dyakonov, V. & Parisi, J. Study of field effect mobility in PCBM films and P3HT:PCBM blends. *Solar Energy Materials and Solar Cells* **87**, 149–156 (2005).

148. Azimi, H. *et al.* Nano-morphology characterization of organic bulk heterojunctions based on mono and bis-adduct fullerenes. *Organic Electronics* **13**, 1315–1321 (2012).

149. Bull, T. A., Pingree, L. S. C., Jenekhe, S. A., Ginger, D. S. & Luscombe, C. K. The Role of Mesoscopic PCBM Crystallites in Solvent Vapor Annealed Copolymer Solar Cells. *ACS Nano* **3**, 627–636 (2009).

150. Gu, Y., Wang, C. & Russell, T. P. Multi-Length-Scale Morphologies in PCPDTBT/PCBM Bulk-Heterojunction Solar Cells. *Advanced Energy Materials* **2**, 683–690 (2012).

151. Hebard, A. F., Haddon, R. C., Fleming, R. M. & Kortan, A. R. Deposition and characterization of fullerene films. *Applied Physics Letters* **59**, 2109 (1991).

152. Rispens, M. T. *et al.* Influence of the solvent on the crystal structure of PCBM and the efficiency of MDMO-PPV : PCBM 'plastic' solar cells. *Chemical Communications* 2116–2118 (2003).doi:Article

153. Cook, S. *et al.* A photophysical study of PCBM thin films. *Chemical Physics Letters* **445**, 276–280 (2007).

154. Bazhenov, A. V., Gorbunov, A. V., Maksimuk, M. Y. & Fursova, T. N. Photoinduced light absorption by C-60 films in the 0.08-4.0-eV spectral range. *Journal of Experimental and Theoretical Physics* **85**, 135–140 (1997).

155. Pichler, K. *et al.* Photophysical properties of solid films of fullerene, C60. *Journal of Physics: Condensed Matter* **3**, 9259 (1991).

156. Reber, C. *et al.* Luminescence and Absorption-Spectra of C60 Films. *Journal of Physical Chemistry* **95**, 2127–2129 (1991).

157. Schlaich, H. *et al.* Absorption at the dipole-forbidden optical gap of crystalline C60. *Chemical Physics Letters* **236**, 135–140 (1995).

158. Feldmann, J. *et al.* White Luminescence from Solid C 60. *Europhysics Letters (EPL)* **20**, 553–558 (1992).

159. Guo, J., Ohkita, H., Benten, H. & Ito, S. Charge generation and recombination dynamics in poly(3-hexylthiophene)/fullerene blend films with different regioregularities and morphologies. *J Am Chem Soc* **132**, 6154–64 (2010).

160. Anderson, T. L., Komplin, G. C. & Pietro, W. J. Rectifying junctions in peripherally-substituted metallophthalocyanine bilayer films. *J. Phys. Chem.* **97**, 6577–6578 (1993).

161. Chen, W., Chen, S., Qi, D. C., Gao, X. Y. & Wee, A. T. S. Surface Transfer p-Type Doping of Epitaxial Graphene. *J. Am. Chem. Soc.* **129**, 10418–10422 (2007).

162. Coletti, C. *et al.* Charge neutrality and band-gap tuning of epitaxial graphene on SiC by molecular doping. *Phys. Rev. B* **81**, 235401 (2010).

163. Zhang, Y. & Blom, P. W. M. Field-assisted ionization of molecular doping in conjugated polymers. *Organic Electronics* **11**, 1261–1267 (2010).

164. Gao, Z. Q. *et al.* An organic p-type dopant with high thermal stability for an organic semiconductor. *Chem. Commun.* 117–119 (2007).doi:10.1039/B713566A

165. Kistenmacher, T. J., Phillips, T. E. & Cowan, D. O. The crystal structure of the 1:1 radical cation–radical anion salt of 2,2'-bis-l,3-dithiole (TTF) and 7,7,8,8-tetracyanoquinodimethane (TCNQ). *Acta Crystallographica Section B* **30**, 763–768 (1974).

166. Bryce, M. R. Recent progress on conducting organic charge-transfer salts. *Chem. Soc. Rev.* **20**, 355–390 (1991).

167. Cohen, M. J., Coleman, L. B., Garito, A. F. & Heeger, A. J. Electrical conductivity of tetrathiofulvalinium tetracyanoquinodimethan (TTF) (TCNQ). *Phys. Rev. B* **10**, 1298–1307 (1974).

168. Egerton, R. F. *Physical Principles of Electron Microscopy*.

169. Ono, S. & Kanaya, K. ENERGY-DEPENDENCE OF SECONDARY-EMISSION BASED ON THE RANGE-ENERGY RETARDATION POWER FORMULA. *Journal of Physics D-Applied Physics* **12**, 619–632 (1979).

170. Falkenberg, C. *et al.* Efficient p-i-n type organic solar cells incorporating 1,4,5,8-naphthalenetetracarboxylic dianhydride as transparent electron transport material. *Journal of Applied Physics* **104**, 034506–034506–6 (2008).

171. Reineke, S. *et al.* White organic light-emitting diodes with fluorescent tube efficiency. *Nature* **459**, 234–238 (2009).

172. Tunc, A. V. *et al.* Molecular doping of low-bandgap-polymer:fullerene solar cells: Effects on transport and solar cells. *Organic Electronics* **13**, 290–296 (2012).

173. Loiudice, A., Rizzo, A., Biasiucci, M. & Gigli, G. Bulk Heterojunction versus Diffused Bilayer: The Role of Device Geometry in Solution p-Doped Polymer-Based Solar Cells. *J. Phys. Chem. Lett.* **3**, 1908–1915 (2012).

174. Chan, C. K., Zhao, W., Kahn, A. & Hill, I. G. Influence of chemical doping on the performance of organic photovoltaic cells. *Applied Physics Letters* **94**, 203306 (2009).

175. Li, H., Winget, P. & Bredas, J.-L. Surface Modification of Indium-Tin-Oxide Via Self-Assembly of a Donor-Acceptor Complex: A Density Functional Theory Study. *Advanced Materials* **24**, 687–693 (2012).

176. Hanson, E. L., Guo, J., Koch, N., Schwartz, J. & Bernasek, S. L. Advanced Surface Modification of Indium Tin Oxide for Improved Charge Injection in Organic Devices. *J. Am. Chem. Soc.* **127**, 10058–10062 (2005).

177. Zhang, Y. & Blom, P. W. M. Enhancement of the hole injection into regioregular poly(3-hexylthiophene) by molecular doping. *Applied Physics Letters* **97**, 083303 (2010).

178. Harada, K., Riede, M., Leo, K., Hild, O. & Elliott, C. Pentacene homojunctions: Electron and hole transport properties and related photovoltaic responses. *Physical Review B* **77**, (2008).

179. Deschler, F. *et al.* Reduced Charge Transfer Exciton Recombination in Organic Semiconductor Heterojunctions by Molecular Doping. *Phys. Rev. Lett.* **107**, 127402 (2011).

180. Gwinner, M. C. *et al.* Doping of Organic Semiconductors Using Molybdenum Trioxide: a Quantitative Time-Dependent Electrical and Spectroscopic Study. *Advanced Functional Materials* **21**, 1432–1441 (2011).

181. Pingel, P. *et al.* Charge-Transfer Localization in Molecularly Doped Thiophene-Based Donor Polymers. *The Journal of Physical Chemistry Letters* **1**, 2037–2041 (2010).

182. Aziz, E. F. *et al.* Localized Charge Transfer in a Molecularly Doped Conducting Polymer. *Advanced Materials* **19**, 3257–3260 (2007).

183. Kleemann, H. *et al.* Structural phase transition in pentacene caused by molecular doping and its effect on charge carrier mobility. *Organic Electronics* **13**, 58–65 (2012).

184. Salleo, A., Kline, R. J., DeLongchamp, D. M. & Chabinyc, M. L. Microstructural Characterization and Charge Transport in Thin Films of Conjugated Polymers. *Advanced Materials* **22**, 3812–3838 (2010).

185. Zhu, L., Kim, E.-G., Yi, Y. & Brédas, J.-L. Charge Transfer in Molecular Complexes with 2,3,5,6-Tetrafluoro-7,7,8,8-tetracyanoquinodimethane (F4-TCNQ): A Density Functional Theory Study. *Chem. Mater.* **23**, 5149–5159 (2011).

186. Yang, H., Joo Shin, T., Bao, Z. & Ryu, C. Y. Structural transitions of nanocrystalline domains in regioregular poly(3-hexyl thiophene) thin films. *Journal of Polymer Science Part B: Polymer Physics* **45**, 1303–1312 (2007).

187. Morana, M. *et al.* Bipolar Charge Transport in PCPDTBT-PCBM Bulk-Heterojunctions for Photovoltaic Applications. *Advanced Functional Materials* **18**, 1757–1766 (2008).

188. Da Como, E., Loi, M. A., Murgia, M., Zamboni, R. & Muccini, M. J-Aggregation in α-Sexithiophene Submonolayer Films on Silicon Dioxide. *J. Am. Chem. Soc.* **128**, 4277–4281 (2006).

189. Loi, M. A. *et al.* Supramolecular organization in ultra-thin films of α-sexithiophene on silicon dioxide. *Nature Materials* **4**, 81–85 (2005).

190. Tsen, A. W., Cicoira, F., Malliaras, G. G. & Park, J. Photoelectrical imaging and characterization of point contacts in pentacene thin-film transistors. *Applied Physics Letters* **97**, 023308–023308–3 (2010).

191. Bolinger, J. C., Traub, M. C., Adachi, T. & Barbara, P. F. Ultralong-Range Polaron-Induced Quenching of Excitons in Isolated Conjugated Polymers. *Science* **331**, 565–567 (2011).

192. Zhang, Y., De Boer, B. & Blom, P. W. M. Trap-free electron transport in poly(p-phenylene vinylene) by deactivation of traps with n-type doping. *Phys. Rev. B* **81**, 085201 (2010).

193. Carsten, B. *et al.* Examining the Effect of the Dipole Moment on Charge Separation in Donor–Acceptor Polymers for Organic Photovoltaic Applications. *J. Am. Chem. Soc.* **133**, 20468–20475 (2011).

194. Tautz, R. *et al.* Structural correlations in the generation of polaron pairs in low-bandgap polymers for photovoltaics. *Nature Communications* **3**, 970 (2012).

195. Prosa, T. J., Winokur, M. J., Moulton, J., Smith, P. & Heeger, A. J. X-ray structural studies of poly(3-alkylthiophenes): an example of an inverse comb. *Macromolecules* **25**, 4364–4372 (1992).

196. Gao, W. & Kahn, A. Electronic structure and current injection in zinc phthalocyanine doped with tetrafluorotetracyanoquinodimethane: Interface versus bulk effects. *Organic Electronics* **3**, 53–63 (2002).

197. Piromreun, P. *et al.* Role of CsF on electron injection into a conjugated polymer. *Applied Physics Letters* **77**, 2403–2405 (2000).

198. Gross, M. *et al.* Improving the performance of doped π-conjugated polymers for use in organic light-emitting diodes. *Nature* **405**, 661–665 (2000).

199. Lee, K. *et al.* Metallic transport in polyaniline. *Nature* **441**, 65–68 (2006).

200. Patil, A. O., Heeger, A. J. & Wudl, F. Optical properties of conducting polymers. *Chem. Rev.* **88**, 183–200 (1988).

201. Malliaras, G. & Friend, R. An Organic Electronics Primer. *Physics Today* **58**, 53–58 (2005).

202. Gulbinas, V. *et al.* Dynamics of the Electric Field-Assisted Charge Carrier Photogeneration in Ladder-Type Poly(Para-Phenylene) at a Low Excitation Intensity. *Phys. Rev. Lett.* **89**, 107401 (2002).

203. Hendry, E., Schins, J. M., Candeias, L. P., Siebbeles, L. D. & Bonn, M. Efficiency of exciton and charge carrier photogeneration in a semiconducting polymer. *Phys Rev Lett* **92**, 196601 (2004).

204. Morita, S., Zakhidov, A. A. & Yoshino, K. Doping effect of buckminsterfullerene in conducting polymer: Change of absorption spectrum and quenching of luminescene. *Solid State Communications* **82**, 249–252 (1992).

205. Kersting, R. *et al.* Ultrafast Field-Induced Dissociation of Excitons in Conjugated Polymers. *Phys. Rev. Lett.* **73**, 1440–1443 (1994).

206. Muntwiler, M., Yang, Q., Tisdale, W. A. & Zhu, X. Y. Coulomb Barrier for Charge Separation at an Organic Semiconductor Interface. *Physical Review Letters* **101**, (2008).

207. Street, R. A., Schoendorf, M., Roy, A. & Lee, J. H. Interface state recombination in organic solar cells. *Physical Review B* **81**, 205307 (2010).

208. Sheng, C.-X., Tong, M., Singh, S. & Vardeny, Z. V. Experimental determination of the charge/neutral branching ratio η in the photoexcitation of π-conjugated polymers by broadband ultrafast spectroscopy. *Phys. Rev. B* **75**, 085206 (2007).

209. Cerullo, G. & De Silvestri, S. Ultrafast optical parametric amplifiers. *Review of Scientific Instruments* **74**, 1–18 (2003).

210. Herrmann, D. *et al.* Approaching the full octave: noncollinear optical parametric chirped pulse amplification with two-color pumping. *Optics Express* **18**, 18752 (2010).

211. Osterbacka, R. Two-Dimensional Electronic Excitations in Self-Assembled Conjugated Polymer Nanocrystals. *Science* **287**, 839–842 (2000).

212. Green, M. A., Emery, K., Hishikawa, Y. & Warta, W. Solar cell efficiency tables (version 37). *Progress in Photovoltaics: Research and Applications* **19**, 84–92 (2011).

213. Chen, H.-Y. *et al.* Polymer solar cells with enhanced open-circuit voltage and efficiency. *Nature Photonics* **3**, 649–653 (2009).

214. Luer, L. *et al.* Oxygen-induced quenching of photoexcited states in polythiophene films. *Organic Electronics* **5**, 83–89 (2004).

215. Rashmi, Kapoor, A. K., Kumar, U., Balakrishnan, V. R. & Basu, P. K. Degradation process in organic thin film devices fabricated using P3HT. *Pramana-Journal of Physics* **68**, 489–498 (2007).

216. Padinger, F. *et al.* Degradation of bulk heterojunction solar cells operated in an inert gas atmosphere: a systematic study. *Synthetic Metals* **121**, 1605–1606 (2001).

217. Manceau, M., Rivaton, A., Gardette, J. L., Guillerez, S. & Lemaitre, N. The mechanism of photo- and thermooxidation of poly(3-hexylthiophene) (P3HT) reconsidered. *Polymer Degradation and Stability* **94**, 898–907 (2009).

218. Abdou, M. S. A., Orfino, F. P., Xie, Z. W., Deen, M. J. & Holdcroft, S. Reversible Charge-Transfer Complexes between Molecular-Oxygen and Poly(3-Alkylthiophene)S. *Advanced Materials* **6**, 838–841 (1994).

219. Abdou, M. S. A., Orfino, F. P., Son, Y. & Holdcroft, S. Interaction of oxygen with conjugated polymers: Charge transfer complex formation with poly(3-alkylthiophenes). *Journal of the American Chemical Society* **119**, 4518–4524 (1997).

220. Kawano, K. *et al.* Degradation of organic solar cells due to air exposure. *Solar Energy Materials and Solar Cells* **90**, 3520–3530 (2006).

221. Jorgensen, M., Norrman, K. & Krebs, F. C. Stability/degradation of polymer solar cells. *Solar Energy Materials and Solar Cells* **92**, 686–714 (2008).

222. Tromholt, T., Katz, E. A., Hirsch, B., Vossier, A. & Krebs, F. C. Effects of concentrated sunlight on organic photovoltaics. *Applied Physics Letters* **96**, 073501 (2010).

223. Gaudiana, R. & Brabec, C. Organic materials: Fantastic plastic. *Nature Photonics* **2**, 287–289 (2008).

224. Kumar, A. *et al.* Origin of Radiation-Induced Degradation in Polymer Solar Cells. *Advanced Functional Materials* **20**, 2729–2736 (2010).

225. Lessmann, R. *et al.* Aging of flat heterojunction zinc phthalocyanine/fullerene C60 organic solar cells. *Organic Electronics* **11**, 539–543 (2010).

226. Lin, C., Lin, E.-Y. & Tsai, F.-Y. Enhanced Thermal Stability and Efficiency of Polymer Bulk-Heterojunction Solar Cells by Low-Temperature Drying of the Active Layer. *Advanced Functional Materials* **20**, 834–839 (2010).

227. Reese, M. O. *et al.* Pathways for the degradation of organic photovoltaic P3HT: PCBM based devices. *Solar Energy Materials and Solar Cells* **92**, 746–752 (2008).

228. Steim, R., Choulis, S. A., Schilinsky, P., Lemmer, U. & Brabec, C. J. Formation and impact of hot spots on the performance of organic photovoltaic cells. *Applied Physics Letters* **94**, 043304–043304–3 (2009).

229. Ecker, B. *et al.* Degradation Effects Related to the Hole Transport Layer in Organic Solar Cells. *Advanced Functional Materials* **21**, 2705–2711 (2011).

230. Seemann, A. *et al.* Reversible and irreversible degradation of organic solar cell performance by oxygen. *Solar Energy* **85**, 1238–1249 (2011).

231. Guss, W. *et al.* Fluorescence from X traps in C60 single crystals. *Phys Rev Lett* **72**, 2644–2647 (1994).

232. He, X. *et al.* Formation of Nanopatterned Polymer Blends in Photovoltaic Devices. *Nano Lett.* **10**, 1302–1307 (2010).

233. Schubert, M. *et al.* Heterojunction topology versus fill factor correlations in novel hybrid small-molecular/polymeric solar cells. *The Journal of Chemical Physics* **130**, 094703 (2009).

234. Schafferhans, J., Baumann, A., Deibel, C. & Dyakonov, V. Trap distribution and the impact of oxygen-induced traps on the charge transport in poly(3-hexylthiophene). *Applied Physics Letters* **93**, 093303–093303–3 (2008).

235. Abdou, M. S. A. & Holdcroft, S. Solid-state photochemistry of pi-conjugated poly(3-alkylthiophenes). *Canadian Journal of Chemistry-Revue Canadienne De Chimie* **73**, 1893–1901 (1995).

236. Reese, M. O. *et al.* Photoinduced Degradation of Polymer and Polymer–Fullerene Active Layers: Experiment and Theory. *Advanced Functional Materials* **20**, 3476–3483 (2010).

237. Caronna, T., Forte, M., Catellani, M. & Meille, S. V. Photodegradation and photostabilization studies of poly(3-butylthiophene) in the solid state. *Chemistry of Materials* **9**, 991–995 (1997).

238. Hintz, H., Egelhaaf, H. J., Peisert, H. & Chasse, T. Photo-oxidation and ozonization of poly(3-hexylthiophene) thin films as studied by UV/VIS and photoelectron spectroscopy. *Polymer Degradation and Stability* **95**, 818–825 (2010).

239. Hintz, H., Peisert, H., Egelhaaf, H.-J. & Chassé, T. Reversible and Irreversible Light-Induced p-Doping of P3HT by Oxygen Studied by Photoelectron Spectroscopy (XPS/UPS). *J. Phys. Chem. C* **115**, 13373–13376 (2011).

240. Deschler, F. *et al.* The Effect of Ageing on Exciton Dynamics, Charge Separation, and Recombination in P3HT/PCBM Photovoltaic Blends. *Advanced Functional Materials* **22**, 1461–1469 (2012).

241. Guo, J., Ohkita, H., Yokoya, S., Benten, H. & Ito, S. Bimodal Polarons and Hole Transport in Poly(3-hexylthiophene):Fullerene Blend Films. *J. Am. Chem. Soc.* **132**, 9631–9637 (2010).

242. Jiang, X. m. *et al.* Spectroscopic Studies of Photoexcitations in Regioregular and Regiorandom Polythiophene Films. *Advanced Functional Materials* **12**, 587–597 (2002).

243. Hukic-Markosian, G. & Vardeny, Z. V. Magneto-optical studies of 1-(3-methoxycarbonyl)-propyl-1-phenyl-(6,6)C61; PCBM. *Synthetic Metals* **160**, 314–316 (2010).

244. Hodgkiss, J. M. *et al.* Subnanosecond Geminate Charge Recombination in Polymer-Polymer Photovoltaic Devices. *Phys. Rev. Lett.* **104**, 177701 (2010).

245. Collini, E. & Scholes, G. D. Coherent intrachain energy migration in a conjugated polymer at room temperature. *Science* **323**, 369–73 (2009).

246. Beljonne, D., Shuai, Z., Pourtois, G. & Bredas, J. L. Spin−Orbit Coupling and Intersystem Crossing in Conjugated Polymers: A Configuration Interaction Description. *J. Phys. Chem. A* **105**, 3899–3907 (2001).

247. Scharber, M. C. *et al.* Charge transfer excitons in low band gap polymer based solar cells and the role of processing additives. *Energy & Environmental Science* **4**, 5077 (2011).

248. Sommer, M., Lindner, S. M. & Thelakkat, M. Microphase-Separated Donor–Acceptor Diblock Copolymers: Influence of HOMO Energy Levels and Morphology on Polymer Solar Cells. *Advanced Functional Materials* **17**, 1493–1500 (2007).

249. Dittmer, J. J. *et al.* Crystal network formation in organic solar cells. *Solar Energy Materials and Solar Cells* **61**, 53–61 (2000).

Acknowledgements

This dissertation was carried out at the Photonics and Optoelectronics Group of the Ludwig-Maximilians-Universität München under the supervision of Prof. Jochen Feldmann. I would like to thank everybody, who made this thesis possible and supported me in completing the presented work!

At first place I would like to thank Prof. Jochen Feldmann for giving me the opportunity to do my thesis in his group, the scientific discussions, the opportunity to take part at international conferences and his many useful ideas and comments. In the last three years, I had the opportunity to advance not only scientifically, but also in many other areas. I would like to emphasise the high research standard of the chair and the excellent experimental equipment. The variety of experimental facilities allows the investigation of a topic from many different perspectives and gives the opportunity to follow different ideas.

In particular, I would like to thank Dr. Enrico Da Como. He was of special importance with his support and encouragement during the whole thesis. His enthusiasm and ideas led to many interesting experiments. He was always open to try new things and discuss new directions. It was always fun to talk about recent results and discuss the interpretations. I remember our meetings on Friday afternoons - sorry for keeping you late at work and annoying your wife. Grazie mille e ogni bene possibile per il futuro in Inghilterra!

I am especially grateful to the Bundesministerium für Bildung und Forschung (BMBF) for funding in the project “OPV Stabilität” and the Bayerisches Staatsministerium für Wissenschaft, Forschung und Kunst for funding in the project „Solar Technologies go Hybrid”.

Many thanks to all the people from Konarka Technologies for the opportunity to work in such a great collaboration and for the supply of state-of-the-art materials and devices. Here, I want to mention in particular Dr. Hans-Joachim Egelhaaf, Peter Kutka and Tobias Sauermann. I would also like to thank our collaborators from the Universität Oldenburg, especially Prof. Elizabeth von Hauff and Dr. Antonietta de Sio. Furthermore, many thanks go to Prof. Manfred Bayer from the Universität Dortmund for the opportunity to perform measurements there.

During my thesis I also had the opportunity to work with several final year students. Many thanks go to Felix Anger, Daniel Riedel, Konrad Maier and Sebastian Kowollik, who showed great commitment during their work and helped to look at the topic from different angles. It was great fun working with you guys!

In addition, I am very grateful to all members of the group. The atmosphere and the teamwork at the chair were always great! In particular, I would like to thank all my office mates Markus Hallermann, Thomas Limmer, Jaekwon Do, Michael Fedoruk, Dr. Haojin Ba, Dr. Wei Li and Anastasia Babynina for the pleasant and enjoyable time in the office. Sorry for annoying you with all my talk about the latest sports results. I would also like to especially thank the people who were proof-reading this thesis: Ilka Kriegel, Dr. Nicolas Bouchonville, Dr. Haojin Ba and Dr. Mike Carlson.

Last but not least, I am indebted to Stefan Niedermaier, Anna Helfrich, Christian Holopirek, and Gerlinde Adam for help in many technical, chemical, electronic and administrational questions during my time in the group. You are the heart and soul of the chair. Thanks for your support!

Special thanks go to all the people from my private environment. To my girlfriend Katharina Vogel, who showed me that there is more in science than physics. To my sisters, Gloria and Florentina, who always made sure I do not lose touch with the “real” world from spending too much time in the labs. And finally to my parents, who supported me during my whole life and always encouraged me to follow my interests.